The role of the GABARAP Protein in the Intracellular Trafficking of FVIII

Dissertation
zur
Erlangung des Doktorgrades (Dr. rer. nat.)
der
Mathematisch-Naturwissenschaftlichen Fakultät
der
Rheinischen Friedrich-Wilhelms-Universität Bonn

vorgelegt von

Salime El Hazzouri

aus Tripoli, Libanon

Bonn, April 2025

Angefertigt mit Genehmigung der Mathematisch-Naturwissenschaftlichen Fakultät der Rheinischen Friedrich-Wilhelms-Universität Bonn.

Gutachter/Betreuer: PD Dr. rer. nat. Osman El Maarri

Gutachterin: Prof. Dr. rer. nat. Diana Imhof

Tag der Promotion: 20.10.2025

Erscheinungsjahr: 2025

Read, ˹O Prophet, ˺ in the Name of your Lord Who created—

created humans from a clinging clot.

Read! And your Lord is the Most Generous,

Who taught by the pen—

taught humanity what they knew not.

The Clot (96: 1-5), the Holy Quran

Summary

FVIII is a glycoprotein secreted by liver sinusoidal endothelial cells (LSECs) that plays an essential role in the intrinsic pathway of the coagulation cascade. Intracellularly, FVIII biosynthesis and processing are supported by known interactions with the Endoplasmic Reticulum chaperones, Calnexin (CANX), Calreticulin (CALR), and BiP, as well as ERGIC transport proteins, LMAN1 and MCFD2. However, compared to other heavily glycosylated proteins, like FV and vWF, FVIII transport through the ERGIC and its further trafficking appear limited. Despite its clinical importance, the overall intracellular lifecycle of FVIII remains poorly understood. Our team previously identified a novel FVIII secretion-modulating protein, ''GABARAP'' (Gamma-Aminobutyric Acid Type A Receptor-Associated Protein), using a yeast two-hybrid screen. Subsequent studies employing CRISPR/Cas9-knockouts and siRNA-based-knockdowns revealed the involvement of GABARAP in FVIII secretion. In this thesis, three key aspects were investigated: **1)** the interaction between GABARAP and FVIII, **2)** the intracellular localization of FVIII and GABARAP across subcellular compartments, and **3)** the effects of CRISPR/Cas9-KOs of both FVIII-associated control proteins (Calnexin, Calreticulin, LMAN1, and MCFD2) and ATG8-family proteins (GABARAP, GABARAPL1, and GABARAPL2) on FVIII secretion and intracellular trafficking, under basal (untreated) and experimentally manipulated conditions. Here, it is demonstrated that the interaction between GABARAP and FVIII is weak, transient or potentially regulated via an intermediary protein. Despite this, GABARAP^{KO} re-distributed FVIII intracellularly in a manner similar to patterns observed in CANX^{KO} and CALR^{KO} clones (ER-chaperone-KOs), contrasting with patterns seen in GABARAPL1^{KO} and GABARAPL2^{KO} (GABARAP homologs). Consistently, pairwise double-KO combinations, including CANX, CALR and GABARAP showed as well comparable impacts on FVIII compartmental localization. Additionally, GABARAP localized to compartments involved in FVIII processing and appeared to also contribute to the maintenance of organized Golgi morphology in HEK cells. Finally, cell treatment with Brefeldin A, glucose starvation, chloroquine, and Rab7 inhibition—agents known to affect ER-to-Golgi transport and specific pathways of the endomembrane system, altered FVIII secretion and intracellular trafficking. These perturbations further aligned the effects of GABARAP^{KO} with those of CANX^{KO} and CALR^{KO}. Collectively, these findings provide deeper insights into FVIII intracellular processing

in the endomembrane system and related vesicles in addition to the potential functional role of GABARAP in these mechanisms.

Zusammenfassung

FVIII ist ein Glykoprotein, das von lebersinusoiden Endothelzellen (LSECs) sezerniert wird und eine essenzielle Rolle im intrinsischen Teil der Gerinnungskaskade spielt. Intrazellulär wird die Biosynthese von FVIII durch bekannte Interaktionen mit Chaperonen des ERs– darunter Calnexin (CANX), Calreticulin (CALR) und BiP – sowie mit ERGIC-Transportproteinen wie LMAN1 und MCFD2 unterstützt. Im Vergleich zu anderen stark glykosylierten Proteinen wie FV und vWF erscheint der Transport von FVIII durch das ERGIC und seine weitere intrazelluläre Verteilung jedoch eingeschränkt. Trotz seiner klinischen Relevanz ist der gesamte intrazelluläre Lebenszyklus von FVIII bisher nur unzureichend verstanden. Unsere Arbeitsgruppe identifizierte zuvor ein neuartiges FVIII-sekretionsmodulierendes Protein, GABARAP (Gamma-Aminobuttersäure-Typ-A-Rezeptor-assoziiertes Protein), mittels eines Yeast-Two-Hybrid-Screens. Nachfolgende Studien unter Verwendung von CRISPR/Cas9-Knockouts und siRNA- Knockdowns zeigten die Beteiligung von GABARAP an der FVIII-Sekretion. In dieser Arbeit wurden drei zentrale Aspekte untersucht: **1)** die Interaktion zwischen GABARAP und FVIII, **2)** die intrazelluläre Lokalisation von FVIII und GABARAP in verschiedenen subzellulären Kompartimenten sowie **3)** die Auswirkungen von CRISPR/Cas9-Knockouts sowohl FVIII-assoziierter Kontrollproteine (Calnexin, Calreticulin, LMAN1 und MCFD2) als auch von ATG8-Familienproteinen (GABARAP, GABARAPL1 und GABARAPL2) auf die Sekretion und intrazelluläre Verteilung von FVIII unter basalen (unbehandelten) sowie experimentell manipulierten Bedingungen. Es wurde gezeigt, dass die Interaktion zwischen GABARAP und FVIII schwach, transient oder möglicherweise durch ein drittes Protein vermittelt ist. Dennoch führte der GABARAP-Knockout ($GABARAP^{KO}$) zu einer Umverteilung von FVIII innerhalb der Zelle, ähnlich den Mustern, die bei $CANX^{KO}$ und $CALR^{KO}$ (ER-Chaperon-KOs) beobachtet wurden – im Gegensatz zu den Unterschieden, die bei $GABARAPL1^{KO}$ und $GABARAPL2^{KO}$ (GABARAP-Homologe) festgestellt wurden. Konsistent zeigten paarweise Double-KO-Kombinationen, einschließlich CANX, CALR und GABARAP, ebenfalls vergleichbare Effekte auf die kompartimentelle Lokalisation von FVIII. Darüber hinaus lokalisierte GABARAP in Kompartimente, die an der FVIII-Prozessierung beteiligt sind, und trug offenbar auch zur Organisation der Golgi-Morphologie in HEK-Zellen bei. Schließlich beeinflussten Behandlungen mit Brefeldin A, Glukoseentzug, Chloroquin und Rab7-Inhibition – Substanzen, die für ihre Wirkung auf den ER-Golgi-Transport und bestimmte Signalwege des

endomembranösen Systems bekannt sind – die Sekretion und intrazelluläre Verteilung von FVIII. Diese Störungen führten erneut dazu, dass sich die Effekte des GABARAP^{KO} stärker denen von CANX^{KO} und CALR^{KO} annäherten. Zusammenfassend liefern diese Ergebnisse neue Einblicke in die intrazelluläre Verarbeitung von FVIII innerhalb des endomembranösen Systems und verwandter Vesikel sowie in die potenzielle funktionelle Rolle von GABARAP in diesen Mechanismen.

Table of Contents

List of Abbreviations

aa	Amino Acid
AAV	Adeno Associated Virus
AdMLP	adenovirus major late
ADP	Adenosine Diphosphate
ALFY	autophagy-linked FYVE protein
AMO1	Human Multiple Myeloma Cells
a-PPT	Activated Partial Thromboplastin Time
ARL8B	ADP-Ribosylation Factor-Like Protein 8B
ATG7	Autophagy-related gene 7
ATG8	Autophagy-related protein 8
ATP	Adenosine Triphosphate
BDD- FVIII	B-deleted-domain FVIII
BFA	Brefeldin A
BHK	Baby Hamster Kidney cells
BiP	Binding Immunoglobulin Protein
BLItz	Bio-layer Interferometry Assay
bp(s),kbp (s)	base pairs, kilo base pairs
bps	base pairs
BSA	Bovine Serum Albumin
CA	Cellulose Acetate Membrane
Ca^{2+}	Calcium ions
CaCl2	Calcium Chloride
CALR	Calreticulin
CANX	Calnexin
Cas9	CRISPR-associated protein 9
CCCP	protonophore carbonyl cyanide 3-chlorophenylhydrazone
CFTR	cystic fibrosis transmembrane conductance regulator
CHO	Chinese Hamster Ovary cells
CHO-K1	Chinese Hamster Ovary (clone K1) cells
Clover/ScarletI	crimson clover (Trifolium incarnatum)
cm, mm	centimeter, millimeter
CMV	Cytomegalovirus
CO_2	Carbon Dioxide
co-IP	Co-immunoprecipitation
COPB	Coatomer Protein Complex B
COPI	Coat Protein Complex I
COPII	Coat Protein Complex II
COS-1	CV-1 derived Monkey Kidney cells
CQ	Chloroquine
CRD	carbohydrate recognition domain
CRISPR	Clustered Regularly Interspaced Short Palindromic Repeats
CSA	Chromogenic Substrate Assay
Cy5	Discosoma Red Fluorescent Protein

CypB	Cyclophilin B
Da	Dalton
DANN	Deoxyribonucleic Acid
DAPI	4',6-diamidino-2-phenylindole
ddH_2O	double-distilled water
DKO	Double Knockout
DMEM	Dulbecco's Modified Eagle Medium
DMSO	Dimethyl Sulfoxide
dNTPs	Deoxynucleotide Triphosphates
DPBS	Dulbecco's Phosphate-Buffered Saline
DpnI	Dam methylation-dependent nuclease I
dsDNA	Double stranded DANN
dsOligos	double stranded Oligomers
DsRed	Discosoma Red Fluorescent Protein
E. Coli	Escherichia coli
e.g	exempli gratia
EDEM	ER-degradation-enhancing 1, 2- mannosidase-like protein
EDTA	Ethylenediaminetetraacetic acid
EGFP	Enhanced Green Fluorescent Protein
ER	Endoplasmic Reticulum
ERAD	ER associated Degradation
ERGIC	ER Golgi intermediate compartment
ERp	Endoplasmic Reticulum Protein 57
Ex	Exon
F (primer)	Forward
FAM134B	Family with sequence similarity 134 member B
FASTA	Fast-All
Fc	Fragment crystallizable
FI,II, V,VII, VIII,IX,X,XIII	Coagulation Factors
FL- FVIII	Full length Factor VIII
g, mg, µg, ng	gram, milligram, microgram, nanogram
GABARAP	Gamma-Aminobutyric Acid Type A Receptor-Associated Protein
GABARAPL1	GABARAP Like 1
GABARAPL2	GABARAP Like 2
GAP	GTPase-activating Protein
GDF	GDI- Displacement Factor
GDI	Guanine Nucleotide Dissociation Inhibitor
GDP	Guanosine Diphosphate
GEF	Guanine Nucleotide Exchange Factor
GI	Glucosidase I
GII	Glucosidase II
Glc	Glucose
GlcNAc2	N-acetyl Glucosamine
GM130	Cis-Golgi Matrix protein 130
GPIb	glycoprotein Ib

gRNA	Guide RNA
GRP	GABARAP
GT	UDP-glucose: glycoprotein glucosyltransferase
GTP	Guanosine Triphosphate
HA	Hemophilia A
HEK293	Human Embryonic Kidney 293 cells
HepG2	Human Hepatocellular Carcinoma cells
hiFBS	Heat Inactivated Fetal Bovine Serum
His	Histidin
HPLC	High-Performance Liquid Chromatography
HRP	Horseradish Peroxidase
HSP	Heat Shock Proteins
i. e.	id est
I.E/I.U	International Unit
ICD	Immunogenic Cell Death
IF	Immunofluorescence
IgG	Immunoglobulin G
IP	Immunoprecipitation
$K_{association}$	Association Constant
KD	Equilibrium Dissociation Constant
$K_{dissociation}$	Dissociation Constant
KO	Knockout
K_{off}	Dissociation Rate Constant
K_{on}	Association Rate Constant
L,ml,µl	Liter, milliliter, microliter
LAMPI	Lysosomal-Associated Membrane Protein 1
LB	Luria Bertani
LC3/MAP1LC3	Microtubule-associated protein 1 light chain 3
LMAN1/ERGIC-53	Lectin, Mannose-Binding 1
LRP	LDL-receptor related protein
LSECs	Liver Sinusoidal Endothelial Cells
LW	Leer Wert
M,mM,µM,nM	Molar, millimolar, micromolar, nanomolar
mA	milliamper
Man	Mannose
MCFD2	Multiple Coagulation Factor Deficiency 2
MFGE8	milk fat globule-EGF factor 8, lactadherin
MgCl2	Magnesium Chloride
MgCl2	Magnesium Chloride
MW	Molecular Weight
MWCO	Molecular Weight Cut Off
N2a	Neuro 2a Cells
NaCl	Sodium Chloride
NBR1	Neighbor of BRCA1 gene 1
NP-40	Nonylphenol Ethoxylate-40
°C	Degrees Celsius

OCA	One -stage Clotting Assay
OptiMEM	Optimized Minimum Essential Medium
P/S	Penicillin/Streptomycin
PACE	Paired Basic Amino Acid Cleaving Enzyme
PAM	Protospacer Adjacent Motif
PCA	Principial Component Analysis
PCC	Pearson's Correlation Coefficient
PCM	Pericentriolar Matrix
PCR	Polymerase Chain Reaction
PDI	Protein Disulfide Isomerase
PE	Phosphatidylethanolamine
PEG	Polyethylene glycol
PFA	Paraformaldehyde
pH	Potential of hydrogen
PLEKHM1	Pleckstrin homology domain-containing family M member 1
PM	Plasma Membrane
pmol	Picomol
PPIase	peptidyl-prolyl *cis-trans* isomerase
PS	Phosphatidylserine
PT	Partial Prothrombin Time
PTM	Post Translational Modification
PVDF	polyvinylidene fluoride
R (primer)	Reverse
Rab	Ras-related proteins in brain
rcf	relative centrifugal force
RIPA	Radio-immunoprecipitation buffer
RISC	RNA-induced silencing complex
RNA	Ribonucleic Acid
rpm	Revolutions per minute
S.O.C	Super Optimal broth with Catabolite repression
s/sec, min, H	seconds, minutes, hours
S1,S2,S4	Samples
SD	standard deviation
SDS	Sodium Dodecyl Sulfate
SDS-PAGE	Sodium Dodecyl Sulfate-Polyacrylamide Gel Electrophoresis
Sec31a	SEC31 homolog A
siRNA	Small Interfering RNA
SKO	Single Knockout
SNARE	Soluble N-ethylmaleimide-sensitive factor attachment protein receptor
SPR	Surface Plasmon resonance
ssDNA	Dingle stranded DANN
ßME	ß-mercaptoethanol
ssOligos	single stranded Oligomers
SV40 ori	Simian Virus 40 origin of replication
***t*- SNARE**	Target Membrane SNARE

T7E1	T7 Endoculease I
TAE	Tris-acetate-EDTA
TBS	Tris-Buffered Saline
TBS-T	Tris-Buffered Saline with Tween-20
TF	Tissue Factor
TGN46	Trans-Golgi Network Protein 46
TRIM5α	Tripartite Motif Containing 5 Alpha
Ub	Ubiquitin
UPR	Unfolded Protein Response
V	Volt
***v*- SNARE**	Vesicles SNARE
V1,V2,V3	Variables
VAMP8	Vesicle-Associated Membrane Protein 8
vWF	von Willebrand Factor
w/v	weight/volume
WAC	WW Domain-Containing Adapter with Coiled-Coil
WB	Western Blot
WPB	Weibel-Palade body
WT	Wild Type
x g	G Force

1. Chapter 1: Introduction

1.1. The Coagulation ''Waterfall''

1.1.1. Blood Coagulation and Hemostasis

Our biological systems are composed of intertwined and complex sub-systems (nervous, immune, respiratory, musculoskeletal, digestive, urogenital, circulatory, and cardiovascular systems…etc.), which synchronize together to ensure equilibrated bodily functions. Blood, the vital component of the circulatory and cardiovascular systems, is present at an approximate volume of 5 liters in the human body, representing about 7% of total body weight [1, 2]. It consists of ***plasma*** and ***other components*** including red blood cells (erythrocytes), white blood cells (leukocytes), and platelets (thrombocytes). This fluid is very precious as its circulation supports a variety of essential functions, involving distribution and supply of nutrients and oxygen to various tissues and cells, waste removal, participation in immune responses (by delivering white blood cells and antibodies to foreign invaders), regulation of body temperature… Etc. [2]. One specific characteristic of the blood is its ability to switch its liquid physical state to a gel consistency, and to further solidify [3]. This switch is referred to as blood ''**coagulation''** or **''clotting''** [3].

Considering our dynamic nature as *Homo sapiens*, we are, at any time, prone to injuries which by turn might lead to minor, mild and sometimes major bleeding events depending on the severity of encountered accidents. These bleeding events, when occurred, are usually addressed by a mechanism in our bodies called **''Hemostasis''** [4]. Hemostasis comes from Greek roots with *–Haem/Heme (haîma)* meaning blood and -*Stasis* meaning stop or cessation[5], and was primarily described in medical practices by the Arab surgeon Abu Qasim Khalaf Ibn Abbas Al Zahrawi also known as Albucasis [6]. This process is governed by a variety of sequential steps, starting **first** with vasoconstriction, meaning contraction and constriction of smooth muscles present in the blood vessels to decrease blood flow and loss; **next** with a temporary formation of an initial platelet plug at the site of the injury; and **finally** with extended formation of

fibrin clots to stabilize initial platelet plugs or in other terms: *coagulation*. Hemostasis also consists of primary and secondary Hemostasis [7].

Primary hemostasis begins when vWF (von Willebrand Factor) is released from the damaged endothelium in response to an injury, reinforcing the binding of circulating platelets to the exposed collagen underneath the damaged blood vessel lining. Platelets adhere to collagen by binding through the collagen-specific glycoprotein Ia/IIa (GPIa/GPIIa) receptors located on their surface. Upon activation, platelets de-granulate releasing their content of signaling molecules such as adenosine diphosphate (ADP), platelet-activating factor (PAF), serotonin, platelet factor 4, vWF and thromboxane A_2 (TXA_2)[4]. These released components amplify platelet activation through a series of positive feedback cycles promoting further aggregation and recruitment of additional platelets leading to the formation of what is called a ''platelet plug''. Following episodes of primary hemostasis, blood coagulation factors are sequentially activated in a ''cascade or waterfall'' manner, ultimately leading to the formation of a fibrin clot and stabilization of the primary platelet plug as a final outcome [7, 8]. The latter constitutes ***secondary hemostasis*** [7, 8]. The terms ''Cascade'' or ''Waterfall'' simplify the nature of the undergoing processes of sequential protein activation that occur during blood coagulation [9].

Under normal homeostatic conditions, blood coagulation factors navigate the blood stream in their inactive forms (i.e. zymogens/procofactors/proenzymes), they get activated by limited proteolysis and act as serine proteases (active form) further activating downstream factors/proteins [3].

1.1.2. Extrinsic, Intrinsic and Common Pathways of Secondary Hemostasis

Secondary hemostasis is divided into three pathways: the **extrinsic** (i.e. tissue factor) pathway, the **intrinsic** (i.e. contact activation) pathway, which pour into the **common** pathway involving FX activation [8, 10].

The extrinsic pathway or tissue factor (TF) pathway is initially activated by exposure of the TF present in the injured sub-endothelial layer to blood circulating FVIIa. TF binds FVIIa to form the **extrinsic** tenase complex which subsequently activates FX into FXa.

Following the same manner of sequential activation, the contact activation pathway or the intrinsic pathway, begins with FXII conversion into FXIIa upon exposure to negatively charged damaged surfaces. FXIIa in turn activates Prekallikrein into Kallikrein, this in turn exerts a positive feedback and amplifies FXII activation. FXIIa then activates FXI into FXIa, which activates FIX into FIXa. FIXa binds FVIIIa to generate the intrinsic tenase complex. The intrinsic tenase complex significantly amplifies the activation of FX, increasing it up to 50 times more than the extrinsic (TF-FVIIa) tenase complex. This amplification enhances the overall effect on the common pathway. Following this, FXa pairs with FVa to form the prothrombinase complex, which converts prothrombin into thrombin. Thrombin then cleaves soluble fibrinogen proteins into fibrin which polymerizes to form insoluble fibrin strands. FXIII in turn cross-links these fibrin strands, further stabilizing the blood clot. The resulting structure forms a network that traps and stabilizes platelets and other components.

FV, FVIII, and FXIII are cleaved by the small amounts of thrombin present in the plasma. It is also important to note that the activity of these proteinase complexes requires the availability of both calcium and phospholipids [3, 8, 10].

1.1.3. Earlier and Current concepts of Secondary Hemostasis

Earlier models described the extrinsic and intrinsic pathways of secondary hemostasis as parallel processes that converge at the activation of FX **(Figure 1).** However, more recent understanding has reshaped this view, revealing that the intrinsic, or contact activation pathway, is not truly parallel but rather plays a role in amplifying thrombin generation which begins in the extrinsic pathway. In this updated model, the extrinsic tenase complex (TF-FVIIa) activates FIX and FX, leading to thrombin generation, after which the rest of the story proceeds in the common pathway **(Figure 2).** To further escalate this reaction, thrombin produced by the extrinsic pathway activates FVIII into

FVIIIa and FV into FVa, which then contribute to the formation of the intrinsic tenase and prothrombinase complexes [8, 10].

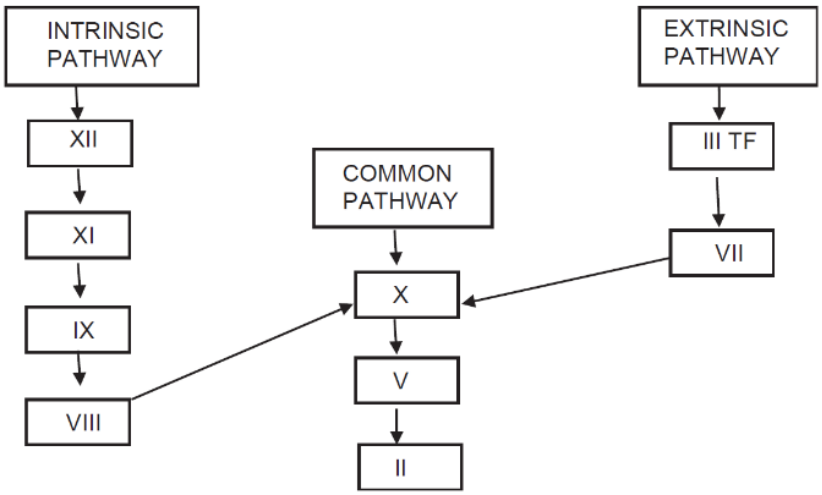

Figure 1. Earlier Concept of Coagulation.

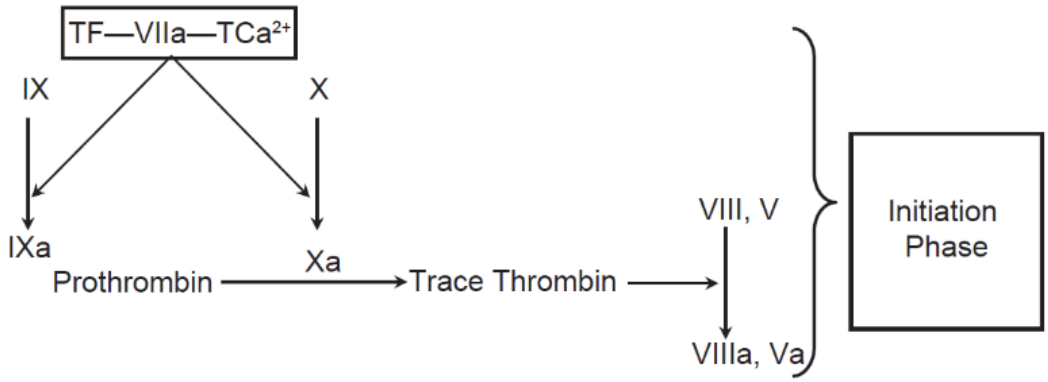

Figure 2. Current Concept of Coagulation (initiation phase).

1.1.4. Blood Disorders

In healthy conditions, proteins and coagulation factors involved in primary and secondary Hemostasis work together in harmony to regulate coagulation rates and optimize the speed of wound healing [3, 8-10]. However, these proteins may be influenced by factors, both quantitatively and qualitatively, leading to various and sometimes critical blood-related disorders [11]. Bleeding disorders are classified

into 4 categories according to the different phases of Hemostasis: **Vessel Wall Disorders**, **Platelet Disorders**, **Coagulation Disorders**, and **Fibrinolytic Disorders** [11]. **Vessel wall disorders** result from structural or functional abnormalities in the blood vessels, as seen in conditions like scurvy (vitamin C deficiency affecting collagen synthesis), Ehlers-Danlos syndrome (a genetic disorder that weakens vessel integrity), and hereditary hemorrhagic telangiectasia (Rendu-Osler-Weber syndrome), characterized by abnormal vessel formation [11]. **Platelet disorders** are divided into acquired or congenital types and further categorized as thrombocytopenias (reduced platelet count) or thrombocytopathies (dysfunctional platelet mechanisms)[11, 12]. Moreover, **coagulation disorders** arise from abnormalities in blood coagulation factors, causing impaired clot formation, as seen in von Willebrand disease, **Hemophilia types A,** B, and C (deficiencies in Factors VIII, IX, and XI, respectively)[11, 12], and various factor deficiencies (e.g., in Hageman factor (FXII), Stuart-Prower factor (FX), proaccelerin (FV), and fibrin-stabilizing factor (FXIII) and fibrinogen (FI))[11]. Additional coagulation-related issues include anticoagulant-related coagulopathies (e.g., from medications like heparin or warfarin) and disease-related coagulopathies (e.g., liver disease, vitamin K deficiency, and disseminated intravascular coagulation)[11]. Lastly, **fibrinolytic disorders** involve abnormal blood clot breakdown, where excessive fibrinolysis leads to bleeding due to increased clot degradation, and reduced fibrinolysis leads to thrombosis [11]. This is commonly due to deficiencies in the α2-plasmin inhibitor, plasminogen activator inhibitor, or Factor XIII, which compromises clot stability and elevates bleeding risk. For detailed classifications, refer to relevant research tables and papers[11].

1.2. Focusing the lens on FVIII

1.2.1. Early History of Hemophilia

The history of the Hemophilia diseases dates back centuries, with early references found as far back as the **2nd century** in the Talmud, which waived the requirement for boys' circumcision in cases where two previous brothers have bled to death due to the

procedure [13-15]. The Bible also described a woman suffering from prolonged bleeding for up to 12 years after which she healed, in addition, in the **10th century,** the arabic physician and surgeon Albucasis reported on families in which males died from exessive bleeding after injuries [6, 13, 14]. In **1803**, Dr. John Conrad Otto identified a bleeding disorder occuring in males, and in **1813,** Dr. John Hay suggested the transmission of this condition from affected fathers to their ''to-be-carriers'' daughters [13-16]. **In 1828**, the term "Haemorrhaphilia" was first introduced by a student called Friedrich Hopff and his professor Dr. Johan Lukas Schonlein in Zurich, which was later shortened to "Heamophilia''.[13, 14]

''Haemophilia'' was also refered to as the ''Royal disease'' [13, 14, 17]. This goes back to the fact of Queen Victoria, who ruled from **1837-1901**, being famously a carrier of Hemophila B (Christmas disease) [13, 14, 17]. The disease was passed on to one of Queen Victoria's sons, Leopold, who died in his early 30s due to complications from it [13, 14]. Hemophilia also spread to other European royal families, as intermarriage among royalty was common at the time [13, 14, 17].

1.2.2. Treatment Evolution of Hemophilia

Treatments for Hemophilia A (lack of FVIII) and B (lack of FIX) began evolving in the early **1900s**, starting with transfusions of fresh blood from relatives, followed by methods like inhaled oxygen, thyroid gland extracts, bone marrow, hydrogen peroxide, and even diluted snake venom [13, 14]. **In 1937**, Arthur Patek and FHL Taylor, physicians at Harvard, reported on the presence of the anti-hemophilic globulin protein, as an anticoagulant. Fresh plasma transfusions followed in the late **1950s** and early **1960s,** however, the amount of needed factors (FVIII and FIX) was insuffecient in the transfused plasma [13, 14]. The first description of the coagulation cascade saw the light in **1964,** in *Nature* which was published by the british hematologist Dr. Robert McFarlane [14, 18]. **In 1965**, Dr. Judith Graham Pool discovered that thawed and spinned down plasma produced a concentrated form of FVIII, advancing treatment significantly and introducing the use of cryoprecipitates to Hemophilia treatment strategies[13, 14, 19]. The **1970s** witnessed the development of freeze-dried powdered FVIII concentrates, which was made accessible to home infusions and an easy- reach for patients[13, 14]. Despite these advancements, the **1980s** brought challenges with the

spread of HIV/AIDS and Hepatitis C because of contaminated blood products [13, 20]. By **1992**, improved methods for viral inactivation (dry-heat, pasteurization, ultrafiltration and non-ultrafiltration viral inactivation techniques…etc) led to safer productions and manufacturing of blood products [13, 14] and in the **mid-1990s**, first synthetic recombinant FVIII and FIX products were introduced using recomibnantly expressing systems [21]. Overcoming the issue of contaminated blood products paved the way to establishing and accepting prophylactic protocols as well as to first administrations of by-passing products (such as FVIIa) in cases of inhibitor developement in patients treated using non-factor replacement therapies [13]. Replacement therapies for Hemophilia, including intravenous injections of FVIII and FIX, have also been improved by extending the proteins' half-lives[13]. This was achieved by fusing them with the Fc component of IgG1 or albumin, as well as by conjugating them with chemicals like polyethylene glycol (PEG)[13]. The half-life extension was particularly successful for FIX, achieving approximately a five-fold increase compared to its standard half-life[13]. In contrast, this extension was less effective for FVIII, with half-life improvements of only 1.5 to 1.7 times its standard half-life [13]. This reduced effectiveness is likely due to FVIII's dependence on the half-life of von Willebrand factor, its companion protein in the blood [13]. The **21st century** marked the introduction of purified FVIII and FIX blood products (without any plasma derivatives) and first gene therapy trials marking a new era and bringing the possibility of longer-term solution for Hemophilia patients[13, 22, 23]. Gene therapy has shown greater long-term success with FIX, achieving stable expression for up to 8 years. FIX's smaller size makes it easier to package into AAV (Adeno Associated Virus) vectors, which likely contributes to these lasting results[13]. For FVIII, researchers used a B-domain deleted form to simplify packaging and delivery. However, unlike FIX, FVIII's expression began to wane around 4 years post-delivery, suggesting ongoing challenges in maintaining its levels over time [13, 23].

1.3. Understanding the pre-life of FVIII: Intracellular trafficking and posed challenges

1.3.1. Genetics and Structure

The FVIII protein is encoded by the *F8 gene* which is located on the X chromosome (Xq28), it consists of 26 exons and 25 introns and mutations or disruptions in this gene might result in the X-linked recessive disorder: **Hemophilia A (HA)** [24, 25]. Hemophilia A could be classified into three categories: severe (<1% normal FVIII Activity), moderate (1%-5% of normal FVIII Activity) and mild (5%-40% FVIII Activity) and has an incidence of 1 per 5, 000-10, 000 males [24-26]. This classification could be linked to the type of mutation occuring in the *F8 gene*, which in turn defines the severity of the diesease. For instance, around half of HA patients (including severe cases) display an inversion of the intron 22 while 5% suffer from HA caused by an inversion of the intron 1 [24, 25]. More than 3,756 mutations in the *F8 gene* were reported until 2024 and could be found in Databases such as HAMSTeRS (The Hemophilia A Mutation, Structure, Test and Resource Site) database and CHAMP (The CDC Hemophilia A Mutation Project) database [24-26].

The domain structure of the FVIII protein consists of 2,332 amino acid residues which constitute the A1–A2–B–A3–C1-C2 domain structure [24, 25], resembling the structure of its homologue protein FV [24]. **(Figure 3)**

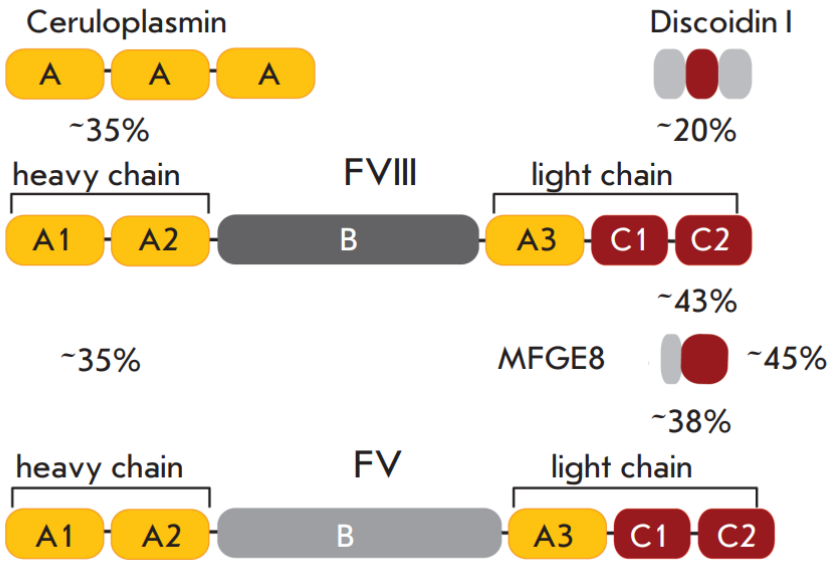

Figure 3. Domain structure of FVIII and FVIII homologs. Numbers represent the homology level of amino acids for domain groups. Discoidin I was obtained from D. discoideum; all other proteins were obtained from H. sapiens

The A domains represent around 30% homology with each other, with A domains of FV and Ceruplasmin. The A1 and A3 domains bind copper ions and stabilize the mature formed FVIII heterodimer [24, 25], while the A2 domain participates in FVIII binding to FIXa and its further conformational change during formation of the tenase complex [24]. The A domains are flanqued by smaller acidic domains (a1, a2 and a3 domains) representing the platform for thrombin cleavage[25]. FVIII's structure also includes C domains that are homologous to those of FV, to the C-terminal domain of MFGE8 (milk fat globule-EGF factor 8, lactadherin) and to the discoidin fragment I [24]. The C2 domain supports FVIII binding to vWF in plasma, upon secretion[24]. Coming to the larger domain of the FVIII polypeptide, the B domain is notable for being encoded by a single, continuous exon and for its extensive glycosylation [24, 25]. It contains 25 potential N-glycosylation sites, of which almost 16 to 19 are occupied [24]. It is noteworthy to clarify that FV and FVIII both share the specific characteristic of having a heavily glycosylated B-domain although their B domains do not share sequence similarity [24]. The B-domain appears to have no role in the blood stream and in the coagulant activity of FVIII since it must be cleaved before release. However, it is the domain through which FVIII interacts with proteins of the Endoplasmic Reticulum and the ERGIC compartment based on carbohydrate recognition, which highlights an intracellular role [24, 25]. Cleavage of the B-domain in the Golgi aparatus by the *trans*-Golgi protease PACE/Furin is very critical to further genrate the mature ''to be-secreted'' FVIII protein [24].

1.3.2. Intracellular Journey of the FVIII protein

1.3.2.1. Endoplasmic Reticulum Primary Quality Control

FVIII is synthesized and secreted in the liver by Liver Sinusoidal Endothelial Cells (LSECs), however, due to the challenges encountered while cultivating primary LSECs and their complex and sensitive requirements, most knowledge and information on the intracellular life of FVIII emerge from investigating its artificial expression in recombinant systems (HEK293, BHK, CHO cells…Etc.)[24, 25, 27-30]

During translocation to the Endoplasmic Reticulum, the FVIII client protein, like any other nascent glycoprotein, undergoes primary N-glycosylation, where oligosaccharide cores, composed of three terminal glucose residues, nine mannose residues, and two N-acetyl Glucosamine residues ($Glc_3Man_9GlcNAc_2$), attach to asparagine amino acids (mostly present in the B-domain of FVIII)[24, 25, 31]. Within the ER, glucosidases I and II act by trimming the last two terminal glucose residues, leaving FVIII with a mono-glycosylated sugar structure ($Glc_1Man_9GlcNAc_2$)[31, 32]. FVIII has been reported to interact specifically with three components of the primary Quality Control (CQ) system during its sojourn in the ER: **Calnexin** (CANX), **Calreticulin** (CALR), and **BiP** [24, 25, 33, 34]. The primary quality control system generally operates at a broader level, and intends retaining proteins within the ER until they are properly folded and achieve stability to undergo further trafficking [31, 32].

FVIII interacts with CANX and CALR by the same mechanism, earlier named ''the CANX-cycle'' [32]. CANX and CALR recognize mono-glycosylated glycoproteins and interact with them through their lectin domains [32]. These interactions hold and slow down the dynamic flux of newly synthesized glycoproteins, providing them the necessary time to achieve mature conformations [31, 32]. Once properly folded, glycoproteins are allowed to leave the ER if their roles require further trafficking and extracellular secretion [31, 35]. For a successful protein quality control, Calnexin and Calreticulin cooperate with additional ER chaperones, such as ERp57, CypB (Cyclophilin B), and ERp29. All three interactions were identified to be mediated by the shared Calnexin/Calreticulin P-domains, and serve as catalyzers for disulfide bond formation, isomerization and proper folding of the nascent glycoprotein [31, 32]. In this context, Calnexin and Calreticulin act as bridges bringing into proximity newly synthesized glycoproteins to other ER components [32]. Moreover, It is believed that the initial interaction with glycoproteins in the ER is mediated by association with Calreticulin and Calnexin first, an event which by turn recruit other ER components, thereby marking the start of the protein-protein interaction events [36].

ERp57 also known as ER-60, GRP58, or PDIA3, is a member of the protein disulfide isomerase (PDI) family, which oxidoreductase activity becomes enhanced upon

interaction with Calnexin/Calreticulin [32, 36]. However, unlike archetypal PDI, which is a general ER chaperone, ERp57 functions specifically as a newly synthesized glycoprotein- specific ER chaperone [36]. Association of ERp57 with newly synthesized glycoproteins also depends on their structure and the trimming activity of the Glucosidases I and II, as for Calnexin and Calreticulin, meaning its binding is also restricted to and stabilized by the formation of disulfide bond with mono-glycosylated glycoproteins [36].

Another protein which binds Calnexin and Calreticulin through the same interaction site as ERp57 is CypB [32, 37]. CypB is a peptidyl-prolyl *cis-trans* isomerase (PPIase) associated with ER stress, proven to play a role in the folding and maturation of collagen and transferrin, respectively [32]. Unlike other ER resident proteins, -which ER residency depends on specific retention signals-CypB remains retained in the ER through interaction with Calreticulin [37]. One supportive proof of this is the reported binding of the immunosuppressant Cyclosporin A to CypB, a mechanism that drove CypB outside of the ER to the plasma membrane for subsequent further secretion [38].

ERp29 is a homologue to PDI (protein disulfide-isomerase), however lacking a thioredoxin domain, therefore the redox activity [32]. The exact mechanism through which ERp29 operates in the ER and binds to newly synthesized proteins remains not fully understood nor investigated. Nevertheless, studies have demonstrated participation of ERp29 in trafficking and biosynthesis of cystic fibrosis transmembrane conductance regulator (CFTR), proinsulin, thyroglobulin and other proteins. It is speculated that ERp29 facilitates the packaging of correctly folded proteins into COPII vesicles, and contributes in ER-Golgi trafficking. In addition, roles such in regulating ER stress and unfolded protein response (UPR) have been as well attributed to ERp29 [39].

All three ER chaperones bind Calnexin and Calreticulin in their P-domain. Binding of Calnexin/Calreticulin to glycoproteins (0.7 µM) has been demonstrated to be stronger than their binding to either of the three ER chaperones, ERp57, ERp29 and CyB (5-15 µM), indicating that Calnexin and Calreticulin bind longer to N-glycosylated proteins than to ER chaperones, allowing ER chaperones to alternate in their association to glycoproteins [31, 32].

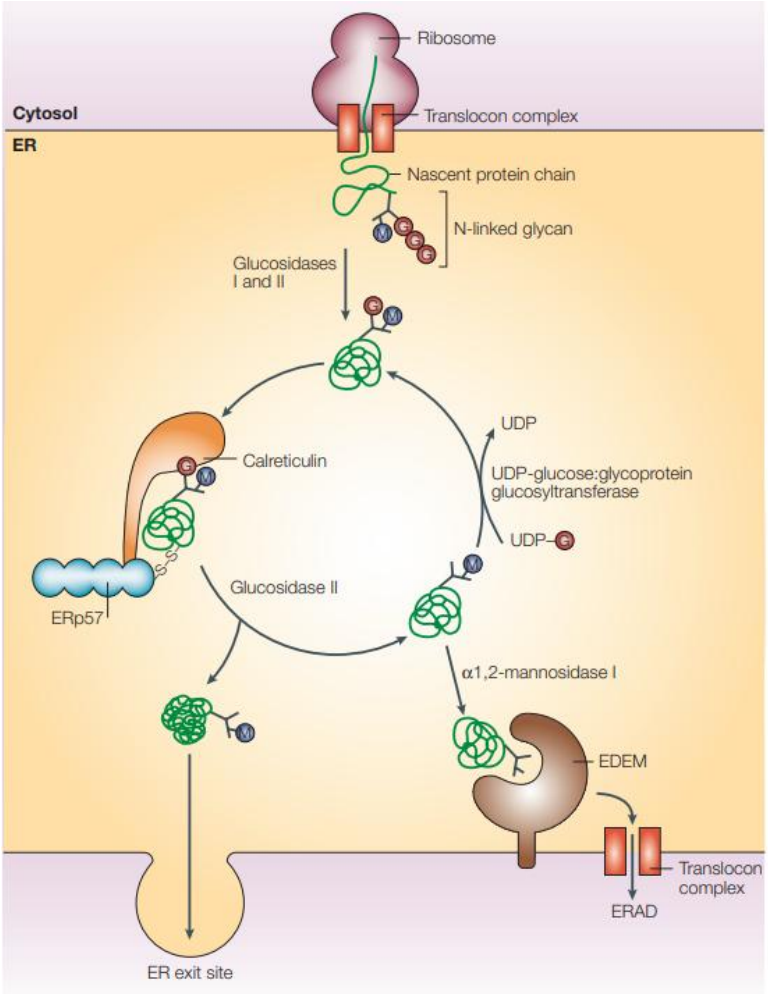

Figure 4. Illustration of the calnexin/careticulin cycle.

Both CANX and CALR share a similar domain structure, consisting of lectin domains (Glycan and Ca^{2+} binding domain), P-domains (ER-Chaperone binding domain), and acidic domains (containing the RKPRRE motif responsible for ER-retention)[40]. The domain structure of CANX, unlike CALR, harbors a transmembrane domain (TM-domain), allowing it to anchor the ER membrane. CALR lacks this domain, which making it soluble within the ER lumen [31, 32, 40]. CALR, in contrast to CANX was documented outside of the ER lumen (nucleus, cytosol, plasma membrane…etc.) and

harbors a C-terminal KDEL retrieval signal motif [32, 41, 42].Upon proper folding of FVIII, the final glucose residue is trimmed by the activity of glucosidase II, preparing the protein for further transport to the Golgi apparatus[31]. Misfolded/Unfolded FVIII protein, however, undergoes re-glycosylation cycles (by UDP-glucose: glycoprotein glucosyltransferase (GT)) and further repeated recognition by the quality control machinery [31]. Permanently unfolded/misfolded FVIII moieties are cleaved by ER α-1, 2-mannosidase I leaving FVIII with 8-mannose residues, a property which allows its recognition by EDEM (ER-degradation-enhancing 1, 2- mannosidase-like protein) and its diversion from the CANX/CALR cycle to Proteasomal degradation through the ER-associated degradation (ERAD) pathway [31, 43]. Additionally, both CANX and CALR play critical roles in calcium regulation, further highlighting their importance in maintaining ER function and homeostasis [32, 40, 42, 44]. **(Figure 4)** [31]

1.3.2.2. Aggregation/Oligomerization, Energy Requirements and Secretion Challenges

FVIII also interacts with the ATPase BiP (GRP78), a member of the HSP70 family (heat shock proteins), and a component of the protein quality control taking place in the endoplasmic reticulum [25, 31], where BiP binds FVIII within the A1 domain (79 aa within residues 253-331) [33, 34]. Unlike FVIII and vWF, FV does not interact with BiP [33]. This interaction has been reported to be more stable for FVIII than for vWF [45]. Interestingly, this correlates with FVIII's lower secretion efficiency in comparison to FV and vWF [45, 46]. Studies have also shown that the dissociation of BiP from its targeted substrates requires the presence of ATP [45]. In addition, when ATP levels were depleted using CCCP (protonophore carbonyl cyanide 3-chlorophenylhydrazone), which disrupts oxidative phosphorylation events and uncoupling of the proton gradient, and interferes with lysosomal degradation [47, 48]. FVIII secretion was more severely affected even by slight amounts of the chemical, while much higher concentrations of CCCP were required to inhibit secretion of FV or vWF [45, 46]. These studies confirm that BiP-interacting substrates differ in their degree of association with the ATPase chaperone, and further highlight the higher ATP thus energetic requirements for FVIII dissociation and release for further post-ER trafficking [45, 49].

Another key feature that distinguishes FVIII from other glycoproteins is its ability to form reversible amyloid-like aggregates/oligomers within the ER [34, 50]. This mechanism is mediated by a specific β-sheet in its A1-domain (79-amino-acid motif residues 253-331) which is responsible for polymerization and seeding of the aggregation, and which was termed: 'Aggron' by [34]. Interestingly, investigating mutations in this A1 domain of FVIII has shown clear and obvious effects on its secretion, where secretion levels increased in F309S and L303E/F309S [ES] mutations, decreased in 7LF>A and F306W mutations and were mildly affected in L300V/ L303E/F309S [VES] and L294T/L303E/F309S [TES] mutations [34]. Moreover, as tested by CA membrane retention procedures in different cell lines (COS-1, CHO-K1 and HepG2), FVIII secretion was inversely proportional to FVIII retention and aggregation in the ER [34]. In the same study, Poothong et. al [34] have also demonstrated that the 'Aggron' motif interacts with both FVIII variants : Full-length- and B-deleted-domain FVIII molecules, as well as the ATPase BiP. Based on this, they further explored the overexpression effect of BiP on the destiny of FVIII aggregation and they have found that higher levels of not only BiP, but also Calnexin and Calreticulin, in addition to higher glucose supplementation (which produces more ATP by glycolysis), resulted in successful resolving and reversible disaggregation of FVIII [34].

The fact that FVIII is a highly ATP and energetic demanding protein poses a challenge on the endogenous as well as recombinant systems expressing this protein, and therefore on its secretion yields as evidenced in literature [25, 33, 34, 45, 50]. Undergone investigations on biopharmaceutical and bio-therapeutics production in recombinant models such as CHO cells, revealed that mammalian cells have the ability of suppressing the secretion of proteins that are energetically and metabolically costly to produce, if non-essential. A comparison of endogenously expressed proteins to recombinantly expressed biotherapeutics like Rituximab, and FVIII revealed that recombinant proteins require significantly more ATP molecules during biosynthesis. They have also found that, unless essential, energy-intensive proteins were suppressed to prioritize and favor the synthesis and secretion of less costly proteins and that CHO cells growth rate was as well compromised when producing to favor protein synthesis over cell growth in this case. Besides, they have pointed out the

variation in energy demands for various proteins, and demonstrated that these requirements are not necessarily influenced by protein-size but rather by the complexity of the degree of complexity of processes undergone by proteins intracellularly up until secretion, such as protein quality control in the ER, vesicle trafficking and post-translational modifications. Moreover, industrial bio-production relies on recombinant systems for efficiency like CHO cells which seem to regulate secretion to better balance system's homeostasis. Knocking down non-essential high-cost proteins has been suggested as a strategy to improve yields, as demonstrated in studies on coagulation factor VIII, which is recombinantly expressed for therapeutic uses.[49, 51]

To better understand these dynamics, further investigation into the interplay between Chaperone-mediated processes, ER quality control mechanisms, post-translational modifications, vesicles trafficking and the energetic requirements of FVIII folding and secretion is critical. This is essential to uncover the mechanistic basis of FVIII's interaction with chaperones and its retention and aggregation in the ER.

1.3.2.3. Transport and Packaging of FVIII in the ER-Golgi Compartment (ERGIC)

Once FVIII is properly folded and cleared to exit the ER, it is marked by the trimming of the last glucose residue, leaving an oligosaccharide core consisting of nine mannose residues [31]. This structure interacts with LMAN1 and MCFD2, two mannose-binding proteins, which consist a part of the secondary protein quality control system [24, 25, 31]. LMAN1 (lectin, mannose-binding 1) and MCFD2 (multiple coagulation factor deficiency protein 2) form a cargo complex that transports FVIII with the aid of COPII vesicles from the endoplasmic reticulum to the Golgi apparatus via the ERGIC compartment [52-54]. LMAN1, also called ERGIC-53 (named after its molecular weight of 53 kDa), exists as homo-hexamers, or more recently as a homo-tetramer [55], in cells and is ER- membrane-bound protein [32, 40, 52-54]. Like CANX, LMAN1 has a transmembrane domain that anchors it to the ER membrane [32, 55]. Its cytosolic-tail harbors a diphenylalanine ER exit motif which is intended for interaction with COPII vesicles (anterograde trafficking) at ER exit sites, as well as a dilysine ER retrieval

sequence that ensures the protein is recycled back to the endoplasmic reticulum, and which interacts with COPI vesicles (retrograde trafficking) [35, 53, 54].

MCFD2, a smaller, soluble monomeric protein of 16 kDa, is characterized by two C-terminal calmodulin-like EF-hand domains, capable of binding calcium, its cargo receptor complex partner LMAN1 and FV/FVIII [52-54]. LMAN1 forms a 1:1 stoichiometric complex with MCFD2, and together, they escort glycoproteins, including FV, FVIII, and alpha-1 antitrypsin, to the ERGIC compartment [52-54]. Defects or mutations in LMAN1 or MCFD2 can result in an autosomal recessive disorder known as combined deficiency of FV and FVIII, as both factors depend on this cargo-receptor complex for efficient trafficking and transport [54]. LMAN1 interacts with FV/FVIII and MCFD2 through its CRD (carbohydrate recognition domain) domain at distinct non-overlapping sites [53]. Evidence suggests that both LMAN1 and MCFD2 can bind FV and FVIII, however the shuttling function of the cargo-receptor complex is disrupted in case LMAN1 fails to oligomerize or if its interaction with MCFD2 is impaired [53, 54].

It was proposed that MCFD2 is the primary effector responsible for recruiting FV and FVIII to the LMAN1-MCFD2 complex, while LMAN1 facilitates their transport and the transport of MCFD2 [52]. LMAN1 also plays a role in retaining MCFD2 in the ER [52]. In the absence of LMAN1, MCFD2 is secreted and scarcely detected within cells [54]. The oligomerization of LMAN1 is not crucial for binding FV/FVIII but is essential for binding MCFD2 [53]. Monomeric LMAN1 fails to exit the ER and cannot co-immunoprecipitate MCFD2 [53, 54].

Once FVIII is successfully escorted to the Golgi apparatus, the cargo receptor components, transport vesicle members, and other aiding proteins release their cargo and recycle back to the endoplasmic reticulum, maintaining ER homeostasis and ER-membrane integrity [24, 31, 35].

1.3.2.4. FVIII in the Golgi Apparatus

Proteins that successfully undergo ER quality control and are packaged into COPII vesicles proceed through the ER-Golgi intermediate compartment (ERGIC) before

reaching their next destination: the Golgi apparatus. The Golgi apparatus is morphologically composed of stacks or ''cisternae'' which are divided into the *cis*-Golgi network-oriented toward the nucleus- followed by the medial-Golgi compartment, and finally the *trans*-Golgi network, where proteins are sorted for further trafficking. In the *trans*-Golgi network, proteins may be directed to the endosomal system (lysosomes), to the plasma membrane, or to be further secreted to the extracellular space. Protein progression through the Golgi apparatus is usually believed to occur via intra-Golgi vesicular transport or through the maturation of Golgi cisternae and stacks, and move from the *cis*- to the *trans*-Golgi. Upon entering the Golgi apparatus, FVIII, like any a glycoprotein, undergoes critical post-translational modifications (PTMs). N-glycans, which were initially attached during protein synthesis in the ER, undergo further modifications. This involves the removal of mannose residues and the addition of N-acetylglucosamine, galactose, and sialic acid residues, refining the glycan structures essential for the function of glycoproteins. Additionally, further modifications such as O-glycosylation and tyrosine sulfation are introduced at specific sites, influencing FVIII's stability and activity.

Importantly, the sorting of proteins within the *trans*-Golgi network is influenced by these post-translational modifications. for example, the phosphorylation of mannose residues in N-glycan structures instead of their removal dictates trafficking towards lysosomes.

Furthermore, secretion from the *trans*-Golgi network occurs via two main mechanisms: constitutive and regulated secretion. Constitutive secretion allows proteins destined for the plasma membrane or extracellular space to be continuously secreted, whereas regulated secretion involves concentration of the proteins in secretory vesicles until a specific stimuli triggers their release (e.g. hormones, enzymes, neurotransmitters…etc). No clear evidence on specific FVIII *trans*-Golgi secretion mechanism have been clearly elucidated until date.

Another key event in FVIII maturation occurs in the trans-Golgi, where the precursor FVIII protein undergoes enzymatic cleavage by Furin/PACE at residues R1313 and R1648. This cleavage generates the heavy and light chains of FVIII, a critical step for its functional activation. These post-translational modifications and processing steps

ensure that FVIII attains its biologically active form before secretion, enabling its essential role in the coagulation cascade. [24, 25, 56]

1.4. Endomembrane system, Autophagy and the GABARAP family

Throughout its biosynthesis and trafficking, FVIII localizes within components of the endomembrane system, a network of membranous organelles and vesicles such as the ER and the Golgi Aparatus [24, 25]. This system also includes further components like the nucleus, the lysosomes, with some evidence including the autophagosomes, and transport vesicles, the peroxisomes… etc [57]. It is true that the endomembrane system includes a wide variety of enclosed organelles and vesicles, however, pathways governing its dynamics could be divided into three categories: **anterograde** trafficking which involves trafficking of nascent proteins from the ER to the Golgi aparatus and theron to further destinations, the **endocytic pathway** which mainly includes protein internalization events and recycling in the endosomal system, and the **retrograde** pathway which is defined by the backward trafficking of proteins and cellular material from the ERGIC and Golgi aparatus back to the ER [58, 59].

The trafficking of proteins within the endomembrane system requires specific vehicles and itineraries. These translate in the cellular unit as mechanisms involving vesicle ''budding and fusion'' (e.g. COPII vesicles in ER and ERGIC- **anterograde** trafficking, COPI vesicles in *cis*- Golgi and ERGIC compartment **retrograde** trafficking and clathrin coated vesicles in **endocytosis** events at the plasma membrane and sorting between *trans*-Golgi and the endosomal system) [59, 60]. Upon processing in the *trans*-Golgi network, proteins are directed toward various destinations: 1) lysosomes and the endosomal system, 2) directly to the plasma membrane for secretion via the constitutive secretion (default) pathway, or 3) stored in secretory vesicles, which release their contents upon specific signals in a regulated secretory manner **(Figure 5)** [61]. The transport and delivery of proteins from the *trans*-Golgi apparatus to the plasma membrane is referred to as **exocytosis**. Intracellular pathways serving these vesicles are selected based on factors like PTMs: e.g. the phosphorylation of mannose residues belonging to the N-glycan core of glycoproteins, by mannose-6-phosphate for

lysosomal hydrolases directs vesicles carrying these proteins toward lysosomes. Besides, in specialized tissues and cells, protein delivery to the extracellular space may be either delayed or accelerated depending on the protein, the state of its cargo proteins as well as the necessity for its production, trafficking, and secretion. This regulation is evident in processes such as neurotransmitter release in the nervous system, enzyme secretion in the digestive system, activation of proteins from precursor forms into their mature, functional variants... etc, all of which plays and

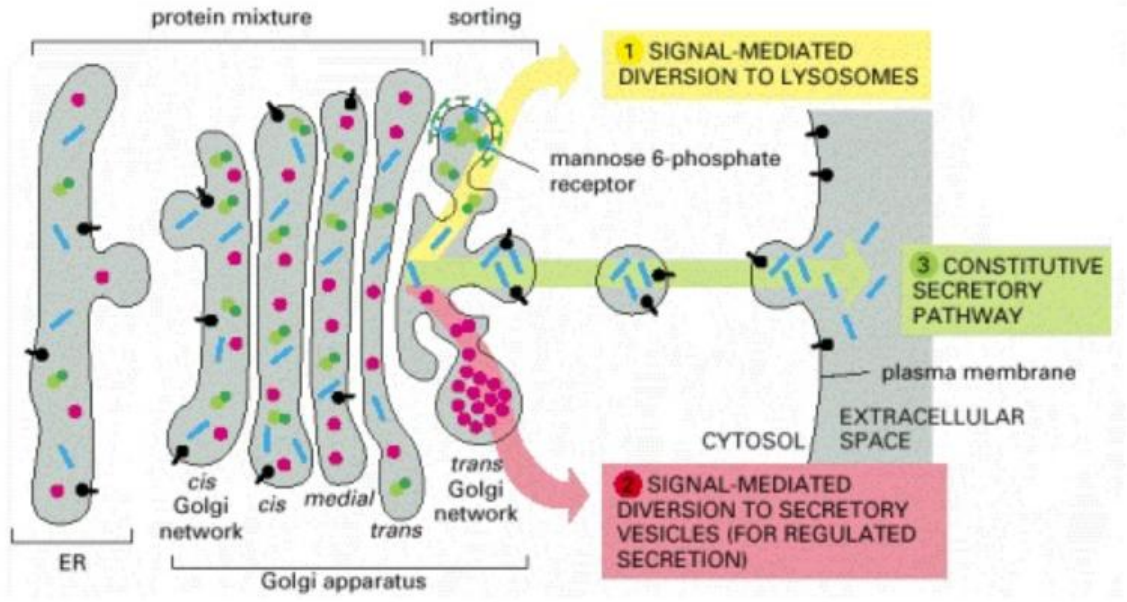

Figure 5. The Three Best-understood Pathways of Protein Sorting in the *trans*- Golgi Network.

essential role in commanding specific vesicle formation and pathway contribution in order to achieve successful cargo delivery [61]. Furthermore, vesicle formation, budding, fusion, and orientation are regulated by specific proteins that determine their origin, destination, and final site of fusion and content release (e.g. Rab GTPases, SNAREs…etc.) [57, 59, 60, 62-64]. The following section will further explore the types of proteins involved in this process and the mechanisms guiding vesicle trafficking.

In general, vesicle transport is regulated by a series of proteins, including **Coat**, **Tether**, **Rab**, and **SNARE** proteins. For this to occur, two types of membranes are required: a *"donor"* membrane and an *"acceptor"* membrane [62]. Initially, transmembrane

proteins containing cargo protein sorting signals, along with **coat** proteins, initiate the budding of flat membranes into round-shaped buds that encapsulate the cellular material or proteins to be transported, in the ''donor'' membrane [62]. Once formed, these vesicles are **transported** either by diffusion or by utilizing the cytoskeleton as a highway [62]. Before

direct vesicle fusion into ''acceptor'' membranes, **tethering** proteins play a critical role in the process [62]. Tethering could be defined as follows: it is when Rabs, which are small GTPases belonging to the Ras superfamily, together with tether proteins, govern the preliminary interaction steps between a vesicle and its target/acceptor membrane ensuring vesicle closeness to the target membrane prior to fusion [62]. Initially, Rabs are inactive in the cytosol, and are known to be in a bound-state to GDP and is associated with a guanine nucleotide dissociation inhibitor (GDI). Rabs are then recruited to membranes by the Guanine nucleotide displacement factors (**GDF**: GDI-displacement factor). Once at the membrane, guanine nucleotide exchange factors (GEFs) facilitate the exchange of GDP for GTP, resulting in Rab proteins activation. Once activated Rab-GTP bound interacts with subsequent effectors to mediate processes of vesicle tethering and fusion. The cycle is completed when GTP is hydrolyzed to GDP by GTPase-activating proteins (GAPs), returning the Rab to its inactive state, in which it was initially in the cytosol [62]. The final step in vesicle transport and movement is **fusion**. This step is known to be mediated by the SNARE proteins. SNARE proteins are existing under two forms: *v*-SNARES (SNARES on the vesicles) and *t*-SNARES (SNARES on the target membranes). Fusion events are the result of pairing between v- and t-SNARES, this creating a trans- SNARE complex, that itself drives vesicle-membrane fusions [62]. **(Figure 6)** [62]

Although massive research has been conducted on FVIII and its contribution in therapeutic advancements of Hemophilia A, the understanding of its detailed vesicular intracellular trafficking remains poor. However, evidence on secretion of FVIII in LSECs under normal conditions[27] as well as its release and secretion upon specific stimuli (like Epinephrin) [65], FVIII appears to have the potential of undergoing all three sorting mechanims and both constitutive and regulated secretion. Nevertheless, the literature

and the research still lacks this information and it would be of great value to investigate this branch of the intracellular life of FVIII [24, 25, 66].

In this thesis, in addition to already established FVIII-interacting proteins, proteins of the autophagy machinery, also known as autophagy-related proteins or Atg8-related proteins, were adressed. Autophagy is a "self-eating" process characterized by the targeting of unnecessary cellular components, such as debris, damaged proteins and organelles, pathogens…etc for lysosomal degradation [67]. This process helps maintain cellular homeostasis and energetic cell properties by recycling the resulting degraded material [68].

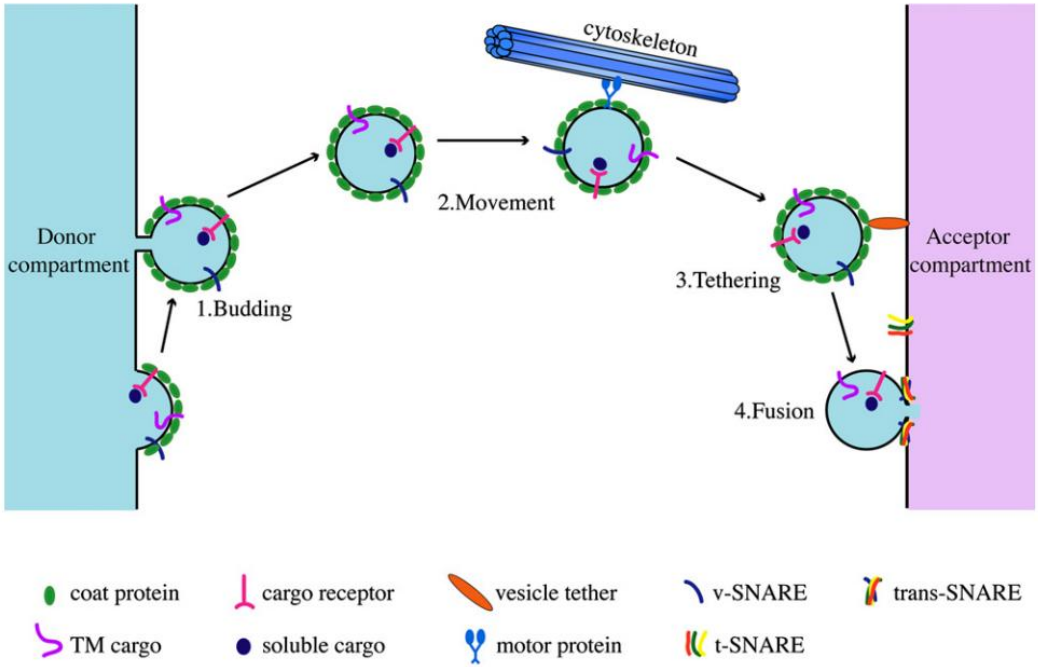

Figure 6. The Four Essential Steps in Vesicle Transport.

The Atg8 protein family is highly conserved in eukaryotes, existing as a single Atg8 protein in yeast (*Saccharomyces Cerevisiae*) but with multiple homologs in *Homo sapiens* [67, 69]. It has recently been confirmed that the Atg8-family of proteins is divided into three subclasses: the **LC3s** (MAP1LC3A, MAP1LC3B, MAP1LC3B2, MAP1LC3C), the **GABARAPs** (GABARAP and GABARAPL1), and GATE-16 or **Golgi-associated ATPase enhancer of 16 kDa** (GABARAPL2) [67, 69]. These proteins are known to participate in vesicular organization, autophagosome formation, and fusion with lysosomes during

autophagy [67, 69]. They are also involved in other cellular processes, such as protein trafficking, maintaining Golgi structure, and playing roles in diseases, including tumor suppression and neurodegenerative disorders [67, 70].

One characteristic of the autophagy related proteins is that In order for them to anchor autophagic vesicles, they must undergo a lipidation process or lipidization or Phosphatidylethanolamine (PE) as a post-translational modification [67, 69, 71]. This process resembles ubiquitin conjugation and occurs as follows [71]: It begins with the cleavage of an Atg8 protein by Atg4, exposing a C-terminal glycine residue (Atg8-**I**). Subsequently, Atg8 is activated by Atg7 and then transferred to Atg3. Following this, Atg8 proteins get attached to PE or PS with the assistance of multimers of Atg12–Atg5/Atg16 complexes [67, 69, 71]. Upon lipidation, the Atg8-**II** protein becomes capable of anchoring to the vesicular membranes [67, 69, 71] .

Despite homologies within the Atg8-family **(Figure 7)** [72], functional differences exist. For example, the LC3 subfamily is primarily involved in nucleation, assembly, and elongation of the phagophore/autophagosome, while the GABARAP subfamily plays a more prominent role in later stages, mediating autophagosome maturation and further fusion events with lysosomes [67, 73]. This thesis focuses specifically on the GABARAP proteins, with particular emphasis on GABARAP itself. The biological functions of the GABARAP proteins are challenging to separate due to their significant amino acid sequence similarity, which often leads to functional overlap, shared protein interactions, and compensatory mechanisms [72]. For instance, both GABARAP and GABARAPL1 bind to the γ2 subunit of $GABA_A$ receptor and assist in its trafficking to the plasma membrane in postsynaptic spaces of the nervous system [74, 75].

Recent studies using single and double fluorescent tagging of endogenous GABARAP proteins (CRISPR/Cas9-mediated fusion of N-Terminal Clover/ScarletI with a 3xFlag epitope) have revealed that only 20-40% of their punctate structures overlap intracellularly, indicating specific internal dispersion for each of the GABARAPs [76]. Although GABARAP and GABARAPL1 share a variety of interactions and mechanisms, GABARAPL1 is distinctively found in plasma membranes, whereas GABARAP primarily

localizes to intracellular vesicles [72]. Furthermore, post-translational modifications, expression patterns, lipidation (PE-conjugation), and transcriptional regulations of each GABARAP protein influence their interactions and dynamics. For instance, GABARAPL1 and GABARAPL2 undergo more efficient PE-conjugations than GABARAP and other members of the Atg8 family by exhibiting higher affinities for ATG4 protein isoforms [72]. Moreover, GABARAP was specifically reported to interact with the Cis-Golgi Matrix Protein GM130 [77]. The interaction between GABARAP and GM130 in the cis-Golgi apparatus is modulated by the protein WAC (WW Domain-Containing Adapter with Coiled-Coil). It was described that WAC binding to GM130 reduces GM130's interaction with GABARAP, thereby promoting starvation-induced autophagy by releasing GABARAP to the centrosomal matrix [77].

Calreticulin, a well-established interaction partner of FVIII, shares similarities with GABARAP in its ability to perform multiple roles and function across various cellular compartments, rather than being confined to a single one [44, 78, 79]. Furthermore, GABARAP and Calreticulin interact with each other, an observation confirmed by in vitro assays such as phage display screening, fluorescence titration, SPR (Surface Plasmon Resonance) spectroscopy, and cell-based experiments involving neural or tumor cells (e.g., brain lysate extracts, N2a, and AMO1 cells) [80, 81].The absence of GABARAP also diminish Calreticulin surface exposure during immunogenic cell death (ICD), leading to perturbed phagocytosis, disruption of Golgi apparatus integrity, and interruption of autophagy in multiple myeloma cells [82, 83]. However, despite these observed effects of GABARAP loss, the precise mechanism underlying its interaction with Calreticulin and the exact site of this interaction remain unknown. These

observations have so far been documented only for GABARAP, with no similar evidence for GABARAPL1 or GABARAPL2.

Figure 7. LC3/GABARAP family protein alignment. *:conserved amino acids, gray: glycine for PE conjugation. Yellow: potential phosphorylation. Green: potential Acetylation.

1.5. Aims of the Study

This thesis forms part of a larger research project primarily focused on understanding the intracellular mechanisms and processing of the coagulation Factor VIII (FVIII) protein. Previous studies conducted by our research group (AG El-Maarri) identified a potential interaction between the GABARAP protein and FVIII through a yeast two-hybrid screen. These findings initiated investigations into the role of GABARAP in FVIII trafficking, with the aim of elucidating its specific contributions and mechanisms.

The **primary objectives** of this doctoral thesis are as follow:

- To investigate the role of the GABARAP protein in FVIII biogenesis, trafficking, and processing by employing a variety of experimental approaches**,** including generations of CRISPR/Cas9 single and double knockout, interaction assays, immunofluorescence microscopy, chemical treatments targeting specific intracellular pathways, and detailed data quantification and analysis.

- To compare the impact of GABARAP to control (Calnexin, Calreticulin, LMAN1 and MCFD2) and homologous (GABARAPL1, GABARAPL2) proteins on FVIII intra- and extracellular profiles.

- To better understand the FVIII journey in the endomembrane system, specifically trans-Golgi sorting events, as well as possible alternative intracellular machineries associated with FVIII secretion.

2. Chapter 2: Materials

2.1. Biological Material

Organism	Name	Supplier
Bacterial Strains	One Shot™ TOP10 Chemically Competent E. coli *(Escherichia coli)*	Thermo Fischer Scientific
Cell lines	HEK 293 cells	SIRION Biotech GmbH

2.2. Reagents and Chemicals

Reagent/Chemical	Supplier
Agarose	Biozym Scientific GmbH
Ampicillin	Sigma-Aldrich
BB2 buffer	Thermo Fischer Scientific
Bovine Serum Albumin (BSA)	Sigma-Aldrich
Brefeldin A (BFA)	Cayman Chemical Company
Calcium Chloride ($CaCl_2$)	Merck Group
Chloroquine (CQ)	Cayman Chemical Company
CID 1067700 (Rab7 Inhibitor)	Sigma-Aldrich
cOmplete mini, EDTA-free (Protease Inhibitor Cocktail)	ROCHE Diagnostics
Dimethyl Sulfoxide (DMSO)	AppliChem GmbH
DNA Ladder (1 kb , 100 bp)	Thermo Fischer Scientific
DNA polymerases	Thermo Fischer Scientific
dNTPs (Deoxynucleotide Triphosphates)	Thermo Fischer Scientific
DpnI	Thermo Fischer Scientific
EDTA	Sigma-Aldrich
Ethanol (Isopropanol)	Carl Roth GmbH + Co. KG
Gelatin	Sigma-Aldrich
Glycine	Carl Roth GmbH + Co. KG
Glycerol	Merck Group
Heat Inactivated Fetal Bovine Serum	ThermoFischer Scientific
Heat Inactivated Fetal Bovine Serum – Hi value	ThermoFischer Scientific
Heat Inactivated Fetal Bovine Serum – Sera plus	ThermoFischer Scientific
HPLC grade water	Sigma-Aldrich

Immersion 40x Objective Oil	Carl Zeiss AG (Carl Zeiss)
Immobilon Western HRP Substrate	MilliporeSigma
Laemmli Sample Buffer (2x, 4x)	Bio-Rad Laboratories
LB (Luria Bertani) Broth	Sigma-Aldrich
Lipofectamine™ 2000 Transfection Reagent	ThermoFischer Scientific
Loading Dye (6x)	ThermoFischer Scientific
Magnesium chloride ($MgCl_2$)	Carl Roth GmbH + Co. KG
Methanol	Merck Group
Midori Green	Nippon Genetics
Novex™ Tricine SDS Sample Buffer 2x	ThemoFischer Scientific
PageRuler™ Plus Prestained Protein Ladder, 10 to 250 kDa	ThermoFischer
Paraformaldehyde	Sigma-Aldrich
Penicillin/Streptomycin	ThermoFischer Scientific
ProLong™ Glass Antifade Mountant	ThermoFischer Scientific
ProLong™ Mounting Medium with NucBlue	ThermoFischer Scientific
Proteinase K	Thermo Fischer Scientific
SDS pellets	Carl Roth GmbH + Co. KG
Skim Milk Powder	MilliporeSigma
Sodium Acetate	Sigma-Aldrich
Sodium Chloride (NaCl)	Merck Group
ß-mercaptoethanol	Carl Roth GmbH + Co. KG
S-solution	Thermo Fischer Scientific
Tris	Carl Roth GmbH + Co. KG
Triton-X100	Sigma-Aldrich
Trypsin	ThermoFischer Scientific
Tween-20	Sigma Aldrich

2.3. Media for Culture of Mammalian Cells and Bacterial Strains

Media	Supplier
Dulbecco's Modified Eagle Medium – High Glucose, Pyruvate	ThermoFisher Scientific
Dulbecco's Modified Eagle Medium (without Glucose)	ThermoFisher Scientific
Dulbecco's Modified Eagle Medium (without Glucose/Glutamate)	ThermoFisher Scientific
Dulbecco's Modified Eagle Medium (without Glutamate)	ThermoFisher Scientific

Opti-MEM Reduced Serum Media	ThermoFisher Scientific
Super Optimal broth with Catabolite repression (S.O.C) Medium	ThermoFisher Scientific

2.4. Buffers and Solutions

2.4.1. Self-made Buffers

Buffer Name	Buffer Composition
Binding Buffer	500 mM NaCl, 1mM $CaCl_2$, 0.04% (v/v) Tween-20, 0.5% (w/v) BSA in 100 ml 1x PBS, pH= 7
IF Antibody Solution (1% BSA)	1% w/v BSA, 0.1% (v/v) (25 ml blocking solution : 2.5 ml 10% BSA, 25 µl Triton-X100 in 22.5 ml 1x PBS)
IF Blocking Solution (1 % BSA)	0.3 M Glycine, 1% w/v BSA, 0.1% (v/v) Triton-X100 (50 ml blocking solution : 1.12 g Glycine, 5 ml 10% BSA, 50 µl Triton-X100 in 45 ml 1x PBS)
LB (Luria Bertani) Agar Medium	17.5g LB Agar Broth (powder) in 500 ml water autoclaved then cooled down and supplemented with corresponding antibiotic
LB (Luria Bertani) Medium	10g LB Broth (powder) in 500 ml water autoclaved then cooled down and supplemented with corresponding antibiotic
miSeq Buffer	10 mM Tris, 0.9 mM $CaCl_2$, 2.9 mM $MgCl_2$, 0.5 M EDTA, 1% (v/v) Triton- X100, pH= 7 (100 ml miSeq Buffer: 0.12g Tris, 0.01g $CaCl_2$, 0.028g $MgCl_2$, 18.61 g, 1 ml Triton-X100 in water)
Neutralization Buffer	1M Tris, pH= 8 (1.2 g Tris in 10 ml water)
Paraformaldehyde (PFA) (4%)	4% (w/v) in 1x PBS, pH= 6.9 (40 g PFA powder in 1 L 1x PBS)
TAE (Tris-acetate-EDTA) Buffer (50x)	40 mM Tris, 20 mM acetic acid, 1 mM EDTA in 1 L of water
TBS (Tris-Buffered Saline) (10x)	100 mM Tris, 1.5 M NaCl, pH= 7.6 (1L 10x TBS: 12.11 g Tris, 87.6 g NaCl in water)
TBS-T (Tris-Buffered Saline with Tween-20) (1x)	For 1x diluted TBS buffer , 0.1% Tween-20 is added (1L 1x TBS: 1ml Tween-20)
WB Blocking Solution (Milk based)	2.5 g Skim Milk Powder, 50 ml 1x TBS-T, 25 µl Tween-20

WB Membrane Stripping Buffer	200 mM Glycine, 3.5 mM SDS, 5 ml Tween-20, pH= 2.2 (500 ml Stripping Buffer : 7.5g Glycine, 0.5 g SDS pellets, 5 ml Tween-20 in water)
WB Transfer Buffer (blotting buffer) (10x)	250 mM Tris, 1.92 M Glycine, 0.01% (w/v) SDS, pH = 8.3 (1L 10x Transfer Buffer: 30.28 g Tris, 144.13 g Glycine, 10 ml 1% SDS in water)

2.4.2. Readily Purchased buffers

Buffer Name	Supplier
Phosphate-Buffered Saline DPBS (1x)	ThermoFisher Scientific
Novex™ Tricine SDS Running Buffer 10x	ThermoFisher Scientific
NP-40 (Nonylphenol Ethoxylate-40) Buffer	ThermoFisher Scientific
Radio-immunoprecipitation buffer (RIPA) buffer	Sigma- Aldrich
Tris/Glycine/SDS Buffer (WB running buffer) 10x	Bio-Rad Laboratories

1.5. SDS-PAGE Gels

Gel	Supplier
16% Novex™ Tricine Mini Protein Gels	ThermoFisher Scientific
4–15% Mini-PROTEAN® TGX™ Precast Protein Gels	Bio-Rad Laboratories
7.5% Mini-PROTEAN® TGX™ Precast Protein Gels	Bio-Rad Laboratories
8–16% Mini-PROTEAN® TGX™ Precast Protein Gels	Bio-Rad Laboratories

1.6. Recombinant Proteins

Recombinant Protein	Supplier
BDD- FVIII (moroctocog alfa: Refacto® 1000 I.E.)	Pfizer
BDD- FVIII (simoctocog alfa: Nuwiq® 1000 I.E.)	Octapharma

Full-length FVIII (Octocog alfa: Advate® 1000 I.E)	Takeda
Full-length FVIII (octocog alfa: Kovaltry® 1000 I.E.)	Bayer
Plasma-derived FVIII (Beriate® 1000 I.E)	CSL Behring
Plasma-derived FVIII (Octanate® 1000 I.E)	Octapharma
rGABARAP (C-terminal-his-tagged) 20 µg	Cusabio

1.7. Biosensors (Bio-Layer Interferometry)

Biosensor Type	**Supplier**
Octet® Anti-HIS (HIS2) Biosensors	SARTORIUS
Octet® Streptavidin (SA) Biosensors	SARTORIUS

1.8. Commercial Kits

Commercial Kit	**Supplier**
BigDye™ Terminator v1.1 Cycle Sequencing Kit	ThermoFisher Scientific
Capturem™ IP & Co-IP Kit	TAKARA
Dade® Innovin® and Factor V deficient Plasma	Siemens Healthineers
DNeasy Blood and Tissue Kits for DNA Isolation	Qiagen
EZ-Link™ Sulfo-NHS-LC-Biotin, No-Weigh™ Format kit	ThermoFisher Scientific
Factor VIII Chromogenic Assay kit	Siemens Healthineers
GeneArt™ CRISPR Nuclease Vector with CD4 Enrichment Kit (with competent cells)	ThermoFischer Scientific
GeneArt™ Genomic Cleavage Detection Kit	Thermo Fisher
INNOVANCE® VWF Ac/Ag assay kit	Siemens Healthineers
iProof™High-Fidelity PCR Kit	BioRad
Luminescent ATP detection assay kit	Abcam
Owren's Veronel Buffer	Siemens Healthineers
Phusion High Fidelity PCR Kit	ThermoFisher Scientific
PureLink™ HiPure Plasmid Midiprep Kit	ThermoFisher Scientific

PureLink™ HQ Mini Plasmid DNA Purification Kit	ThermoFisher Scientific
QIAquick Gel Extraction Kit	Qiagen

1.9. List of Antibodies

Antibody	Supplier	Use	Reference Nr.
Anti-Mouse HRP	Abcam	WB	6789
Anti-Rabbit HRP	Abcam	WB	6721
ARL8B	Proteintech	IF	13049-1-AP
Calreticulin	Santa Cruz	IF	Calregulin (H-170) sc-11398
Calreticulin	Abcam	WB	Ab22683
COPB (COPI)	Santa Cruz	IF	COPB (D-10) sc-393615
Donkey anti-Mouse Alexa Fluor 488	ThermoFisher scientific	IF	A-21202
Donkey anti-Rabbit Alexa Fluor 488	ThermoFisher scientific	IF	A11008
Donkey anti-Rat Alexa Fluor 488	ThermoFisher scientific	IF	A-21208
Donkey anti-Sheep Alexa Fluor 594	ThermoFisher scientific	IF	A- 11016
Furin	Abcam	IF	3467
FV	Haematologic technologies	IF/WB	AHV-5146
FVIII	Affinity Biologicals	IF	SAF8C-AP/ AP1871-BR1
GABARAP	Novus Biologicals	IF	MAB8574/ Clone#853641
GABARAP	Cell Signaling Technology	WB	E1J4E
GABARAPL1	Proteintech	IF	11010-1-AP
GABARAPL2	Cell Signaling Technology	IF	D1W9T
GM130	Cell signaling Technology	IF	D6B1
Goat anti-Mouse Alexa Fluor 488	ThermoFisher scientific	IF	A-11029
Goat anti-mouse Alexa Fluor 555	ThermoFisher scientific	IF	A-21422
Goat anti-Mouse Alexa Fluor 633	ThermoFisher scientific	IF	A-21052
Goat anti-rabbit Alexa Fluor 594	ThermoFisher scientific	IF	A-11012
Goat anti-Rabbit Alexa Fluor 633	ThermoFisher scientific	IF	A-21071
LAMPI	Cell Signaling Technology	IF/WB	D2D11
LC3B	Abcam	IF/WB	51520

LMAN1 (ERGIC-53)	Santa Cruz	IF/WB	ERGIC-53 (B-9) sc-271517
MCFD2	Santa Cruz	IF	MCFD2 (F-3) sc-390463
PDI	Cell Signaling Technology	IF	C81H6
Rab11	Cell Signaling Technology	IF	D4F5
Rab26	Proteintech	IF	14284-1-AP
Rab5	Cell Signaling Technology	IF	C8B1
Rab7	Santa Cruz	IF	Rab7 (B-3) sc-376362
Rab8	Cell Signaling Technology	IF	D22D8
Sec31a (COPII)	Cell signaling Technology	IF	D1G7I
TGN46	SIGMA ADLRICH	IF	T576
Ubiquitin	Santa Cruz	IF	Ubiquitin (F-11) sc-271289
VAMP8	Santa Cruz	IF	Endobrevin (G-12) sc-166820
vWF	Agilent Technologies	IF/WB	GA527

1.10. Plasmids and Vectors

Vector/Plasmid	**Supplier**
Calnexin (CANX) (NM_001746) Human Tagged ORF Clone	OriGene
Calreticulin (CALR) (NM_004343) Human Tagged ORF Clone	OriGene
GABARAP expression plasmid (designed)	VectorBuilder
LMAN1 (NM_005570) Human Tagged ORF Clone	OriGene
MCFD2 (NM_139279) Human Tagged ORF Clone	OriGene
pcDNA3.1-WT-vWT Plasmid	Addgene
pMT2-V [GI 5138] 40515	ATCC

1.11. Designed Oligonucleotides (Megaprimer insertion in CRISPR/Cas9-vectors)

Vector	**Inserts**	**Primers Sequences**
CRISPR CD4 Nuclease Vector $^{+}$	gRNA- LMAN1-F	TAT ATA TCT TGT GGA AAG GAC GAA ACA CCG TCACTCGGTCGCTTCGTCCG

	gRNA- LMAN1-R	ATT TTA ACT TGC TAT TTC TAG CTC TAA AAC CGGACGAAGCGACCGAGTGA
	gRNA- GABARAP-F	TAT ATA TCT TGT GGA AAG GAC GAA ACA CCG GTTCGAGAAGCGCCGCTCTG
	gRNA- GABARAP-R	ATT TTA ACT TGC TAT TTC TAG CTC TAA AAC CAGAGCGGCGCTTCTCGAAC

2.12. Primers

Primer	Sequence
LMAN1_ F	5'-CAG CTG CTC CTG GCC GTG-3'
LMAN1 _R	5'-ACA GCG CAT ATG GTG TGC-3'
LMAN1 _R	5'-CAG GGT AGC CGC GGA TGA-3'
LMAN1 _F	5'-GCT CTG CCA ATC AGC GAG-3'
MCFD2 _R	5'-ATA CCT GAC TTA TAG GTG-3'
MCFD2_F	5'-TGA CAA GCT CTC TTC CTA-3'
GABARAP-F	5'-TCC GCT GAA TCC GCC CGC-3'
GABARAP-R	5'-GGT CGA CTA GTG ATT CAA TC-3'
CALR-R	5'-ACT CGC GAG GAC CCT CGA CT-3'
CALR-F	5'-AGC TTG TGG CTC TCG GCA GA-3'
CANX-R	5'-CTG AGT AGT TGA GAC TAC AT-3'
CANX-F	5'-ATG AGA GAG TGG TTA GTG AT-3'
GABAL1_F	5’-ATG CAG CTA TAA CCT CAT GAA-3’
GABAL1_R	5’-ATC AGA TAA CTC CAG AGC AT-3’
GABAL1_ F	5’-GAC AGT GAG ACT TCA TCT CA-3’
GABAL1_R	5’-GAG CAT TAC CAG TAA GGT C-3’

2.13. List of siRNAs

siRNA	Supplier	Reference Nr.
AllStars Neg. Control	QIAGEN	SI03650318
Hs_CALR_1_FlexiTube siRNA	QIAGEN	SI00062874
Hs_CALR_8_FlexiTube siRNA	QIAGEN	SI02654589
Hs_CALR_9_FlexiTube siRNA	QIAGEN	SI02777096
Hs_CANX_1_FlexiTube siRNA	QIAGEN	SI00027636
Hs_CANX_6_FlexiTube siRNA	QIAGEN	SI02663367
Hs_CANX_7_FlexiTube siRNA	QIAGEN	SI02757300
Hs_GABARAP_1_FlexiTube siRNA	QIAGEN	SI00096194

Hs_GABARAP_4_FlexiTube siRNA	QIAGEN	SI00096215
Hs_GABARAP_5_FlexiTube siRNA	QIAGEN	SI03105795
Hs_LMAN1_4_FlexiTube siRNA	QIAGEN	SI00078988
Hs_LMAN1_7_FlexiTube siRNA	QIAGEN	SI04933334
Hs_MCFD2_5_FlexiTube siRNA	QIAGEN	SI03135496
Hs_MCFD2_6_FlexiTube siRNA	QIAGEN	SI04243764
Hs_MCFD2_7_FlexiTube siRNA	QIAGEN	SI04257225

2.14. Labware

Labware	**Supplier**
BioTek Microplate Reader	Agilent Technologies
Cell culture Plates (10cm, 6-12-24-48-96 wells)	Sarstedt
Cover Slips (18 mm)	Marienfeld
Cryotube Vials	Eppendorf
Falcons (15- 50 ml)	Eppendorf
Whatman Filter papers (WB)	Cytiva
Filters (0.2 µm)	VWR
Filtertips	Eppendorf
Micropipettes	Eppendorf
Microtubes (1.5-2 ml)	Eppendorf
Neubauer Cell Counter	Marienfeld
Parafilm	Bemis Company Inc.
Pasteur pipettes	VWR
PCR-strips	Carl Roth GmbH + Co. KG
Petri-dishes	Corning
PVDF Membrane	Carl Roth GmbH + Co. KG
Slides	Marienfeld
Tips	Eppendorf
Tissues	Fuhrmann GmbH
Via2-Cassette™	Chemometec
Whatman lens Cleaner	Cytiva

2.15. Equipment

Equipment/Machine	**Supplier**
3500xL Genetic Analyzer	Hitachi Applied Biosystems

Agarose Gel Electrophoresis Chamber	Bio-Rad
ApoTome (Fluorescence Microscope)	Carl Zeiss
Centrifuge	Eppendorf, Sigma- Aldrich
ChemiDoc	BioRad
CO_2 Incubator	PHCbi
Fridge (-150^oC)	PHCbi
Hemostasis Analysis System	Sysmex CN 6000
Incubator	Memmert
Laminar Hood	Labogene SCANLAF
Light Microscope	Olympus
Nitrogen Tanks	Consartic, Bio 36
NucleoCounter ® NC-202™ (cell counter)	Chemometec
Rocker	PegLab
SDS-PAGE Chamber	Bio-Rad
Spectrophotometer (NanoDrop)	PegLab
Table Centrifuge	Eppendorf
Thermal Shaker	Edmund Bühler GmbH
ThermoCycler	Bio-Rad
Thermomixer	Eppendorf
Vortexer	Junke und Kunkel IKA
Water Bath	Thermo Fischer Scientific

2.16. Softwares

Program	**Application**
Microsoft Office 2016, Endnote (Word, Excel, Power Point)	Dissertation Preparation, Data Organization, Data and statistical analysis, Figure preparation, Presentation
Prism- Graphpad	Statistical Analysis, Figures Preparation
Qlucore Omics Explorer	Advanced Statistical Analysis and Data Visualization
Geneious R/Prime	Sequence Alignment
Benchling Online Tool	Sequence Search and Alignment
ClustVis Online Tool	Advanced Data Analysis and Visualization
Zen Blue 2.6 pro	Image Co-localization and Analysis
Nucleotide Data bases	NCBI gene bank, Ensembl
Protein Sequence Data Bases	Uniprot
Sequence Search	BLAST, BLAT
BLItz Pro™	Bio-layer Interferometry Data Analysis

ImageLab	Gel (Electrophoresis, SDS-PAGE) Visualizations
NC-View™	Cell Counting
CellProfiler 4.2.8	Image Analysis, Organelle Quantification

3. Chapter 3: Methods

3.1. General Protocols (Routinely Performed Experiments)

HEK293 parental cell line and modified HEK 293 cells ($HEK28^{WT}$, CRISPR/Cas9-KOs) were cultured using the following protocol.

3.1.1. Cultivation of Mammalian HEK293 cells

3.1.1.1. Thawing and Maintaining HEK293 Cells

Cryovials containing stored/frozen HEK 293 cells were pre-warmed in a 37°C water bath. Cells were then diluted in complete Dulbecco's Modified Eagle Medium (DMEM) containing 10% heat-inactivated fetal bovine serum (hi-FBS) and 1% Penicillin-Streptomycin (P/S), and centrifuged at a speed of 1,200 rpm for 2 minutes. Old media was aspirated, discarded and replaced by fresh complete DMEM. Cells were then plated onto 10 cm plates, and left to incubate in a 5% CO_2 humidified incubator.

When the cells reached approximately 70-80% confluence, old media were removed, and cells were washed with 1x DPBS. After removing the PBS, 1x Trypsin was added (2ml Trypsin for 10 cm plates), and the cells were incubated for 2 minutes either at room temperature or 37°C. Following incubation time, cells were detached by gently tapping the edges of the culture dishes/plates, then collected in three times the volume of the added Trypsin (6ml complete DMEM). Cell suspensions were transferred to 15 mL falcons and centrifuged at a speed of 1,200 rpm for 2 min. The supernatant was carefully aspirated and discarded to retain an intact cell pellet. The latter was then re-suspended in the desired amount of fresh complete DMEM, depending on the duration of cell maintenance. Cells were then either re-plated onto new 10 cm culture dishes for maintenance, or counted if further downstream experiments were required. Cell counting was performed using the automated NucleoCounter ® NC-202™ from chemometec or the manual counting technique using a Neubauer Chamber, and seeded into the desired plates (6 wells, 12 wells, 24 wells, 48 and 96 wells plates) at required concentrations.

3.1.1.2. Cell Counting

i. NucleoCounter ® NC-202™

The NucleoCounter® NC-202™ is the 3rd generation cell counter provided by Chemotec, which is a cassette-based instrument. Cells must first be drawn into a special cassette, the Via2-Cassette™, and then loaded into the instrument. With a simple press of the run button, the NC-View™ software automatically calculates the cell count per mL of solution, the amount of cell debris and aggregates, as well as generates a full report on viability rates and information about the size/morphology of the counted cells, when already provided with the dilution factor and sample volume. Based on the viable cell count, dilutions of cells were prepared before seeding/plating.

ii. Neubauer 0.1 mm Chamber (Hemocytometer)

After cell re-suspension in fresh DMEM, cells were diluted 1:10 (10 µl cell suspension in 90 µl DMEM or PBS). 10 µl were loaded into the Neubauer Chamber (upper or lower big square). Calculations were made according to the following formula:

$$\text{Cell Concentration } \left(\frac{\text{cells}}{\text{ml}}\right) = \frac{\text{Cell count per square (S)}}{\text{number of counted squares (S)}} \times \text{Dilution Factor} \times 10^4$$

10^4 accounts for the volume of each square (0.1 mm depth and 0.04mm^2 area)

(Figure 8)

Example of Calculation

Suppose counts in four small squares: 15, 20, 17, and 19 and my DF= 10

$$\text{Cell Concentration } \left(\frac{\text{cells}}{\text{ml}}\right) = \frac{(15+20+17+19)}{4} \times 10 \times 10^4$$
$$= 1.775 \times 10^6 \text{ cells/ml}$$

***(Note**: in case we want to calculate cell number/concentration in the full volume or plate, we must multiply by the media volume in which the cells were re-suspended following centrifugation. Example:* $1.775 \times 10^6 \times 5 = 8.875 \times 10^6$ *cells in* $5\ ml$*)*

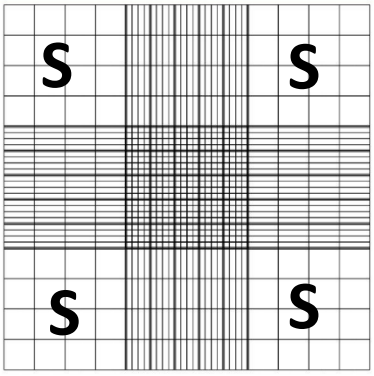

Figure 8: Schematic Representation of the Neubauer Chamber. S squares represent the 4 small squares of the area in which cells must be counted.

3.1.1.3. HEK293 cells Stock Preparation

To preserve WT and modified cells, stocks were prepared and stored in liquid nitrogen tanks until further use. Cells were split, and at a confluence of 60-70%, they were spun down and re-suspended in a 1 mL mixture of DMEM supplemented with hi-FBS and P/S, along with Dimethyl Sulfoxide (DMSO) (and more hi-FBS if needed).

(For example: 900 µL complete DMEM + 100 µL DMSO, or 500 µL complete DMEM + 400 µL Hi-FBS + 100 µL DMSO).

Cells were then kept overnight at -80°C in a Mr. Frosty cooling container, a cryopreservation freezer filled with ethanol, to ensure gradual cooling and avoid any damage or shock to the cells. Cells were transferred on the next day to nitrogen tanks and stored there until further use.

3.1.2. Transfection by Lipofectamine™ 2000 (Lipid-Based Gene Delivery)

All transfection-based experiments in HEK293 cells were carried out using the Lipofectamine™ 2000 transfection reagent. Cells were seeded in complete DMEM into either 6, 12 or 24-well culture plates, depending on the optimal number of cells needed for downstream transfection analysis/verification, and left to grow at 37°C

until reaching 70-80% confluence in a 5% CO_2 humidified incubator **(Day 1).** At approximately 70-80% confluence, the media were replaced with reduced serum media (Opti-MEM 1x) to ensure better transfection efficiency. DNA samples (of CRISPR/Cas9-KO and expression vectors) were pre-diluted to a concentration of 200 ng/µl in ddH_2O. To achieve the desired final DNA concentration, specific volumes of the pre-diluted DNA stock were used. Lipofectamine and DNA samples were further diluted in Opti-MEM 1x, incubated for 5 minutes at room temperature, then combined (1:1 ratio) and further incubated for 20 minutes at room temperature before being added to the cells. Following addition of the DNA- Lipofectamine mixture to the cells, cells were left for 4 hours at 37°C in a 5% CO_2 humidified incubator, after which the media were switched back to complete DMEM **(Day 2).** 48 to 72 hours following transfection, media were collected for necessary FVIII activity measurements, cells were lysed for Western Blot procedures, and plates were microscopically visualized if required **(Day 4 or 5). (Figure 9. Table 1).**

Note: in case cells did not reach expected confluence on the second day, they were left in culture for another additional 24 hours. Transfection procedures in this case started on the 3^{d} day.

Table 1. Details corresponding to different plate formats (6, 12, and 24 well plates) used during transfection procedures.

	6 wells Plates	12 wells Plates	24 wells Plates
Mixture OptiMEM/Lipofectamine	140 µl OptiMEM + 10 µl Lipofectamine	75 µl OptiMEM + 5 µl Lipofectamine	37.5 µl OptiMEM + 2.5 µl Lipofectamine
Mixture OptiMEM/DNA (stock conc. 200 ng/µl)	140 µl OptiMEM + 5-30 µl DNA (200 ng/µl)	75 µl OptiMEM + 2.5-15 µl DNA (200 ng/µl)	37.5 µl OptiMEM + 1.25– 7.5µl DNA (200 ng/µl)
Mixture Lipofectamine/ DNA	300 µl	150 µl	75 µl
DNA Final Concentration	1-6 µg	1-6 µg	1-6 µg
Cell number	1 x10^6 cells/well	500 x10^3 cells/well	250 x 10^3 cells/well

Note: for transfection of FV and vWF in HEK293p, HEK28^{WT} and CRISPR/Cas9- single knockouts, cells were transfected using 2µg of vWF and 4µg FV expression plasmids. 4 hours later, media were switched to: an expression-media formula for FV (Opti-MEM™ Reduced Serum Medium supplemented with 5% BSA, 1mM CaCl2, 1% P/S) and to complete regular DMEM formulation for vWF. 48 hours later, media were collected for FVIII, FV and vWF measurements. FVIII activity was measured using a two-stage chromogenic assay, FV activity by one-stage clotting assay and vWF activity and antigen levels using INNOVANCE® VWF Ac assay and Ag assay (immunoturbidimetric assay). Cells were also fixed in parallel with 4% paraformaldehyde and prepared for further immunofluorescence staining of FV and vWF.

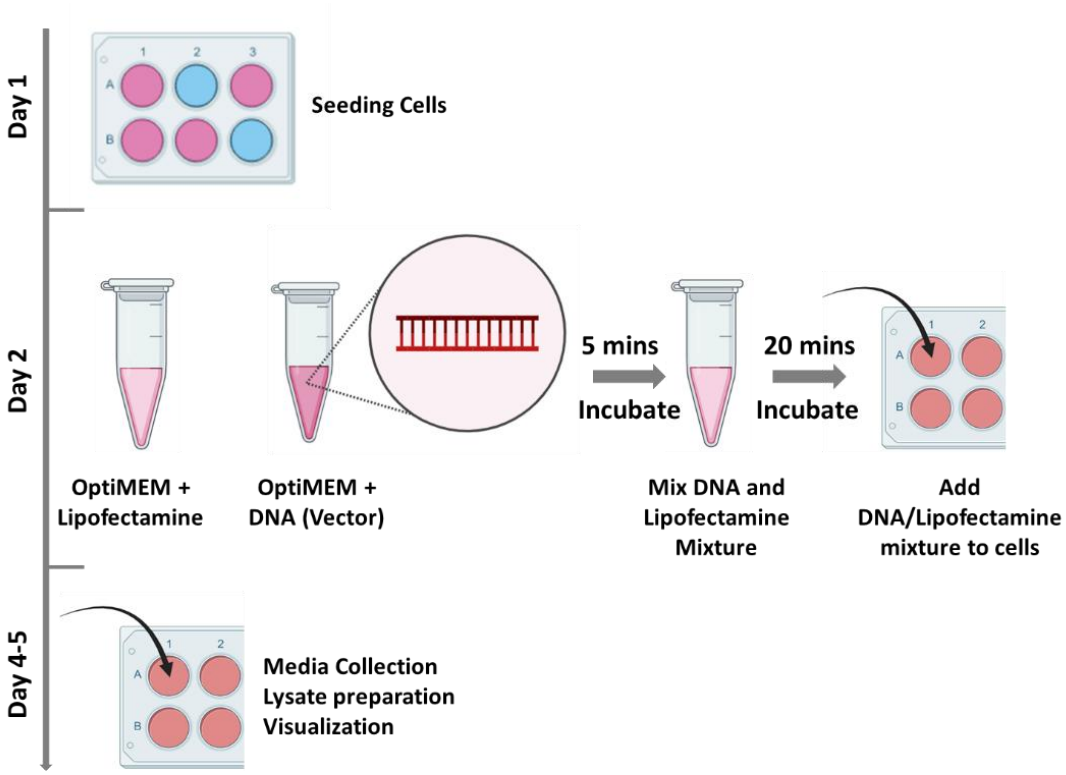

Figure 9. General workflow of Lipid-based Gene Transfection Procedures using Lipofectamine™ 2000. Figure generated in BioRender.

3.1.3. Coagulation Assays

3.1.3.1. Measurement of FVIII activity (FVIII: C) by two-stage chromogenic substrate Assay (CSA)

In the first stage of the assay, Factor VIII (FVIII) in FVIII-containing samples (such as cellular media and recombinant FVIII products) was activated by thrombin (FIIa). The activated FVIII was then mixed with activated Factor IX (FIXa), Factor X (FX), phospholipids, and calcium ions (Ca^{2+}) and incubated for 2 to 10 minutes, allowing FX to be activated into FXa (FXa). At this point, the amount of activated FXa reflects the functional FVIII present in the samples. In the second stage, thrombin was inactivated to stop the reaction, and a chromogenic substrate—a FXa-specific peptide nitroanilide substrate—was added. FXa cleaves the substrate, releasing p-nitroaniline, a colored product that can be measured using a spectrophotometer (Sysmex NC 6000). The

assay was performed using the Factor VIII Chromogenic Assay kit from Siemens Healthineers. **(Figure 10. A)**

3.1.3.2. Measurement of FVIII and FV activity by one -stage clotting Assays (OCA)

PT (prothrombin Time-FV) and a-PTT (Activated Partial Thromboplastin Time-FVIII)

Samples were prepared by serial dilution and mixed with FVIII/FV deficient plasma, followed by incubation with phospholipids and a contact surface activator (e.g., silica, kaolin, celite, ellagic acid or sulfatides for FVIII) or Tissue Factor (Thromboplastin for FV). Calcium (for FV) or Calcium Chloride (For FVIII) was then added to initiate the coagulation cascade. The time between the addition of calcium and the clot formation (PT/ a-PTT) is measured, reflecting the amount of FVIII in the sample that was able to correct the clotting time. The analyzer measures the PT/a-PTT by tracking changes in light transmission, with the time required to reach the threshold signal indicating the PT/a-PTT and, consequently, FVIII and FV activity. **(Figure 10. B)**

3.1.3.3. Measurement of vWF Activity

To measure vWF activity, a latex particle-based immunoturbidimetric assay provided by Siemens Healthineers (INNOVANCE® VWF Ac assay kit) was used. This assay operates on the principle of mimicking the binding of vWF to glycoprotein Ib (GPIb) on platelets. In this method, latex particles are coated with anti-GPIb antibodies. Recombinant GPIb containing gain-of-function mutations G233V and M239V, along with blocking reagents and buffer, were mixed with samples containing vWF. The binding of GPIb to its specific antibody and to vWF leads to agglutination, which is detected by a turbidimeter that measures light scattering through the aggregated particles. The degree of light scattering or reduction in light transmission corresponds to the amount of agglutination, which in turn reflects the activity of vWF **(Figure 10. C).**

3.1.3.4. Measurement of vWF Antigen

The vWF antigen assay is similar in principle to the vWF activity assay. In this assay, latex particles are coated with an antibody directed against vWF. When mixed with specific reagents, a glycine-containing buffer, and test samples containing vWF, the latex particles agglutinate, increasing the turbidity or cloudiness of the sample. This turbidity is measured based on light scattering using a turbidimeter, as in the vWF activity assay.

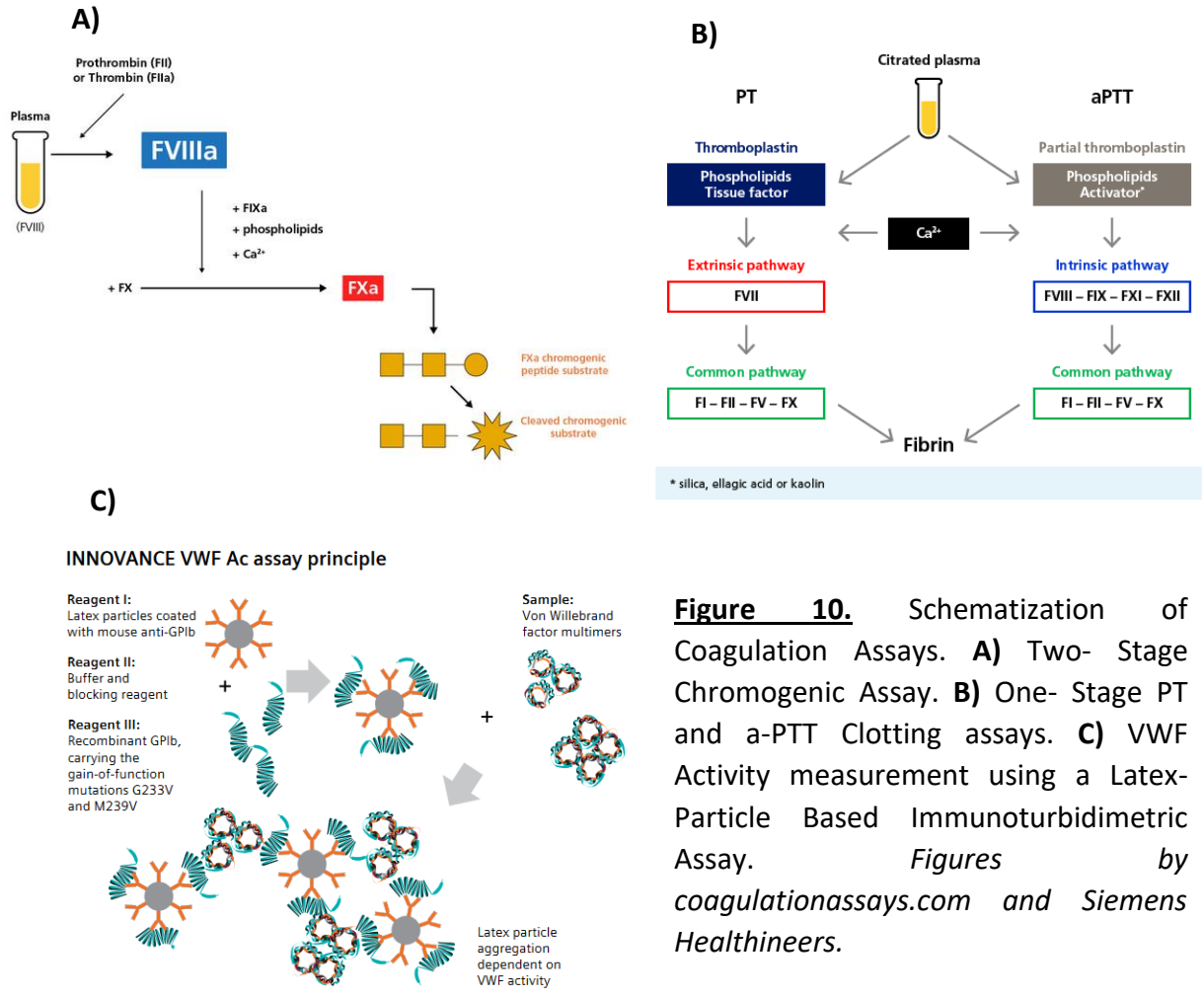

Figure 10. Schematization of Coagulation Assays. **A)** Two- Stage Chromogenic Assay. **B)** One- Stage PT and a-PTT Clotting assays. **C)** VWF Activity measurement using a Latex-Particle Based Immunoturbidimetric Assay. *Figures by coagulationassays.com and Siemens Healthineers.*

3.1.4. Polymerase Chain Reaction (PCR)

Polymerase Chain Reaction (PCR) was performed as a tool for DNA amplification, DNA sequencing, cloning, and gene expression analysis (e.g. iProof PCR for generation of double stranded DNA (megaprimers) upon design of CRISPR/Cas9- vector, Phusion PCR for insertion of generated dsDNA (megaprimers) into the corresponding CRISPR/Cas9- vector, Sequencing PCR performed for vectors and DNA extracted from

cell lysates, and finally PCR reactions associated with the Cleavage Assay upon DNA isolation of CRISPR/Cas9 transfected single cells).

DNA samples were mixed with corresponding amounts of buffers, a specific set of primers, DNA polymerases, dNTPs (Deoxynucleotide Triphosphates), $MgCl_2$, and nuclease-free water. The mixture of corresponding reagents was scaled up in a Master Mix. Positive and negative controls were included to avoid false positive signals, nonspecific DNA products, DNA contamination, and issues related to primer self-annealing, primer dimerization, etc. Samples were pipetted into PCR strips, kept cold on ice, vortexed, and spun down before entering the thermal cyclers. For each purpose, a different PCR thermal cycling program was used, including different denaturation, annealing and elongation thermal phases and cycles.

In the following sections, each PCR experiment will be accompanied by the specific volumes of PCR-mixes material as well as each PCR-program conditions being employed.

3.1.5. Agarose Gel Electrophoresis

Agarose gel was prepared using a weight/volume (w/v) by dissolving 1 g of agarose in 100 ml of 1xTAE buffer (Tris-acetate-EDTA, pH 8.3)), followed by solution heating in the microwave until completely dissolved. Midori Green (5 µL per 100 mL of agarose gel) or Ethidium Bromide (0.5 µg/mL) was then added for DNA visualization. The gel apparatus was prepared by placing the gel casting tray into the casting system, pouring the dissolved agarose into the tray, and by subsequently inserting the desired comb which will be removed following gel solidification. The tray containing the solidified agarose gel was afterwards placed into the gel apparatus filled with 1x TAE buffer. Prior to loading, the samples were mixed with a loading dye (at a 1:5 ratio, e.g., 1 part loading dye to 4 parts sample) containing bromophenol blue and xylene cyanol as tracking dyes, along with a high percentage of glycerol to increase density, allowing the DNA to settle at the bottom of the wells. A DNA ladder was also included to serve as a size marker for the DNA fragments. Samples were left to run for 25-30 min at 150V. Gel was placed on a UV transilluminator system (Bio-Rad Laboratories GmbH) for visualization.

3.1.6. Protein Extraction and Cell lysis

In order to analyze the cellular protein content, cells were cultured at 37°C in a 5% CO_2 humidified incubator. Prior to lysis, old media was discarded and cells were washed with PBS. Depending on the lysis buffer used, different procedures were followed. Protein extraction experiments were carried out using either RIPA (Radioimmunoprecipitation Assay Buffer) or NP-40 **(**Nonylphenol Ethoxylate-40), depending on the requirement of the procedure being perfoemed. Lysis procedure by RIPA buffer: After washing with PBS, RIPA lysis buffer supplemented with a protease inhibitor cocktail (one tablet of protease inhibitor cocktail dissolved in 10 ml of ready RIPA buffer purchased from ROCHE) was added directly to the cells, and the whole cell culture plate was placed on ice for 10 min. Lysis procedure by NP-40**:** After washing with PBS, cells were detached mechanically using Trypsin, centrifuged, as stated in the section (Cultivation of HEK293 mammalian cells) and then washed twice with 1× PBS to remove any residual Trypsin. NP-40 lysis buffer supplemented with a protease inhibitor cocktail (one tablet of protease inhibitor cocktail dissolved in 10 ml of ready NP-40 buffer) was then added to the cell pellet, and the suspension was incubated on ice for 30 minutes with vortexing every 10 minutes to ensure even distribution of the lysis buffer. Following lysis, the cell lysates were centrifuged at 12,000 rpm for 10 minutes at 4°C, and the supernatant containing the protein extract was carefully collected. Protein extracts were stored at either -20°C for short-term storage or -80°C for long-term storage.

3.1.7. SDS-PAGE (Sodium Dodecyl Sulfate-Polyacrylamide Gel Electrophoresis)

To analyze, identify and visualize proteins of interest, Sodium Dodecyl Sulfate Polyacrylamide Gel Electrophoresis (SDS-PAGE) was employed, followed by protein transfer by Western Blotting. To optimize the best conditions for the samples and accommodate the diverse range of proteins under study, two different SDS-PAGE systems: Bio-Rad and ThermoFisher were used. Each system utilized its own specific gels, buffers, sample loading dyes, and running conditions. Samples, which included recombinant proteins, cell lysates and media containing a mixture of proteins, were diluted using appropriate sample buffers (either 2x or 4x Laemmli buffers, or 2x

Tricine-SDS sample buffer). ß-mercaptoethanol was added to the Laemmli sample/loading buffers at a final concentration of 5% (e.g., 950 µl Laemmli buffer mixed with 50 µl ß-mercaptoethanol). The samples were then heated in a thermal shaker at 95°C for 5 minutes while shaking at 350 rpm for high molecular weight proteins, which were subsequently loaded onto 4–15%, 8–16%, or 7.5% Mini-PROTEAN® TGX™ Precast Protein Gels (10 wells, 50 µl) from Bio-Rad. For low molecular weight proteins, the samples were heated at 85°C for 2 minutes before being loaded onto 16% Novex™ Tricine Mini Protein Gels from ThermoFisher. Following heating, the samples were kept on ice until the SDS-PAGE setup was ready. The gels were placed in the SDS-PAGE cell, which was thoroughly cleaned and rinsed with the appropriate running buffer. The samples were then pipetted into the gel wells, the lid was closed, and electrophoresis was performed at 150 V for 30–40 minutes. **(Table. 2)**

3.1.8. Immunoblotting by Western Blot

Following SDS-PAGE, proteins were transferred to a polyvinylidene fluoride (PVDF) membrane using a wet transfer method for subsequent detection with specific primary and secondary antibodies. At the end of the SDS-PAGE run, the gels were carefully retrieved and placed into a sandwich cassette for blotting. The assembly of the cassette was performed by stacking the components in the following order: sponge → filter paper → membrane → gel → filter paper → sponge. Before assembly, the sponges and filter papers were thoroughly immersed in the appropriate 1x transfer buffer. The PVDF membrane was shortly (30 sec) soaked in methanol, then in the 1x transfer buffer, and finally placed directly above the gel to ensure full coverage. The PVDF membrane was also placed between the gel and the positive electrode in order to ensure proper migration of proteins perpendicularly in the direction gel → PVDF membrane. Once assembled, the cassette was tightly closed and placed into the western blot transfer tank. To maintain low temperatures during transfer, an ice pack was placed in the tank, or alternatively, the entire station was set on ice. The tank was filled with transfer buffer to cover the cassette, and the transfer was carried out for 1 hour at 250 mA. After the transfer, the PVDF membrane was retrieved and blocked overnight with 5% skim milk in TBS-T buffer to prevent non-specific binding. The next

day, the membrane was washed three times for 15 minutes each with the TBS-T buffer. The corresponding primary antibodies were diluted in TBS-T and incubated with the membrane overnight at 4°C. On the following day, unbound primary antibodies were removed by washing the membrane three times for 15 minutes each in TBS-T. Secondary antibodies, diluted to the appropriate concentrations in TBS-T, were then incubated with the membrane for 1 hour at room temperature with gentle shaking. After this, the membranes were washed again three times for 15 minutes each and developed using a horseradish peroxidase substrate to visualize the proteins.

Table 2. Different conditions of SDS-PAGE and Western Blot Procedures. Details of corresponding gels, material, running and transfer conditions are listed in the table below.

SDS-PAGE Gel	Protein (MW)	Heating conditions	Running conditions	Transfer Conditions	Buffers
7.5% Mini-PROTEAN® TGX™ Precast Protein Gels (BIORAD)	>200 kDa	95°C 5 min Running buffer: 1x Tris/Glycine/SDS	30-40 min 150 V	1 H 250 mA	2x/4x Laemmli Sample Buffer + ßME
4-15% / 8-16% Mini-PROTEAN® TGX™ Precast Protein Gels (BIORAD)	25- 200 kDa	95°C 5 min Running buffer: 1x Tris/Glycine/SDS	30-40 min 150 V	1 H 250 mA	2x/4x Laemmli Sample Buffer + ßME
16% Novex™ Tricine Mini Protein Gels (ThermoFisher)	<25 kDa	85°C 2 min Running Buffer: 1X Novex™ Tricine SDS Running Buffer	40 min 220 V	1 H 250 mA	2x Novex™ Tricine SDS Sample Buffer

3.1.9. Immunofluorescence Staining (IF)

3.1.9.1. Cell Preparation and Fixation

Immunofluorescence Staining procedures were performed on 4% paraformaldehyde (PFA) fixed HEK293 cells (WT and modified cell lines) using gelatin pre-coated 18 mm round coverslips in 12 wells plates. 0.1% Gelatin from porcine skin was prepared based on w/v solution preparation (e.g., 0.1 g in 100ml ddH_2O) then autoclaved following complete dissolving of the gelatin in water. In order for the gelatin to be completely dissolved, little heating was applied while shaking (30°C to 40°C). Round coverslips were placed into 12 wells cell culture plates and coated by pipetting 1 ml of autoclaved 0.1% gelatin solution. Plates were then sealed with a parafilm and left at 4°C overnight. On the next day, gelatin was discarded and plates were left to dry in the airflow of the hood. Cells were then seeded (250-300 x 10^3 /well) and left to grow until reaching 70-80% confluence at 37°C in a humidified CO_2 incubator. Once the cells have reached the desired confluence, media were discarded and cells were washed with 500 µl of 1x PBS. PBS was then discarded and 500 µl of 4% self-made PFA was added to cells and left to incubate at room temperature for 5-10 min. PFA was subsequently discarded and cells were re-washed with 1x PBS and kept in 1x PBS at 4°C sealed with parafilm at 4°C until further use for immunofluorescence staining. *(**Note:** Fixation was done using methanol at -20°C for 15 min when needed).*

3.1.9.2. Immunofluorescence Staining

Fixed cells were transferred to a new 12-well plate filled with 1x PBS and then blocked using 1 mL of a 1% BSA blocking solution containing glycine for 30 minutes at room temperature. Meanwhile, primary antibodies were diluted to previously optimized concentrations in a 1% BSA antibody solution containing Triton. After blocking, the blocking solution was discarded, and 500 µL of the prepared antibody solution with the desired antibody (or combination of antibodies) was pipetted onto the cells. The cells and antibodies were incubated at 4°C overnight. The following day, the primary antibodies were washed away, and the cells were blocked again for 30 minutes with 1% BSA. Subsequently, the cells were incubated with prepared secondary fluorescent

conjugated antibodies and left to incubate in the dark at room temperature. After incubation, the secondary antibodies were washed away, and the cells were mounted on rectangular slides with a DNA stain-containing mounting medium, ProLong™ mounting medium with NucBlue™.

Note: During the immunofluorescence staining procedures, combinations of primary and secondary antibodies targeting multiple proteins were prepared and used to allow multiplexing and co-localization analysis. (Details of buffer compositions and antibodies used can be found the Materials section).

3.1.9.3. Fluorescence Microscopy Imaging and Co-localization Analysis

Stained cells were visualized using the ApoTome.2 system from Carl Zeiss. Multiple channel images (EGFP, DsRed, Cy5, DAPI, etc.) of the cells were captured using the 40x oil objective. For each condition, three to four images were acquired, and a set of 10-15 cells per image were selected and marked for further co-localization and correlation analysis. Following imaging, the objective's lens was cleaned with special tissues and cover slips were wiped with Ethanol. Each cell was analyzed using Zen Blue 2.6 Pro software, which automatically sets a threshold according to the Costes method. Specific channels intended for co-localization were chosen, and the software calculated various parameters, including signal intensity, Mander's Coefficients, and Pearson's Correlation Coefficient (PCC), among others. For this study, Pearson's Correlation Coefficient (PCC) was considered as it serves well the objectives of this procedure. PCC assesses the degree of co-localization between two signals, providing a value from -1 to 1: a PCC of -1 indicates a high negative correlation between signals, 0 indicates no correlation, and 1 indicates the highest positive correlation between the two signals. PCC values from different immunofluorescence staining procedures were collected, and averages as well as statistical analyses were performed to further evaluate the data sets.

3.2. Knockdown by small interfering RNA Technology (siRNA)

In order to assess short-term effects of specific genes silencing (knock-down) on FVIII secretion, small interfering RNAs (siRNAs) targeting Calnexin, Calreticulin, LMAN1,

MCFD2, and GABARAP were transfected into HEK293 cells stably expressing Factor VIII (HEK28) using lipofection, following the transfection protocol detailed in the "Transfection by Lipofection" section. The siRNAs were purchased from Qiagen, each provided as a stock amount of 1 nmol. To prepare the working stock solutions, each siRNA was re-suspended in sterile, RNase-free water. The siRNA transfection was performed in 24-well plates, with cells seeded at a density of 150-200 × 10^3 cells per well. siRNAs were diluted in Opti-MEM to the desired concentrations before

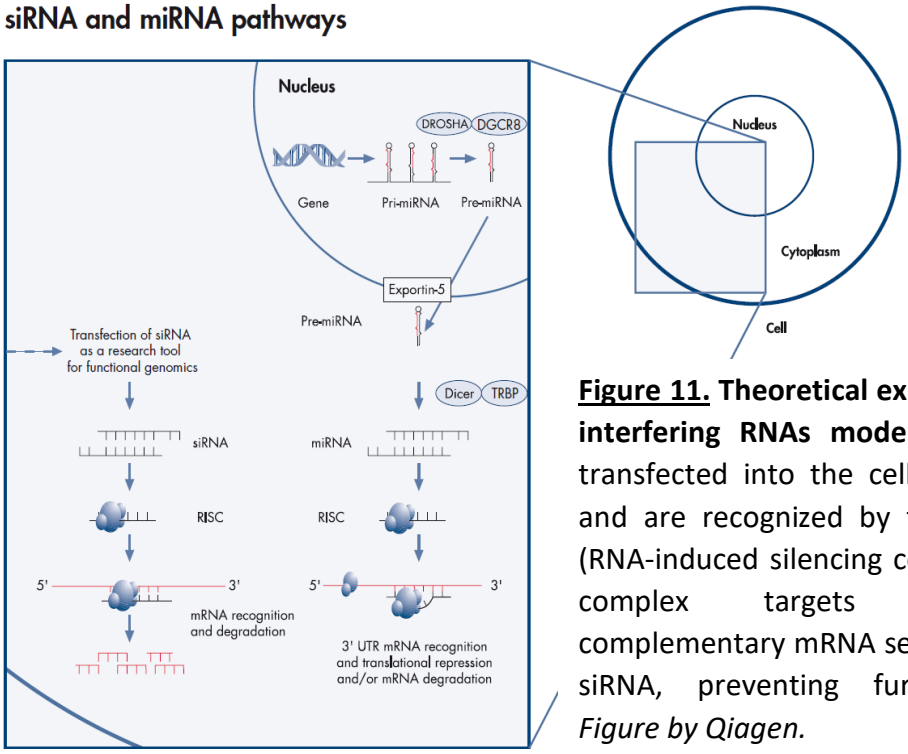

Figure 11. Theoretical explanation of small interfering RNAs mode of action. Once transfected into the cells, siRNAs unwind and are recognized by the RISC complex (RNA-induced silencing complex). The RISC complex targets and cleaves complementary mRNA sequences to bound siRNA, preventing further translation. *Figure by Qiagen.*

transfection. A range of siRNA concentrations (5nM, 20nM, and 50 nM) was initially tested, with 5 nM ultimately chosen for subsequent experiments based on preliminary results. For transfection, siRNA-Opti-MEM mixtures were prepared in a 1:1 ratio with Lipofectamine, then added to the cells. After transfection, cells were incubated for 72 hours. Media samples were collected at 48 and 72 hours post-transfection to assess FVIII activity using a two-stage chromogenic assay. A scrambled siRNA with no homology to any mammalian gene served as a negative control, along with mock-transfected and un- transfected cells as additional controls. All experiments were conducted in triplicate to minimize measurement biases, with appropriate master mixes prepared for multiple reactions to ensure consistency. **(Figure 11)**

3.3. Chemical Cellular Treatments

Cell clones including HEK28^{WT}, CANX^{KO}, CALR^{KO}, LMAN1^{KO}, and GABARAP^{KO} were subjected to various conditions involving treatments with specific drugs and chemicals like Brefeldin A (BFA), Chloroquine (CQ) and Rab7 inhibitor CID 1067700, in addition to stressful metabolic conditions like glucose starvation. Full establishment procedures were carried out in HEK28^{WT}. Upon confirmation of optimal treatment (s) conditions, the procedures were further applied to the cell KO-clones. FVIII activity measurements were assessed using a two-stage chromogenic assay, and cells were in parallel fixed with 4% paraformaldehyde for IF- staining experiments. Treatment details are presented in **Table 3).**

Table 3. Experimental Establishment Workflow of the Four Employed Chemical Treatments. (Brefeldin A, Glucose Starvation, Chloroquine, and rab7.inhibition CID 1067700).

Treatment	Brefeldin A (BFA)	Glucose Starvation	Chloroquine (CQ)	Rab7 inhibition (CID 1067700)
Reconstitution and Stock concentration	**Stock** : 10 mg/ml in DMSO	All media were supplemented with hiFBS and antibiotics	**Stock:** freshly reconstituted prior to each experiment at 50 mM in ddH_2O	**Stock:** 10 mg/ml in DMSO
Treatment Concentration	**Establishment:** 0.05-10 µg/ml **Final:** 0.05 µg/ml	**Establishment**: - reduced serum - glucose deprivation - amino acid deprivation - glucose & amino acid deprivation **Final:** - Glucose deprivation	**Establishment:** 2.5- 15 µM **Final:** 10 µM	**Establishment:** 10- 40 µM **Final:** 40 µM
Treatment Duration	**Establishment**: 30 min- 24 hours **Final**: 20 hours	24 hours	24-36 hours	24 hours
Storage	-20°C	4°C	Lyophilized powder at -20°C	-20°C
Treatment Verification	**IF Staining** Cis- and Trans-Golgi markers GM130 and TGN46	**Western Blot** Tracking changes in LC3B-band **IF Staining** Tracking changes in LAMPI vesicles	**Western Blot** Tracking changes in LC3B banc **IF Staining** Tracking LC3B accumulation	**Western Blot** Tracking changes in LAMPI band **IF Staining** Tracking changes in Rab7 protein pattern
Purpose	To block vesicular trafficking between the endoplasmic reticulum (ER) and the Golgi apparatus	To influence cellular metabolism, energy levels, and activate the autophagy machinery	To disrupt the autophagy machinery, particularly the fusion of autophagosomes with lysosomal compartments, as well as endosomal organelles and Golgi associated networks	CID 1067700 is a competitive inhibitor, which binds Rab7 and disturbs its binding to other proteins reducing the fusion of the late endosomes to the lysosomes

3.4. Mitochondria Staining

3.4.1. Cell Preparation and Mito-Staining (Experimental Procedure)

Cells were seeded onto 0.1% gelatine coated cover slips in 12 well plates in complete DMEM, and left to grow for 48 hours at 37°C in a CO_2 humidified incubator. To stain mitochondria, a chemical dye was chosen, the MitoTracker® Mitochondrion-Selective Probes, specifically MitoTracker® Red CMXRos (Invitrogen, #M7512). MitoTracker Stock solutions were prepared by diluting the lyophilized powder in dimethylsulfoxide (DMSO) to a final concentration of 1 mM and kept at -20°C in the dark until further use. MitoTracker stock solution was further diluted in media without addition of sera or antibiotics according to the manufacturer's recommendations, to a concentration of 100 nM. Old media were removed and replaced by the MitoTracker containing Media, and left to incubate at 37°C in a CO_2 humidified incubator for 30-45 min. Media were finally removed, cells were washed with 1xDPBS and fixed with 4% Paraformaldehyde. The cover slips with stained cells were further mounted with ProLong™ Glass Antifade Mountant with NucBlue™ Stain and left to dry completely prior to imaging. Images were then taken using the ApoTome.2 from Zeiss.

3.4.2. Image Analysis (CellProfiler 4.2.8)

For the image analysis, used CellProfiler 4.2.8 was used. This analysis involved constructing a pipeline in which several modules were integrated, each responsible for processing cells and targets of interest. The modules used were designed to first identify the nuclei, then propagate to the cell borders and outline the cells. Based on this, the cytoplasm region was identified, which subsequently contained the mitochondria. The Cytoplasm and Mitochondria objects were then related as Parent (Cytoplasm) - Children (Mitochondria). Further modules were added to the pipeline, including commands for intensity, count, and area measurements of objects. The data extracted included the count of mitochondria based on the segmentation of individual mitochondria after adjusting parameters for object diameter and intensity

thresholding. The lower intensity threshold for mitochondria detection was adjusted to 0.1, 0.15, 0.2, 0.25, and 0.3, and measurements were assessed accordingly.

The occupied area of mitochondria was divided by the occupied area of the cytoplasm to further quantify mitochondria occupation per cell.

$$\text{Area of Mitochondria (per image)} = \frac{\text{Area of All Mitochondria objects within Cytoplasm Objects (per image)}}{\text{Area of all Cytoplasm objects (per image)}}$$

Mean intensities of mitochondria objects were calculated by dividing the integrated intensities or total intensities of mitochondria per cell by the area of the cytoplasm they occupy.

$$\text{Mean Intensity} = \frac{\text{Total Intensity of Mitochondria in one Cytoplasm}}{\text{Area of the Cytoplasm}}$$

3.5. Protein Interaction Assays

3.5.1. Bio-layer Interferometry Assay (BLItz)

Bio-layer Interferometry is a technique used to investigate interactions between biomolecules based on a "Dip and Read Format" **(Figure 12).** The principle of this technique is based on the optical monitoring, in real-time, of the shift in wavelength between two white light interference patterns. This shift is usually caused by changes in the amount of biomolecules binding, reflecting a difference in thickness or in the distance between the studied surfaces (Biosensors-Air). These changes in light

reflection patterns are translated into kinetic studies of association and dissociation curves, which are used for further assessment of binding affinity.

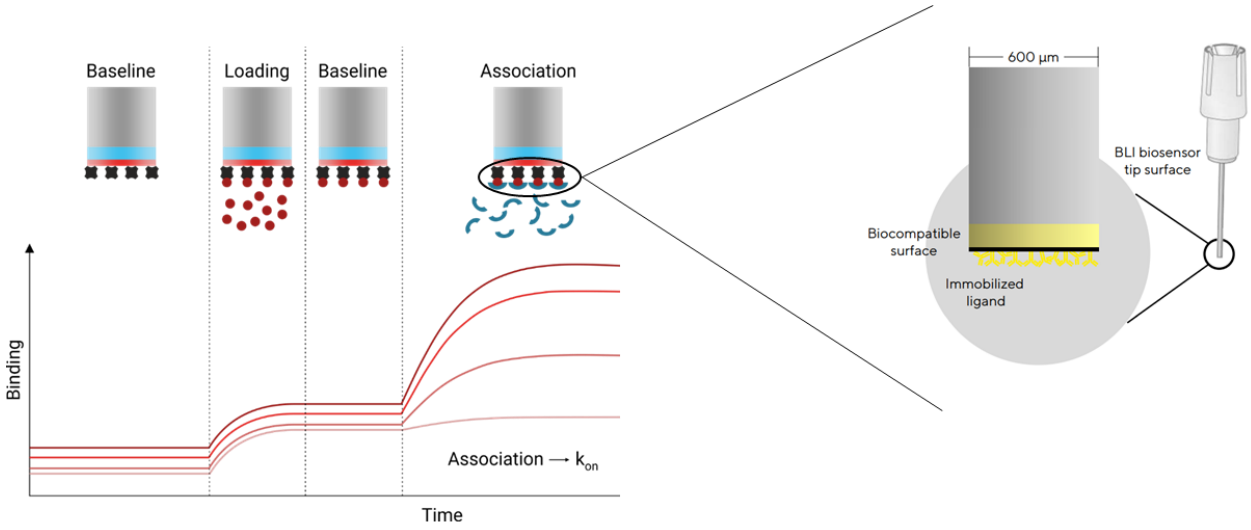

Figure 12. Experimental schematization of the Bio-layer Interferometry Assay (BLItz), along with the translation of the outcomes in the form of graphical curves showing baselines, loading (immobilization), and association curves. On the right a magnified schematization of the Biosensor shape and characteristics. Edited Figure from *https://2bind.com/technologies/bli/.*

3.5.1.1. Experimental Setup

The experimental setup consisted of three recombinant proteins: GABARAP, Full-length FVIII (octocog alfa: Kovaltry® 1000 I.E.) and B-deleted-domain FVIII (moroctocog alfa: Refacto® 1000 I.E.).

i. Immobilization of GABARAP on the Biosensor

The recombinant GABARAP protein was initially purchased from Cusabio as a C-terminal His-tagged GABARAP protein at a stock concentration of 1 mg/ml in the corresponding buffer. To ensure proper binding of the protein on the anti-His coated biosensors, the protein was analyzed using SDS-PAGE followed by Western blotting. Both the His-tag and GABARAP were detected, along with appropriate negative controls, to verify the protein. First, the anti-His biosensors were hydrated for at least 10 minutes to dissolve the sugar biosensor coat. As a first step baseline was generated to deduct any buffer background. Next, using a binding buffer, the recombinant

GABARAP protein was diluted to varying concentrations (0.5 µM - 2 µM) and loaded onto the biosensors for 2 minutes. After determining the appropriate concentration, taking into consideration the potential oversaturation of the biosensor, a concentration of 1 µM recombinant GABARAP was used for the subsequent procedures. Following the successful loading of GABARAP on the biosensor tip, a second baseline was generated. The ligand – Kovaltry and Refacto – were diluted in five different concentrations (0.065 µM – 1 µM), and the GABARAP-loaded biosensor tip was dipped into these solutions to allow for FVIII product association. Subsequently, the biosensor tip was dipped into the buffer to estimate the amount of ligand dissociation. The experimental setup included a blank buffer as a negative control – which was used as a reference for further kinetic analysis-, GABARAP alone, and FVIII products as additional negative controls.

ii. Immobilization of FVIII on Streptavidin Biosensors

A reciprocal BLItz protocol was conducted to evaluate the binding of immobilized FVIII products to the soluble recombinant GABARAP protein. In this reverse scenario, both Kovaltry and Refacto were pre-biotinylation using the EZ-Link™ Sulfo-NHS-LC-Biotin, No-Weigh™ Format kit from ThermoFisher. The biotinylation protocol was executed according to the manufacturer's instructions with slight optimizations to fit the proteins of interest. To first discard all potential interfering buffer ingredients and FVIII products' supplementary salts, amino acids…etc, the buffers in which both FVIII concentrates were (H_2O), were first exchanged with PBS using Zeba™ Spin Desalting Columns with a 7K MWCO (Molecular Weight Cut Off). This was done by washing the columns three times with PBS, each followed by centrifugation at 1500 x g for 1 min. The FVIII solutions were then loaded onto the Zeba™ spin columns and centrifuged for 2 minutes at 1500 x g. The concentration of the recovered FVIII protein was measured using a NanoDrop Spectrophotometer. Molar concentrations of both Kovaltry and Refacto were calculated, accordingly Biotin was subsequently added at a molar ratio of 50:1 (Biotin: FVIII), and the FVIII-biotin mixture was incubated at room temperature for 30 minutes in the dark, with mixing after 15 minutes. Excess unbound biotin was removed by a final repeated desalting step, and final FVIII concentration was

reassessed to ensure accurate calculations for the following BLItz assay. The biotinylated FVIII concentrates, Kovaltry and Refacto, were then immobilized on the Streptavidin Biosensors after a 10 min hydration step, following the previous protocol. Each concentrate was loaded taking into account the high molecular weight of full-length FVIII and the differences in protein sizes between full-length and B-domain-deleted FVIII. Five concentrations of recombinant GABARAP protein were prepared and diluted in binding buffer (1 µM, 0.5 µM, 0.25 µM, 0.125 µM, and 0.062 µM) for sequential binding during the association phase. The same negative controls were as well employed to deduct un-specificities and buffer background.

3.5.1.2. Calculations and Analysis

At the end of each run, binding affinities were determined by calculating the ratio of the dissociation rate (k_{off}) to the association rate (k_{on}), represented as $KD = k_{off}/k_{on}$ (or $KD = k_{dissociation}/k_{association}$). Data were displayed as curves showing baselines, association, and dissociation curves. Binding affinities (KDs) were calculated, and all curves were normalized using BLItz Pro™ software (SARTORIOUS; version 1.2.1.5) from FortéBio, to the blank buffer run.

3.5.2. Immunoprecipitation and co-Immunoprecipitation

To rapidly capture protein-protein interactions in cell lysates, an immunoprecipitation protocol based on small-scale affinity of antigen purification after immobilization of respective antibody on a solid support. For this, the Capturem™ IP and co-IP kit purchased from TAKARA was utilized. The TAKARA kit uses Protein A columns which have a high affinity to capture the Fc region of IgG antibodies, a high sample volume (up to 850 µl) and a small elution volume (20 µl). Cells were first lysed using RIPA or NP-40 lysis buffers and then incubated with the desired amount of antibody (1-2 µg, optimized for each protein) at 4°C for 1 hour up to overnight, or at room temperature for 20 minutes. According to the manufacturer's instructions, cell extracts (300-400 µl) were then loaded onto the previously equilibrated columns (100 µl of equilibration kit buffer, centrifuged at 1,000 g for 1 minute). The flow-through was either discarded or kept for further downstream analysis. The columns were then washed to remove

unbound and non-specific proteins using the kit wash buffer (100 µl of wash kit buffer, centrifuged at 1,000 g for 1 minute), and the wash flow-through was also discarded or kept for further downstream analysis. The washing step was sometimes repeated twice for a cleaner background. Finally, the columns were placed into pre-coated Eppendorf tubes containing a self-made neutralization buffer (1 M Tris, pH 8). The volume of neutralization buffer constituted 1/10th of the final volume of the added elution buffer. Twenty to fifty µl of elution buffer were then added to the columns to disrupt the protein A-antibody interaction, columns were subsequently centrifuged at 1000 g for 1 min and the eluted sample was either directly loaded for SDS-PAGE and Western blot analysis or briefly stored at -20°C for further analysis in the upcoming days.

3.6. Generation of CRISPR/Cas9 Knockout Cell Lines

Note: In this thesis, CRISPR/Cas9 double knockout (DKO) cell lines were generated in HEK28^{WT}, stably expressing FVIII on the basis of the previously generated single- KO cell lines. These cell lines included double-KOs of **CANX/LMAN1**, **CANX/GABARAPL1, and CANX/GABARAP** along with **CANX/CALR, CALR/GABARAP** and **LMAN1/MCFD2;** the latter three **DKOs** were previously generated but as well integrated and further analyzed in this thesis. The double knockout of **CANX/GABARAPL1** was excluded from the further analysis of this study**.** In the following section, procedures will be generally described to simplify comprehension. Additional details are provided in table formats (vector and primer information are provided in **Chapter 2: Material**). The same procedure was applied to generate all CRISPR/Cas9-knockouts.

3.6.1. Design of single-stranded DNA (Design of gRNAs)

All gene specific guide RNAs were earlier designed using the online tool provided by the Zhang lab (http://crispr.mit.edu/) which is now re-directed to other online resources such as Benchling or other CRISPR/Cas9 designing tools. Briefly, Target DNA sequences were provided to the tool in a FASTA format. Specific criteria such as the type of CRISPR system, the Cas9 protein, genome reference, and the type of the PAM (Protospacer Adjacent Motif) sequence (in this case NGG) was submitted to the

system and the analysis was run. Results were displayed as potential candidates for guide RNAs showing scores on efficiency and specificity of each candidate, as well as potential off-targets. Both top and bottom (complementary) single strands were designed and purchased.

3.6.2. Generation of double-stranded DNA (Megaprimers)

3.6.2.1. Annealing of double – stranded DNA

To anneal the complementary single stranded designed oligonucleotides into double-stranded oligonucleotides, a PCR was performed using the reagents of the iProof™High-Fidelity PCR Kit purchased from ThermoFisher, according to the following mixture for one reaction. Samples were then loaded on 1% agarose gel electrophoresis along with 100 bps ladder.

Component	**Amount/Volume**
H_2O	35 µl
iProof 5X HF/GC Buffer (7.5 mM $MgCl_2$)	5 µl
dNTPs mix (2.5 mM)	1 µl
Forward strand oligo. 100 pmol	1 µl
Reverse strand oligo. 100 pmol	1 µl
iProof polymerase	0.5 µl

Cycler Program:

	Step	**Temperature °C**	**Time**
	1	98	30 s
30 cycles	**2**	98	10 s
	3	60	30 s
	4	72	30 s
	5	72	10 min
	6	4	Forever

3.6.2.2. Gel extraction and Concentration measurement

After documentation, PCR products were extracted from the agarose gel and purified using the QIAquick Gel Extraction Kit following the manufacturer's instructions. First, the desired PCR fragments were carefully excised from the gel using a clean, sharp scalpel and then placed in microcentrifuge tubes for weighing. Three volumes of Buffer QG were added to the gel slices (using 1 volume of gel as the reference). The tubes were then incubated at 50°C for 10 minutes or until the gel slices were completely dissolved. Once the gel was fully dissolved, one volume of isopropanol was added to each sample. The samples were then applied to QIAquick spin columns placed in the provided 2 ml collection tubes. After centrifugation for one minute, the flow-through was discarded, and the columns were placed back into the same collection tubes. Next, 500 µl of Buffer QG was added to the columns, and the samples were centrifuged again for one minute. The flow-through was discarded, and the columns were returned to the same collection tubes. Subsequently, 750 µl of Buffer PE was added to the columns, followed by centrifugation for one minute. An additional centrifugation for one minute was performed to remove any residual wash buffer. The columns were then transferred to new, clean collection tubes, where 30 µl of water was added directly to the center of each column to elute the DNA. The tubes were centrifuged for one minute to collect the eluted product. Finally, the concentration of the megaprimers was measured using a NanoDrop spectrophotometer.

3.6.2.3. Cloning (Insertion) of Megaprimers into corresponding Vectors

The generated megaprimers (or annealed dsOligos) were fused into the corresponding vector according to the following PCR reaction mixture and conditions, using the Phusion High-Fidelity PCR Kit purchased from ThermoFisher.

Component	Volume / Amount
H_2O	11.5 µl
5x HF –Buffer	4 µl
dNTPs (2.5 mM)	1.6 µl
Phusion Polymerase	0.5 µl
Vector	1.5 µl (10 ng/ µl)
Megaprimer	70 ng

Cycler Program:

	Step	Temperature °C	Time
	1	98	2 min 30 s
33 cycles	**2**	98	30 s
	3	60	1 min
	4	72	7 min
	5	72	7 min
	6	10	Hold

3.6.3. Transformation into competent E.coli

To isolate positive plasmids containing the correct insertion, the previously constructed vectors were transformed into E. coli Top10 chemically competent cells. Prior to transformation, 1 µl of DpnI was added to each reaction mixture and incubated at 37°C for 1 hour in a thermal cycler. For each reaction, one 50 µl vial of OneShot® Top10 competent cells was used. The vials were placed on ice until fully thawed. To each vial, 5 µl of the ligation reaction containing the inserted megaprimers (annealed ssOligos) was added, and the contents were gently mixed by tapping or swirling (no pipetting). The vials were then incubated on ice for 30 min, followed by a heat shock at 42°C for exactly 30 seconds. Immediately after a heat shock, 250 µl of pre-warmed S.O.C. medium (Super Optimal broth with Catabolite repression) was

added to each vial. The vials were then shaken at 37°C for 1 hour at 225 rpm. After incubation, the entire volume from each vial was spread onto separate labeled LB agar plates containing the appropriate antibiotic (ampicillin). Once the plates were dry, they were inverted and incubated overnight at 37°C. The following day, colonies were picked from the plates using a tip, and an overnight culture was set up using 5 mL of LB medium with 5 µl of ampicillin (final concentration of 50 µg/ml) in a shaker at 37°C.

3.6.4. Plasmid Isolation and Purification

Plasmids were isolated from overnight cultures using the GeneJET Plasmid Miniprep or Midiprep Kits from ThermoFisher. Both kits describe almost the same protocol however employing different samples' volume and resulting in different final yields. To simplify, I will describe the protocol of the Miniprep for plasmid purification and isolation. All steps were performed at room temperature, with centrifugations in a tabletop microcentrifuge at speeds over 12,000 g. To start, 800 µl of the bacterial culture was reserved for stock at 4°C. The remaining cells were harvested by centrifugation, and the pellet was resuspended in 250 µl of resuspension solution in a microcentrifuge tube. Next, 250 µl of lysis solution was added, and the tube was inverted until the solution became clear. Then, 350 µl of neutralization solution was added, causing a white precipitate to form. The mixture was centrifuged for 5 min to pellet the cell debris and chromosomal DNA. The supernatant was transferred to a GeneJET spin column and centrifuged; the flow-through was discarded. The column was washed twice with 500 µl of wash solution, each followed by centrifugation and removal of the flow-through. A final centrifugation step was performed to eliminate any residual wash buffer. The column was then placed in a fresh 1.5 ml collection tube, and 50 µl of elution buffer was added directly to the center of the column membrane to elute the plasmid DNA. After a final centrifugation, the column was discarded, and the plasmid DNA was stored at -20°C. To verify successful plasmid isolation, 0.5 µl of the samples were mixed with 2 µl of loading dye (1:4 ratio) and 5 µl of water, and loaded onto an agarose gel. Electrophoresis was conducted under standard conditions (150 V, 300 mA, 25 min), alongside a 1 kb DNA ladder.

3.6.5. Plasmid Sequence Verification

3.6.5.1. Plasmid Sequencing

Sequencing PCR

Component	Amount
H_2O	6.5 µl
Ready mix	1.5 µl
5x Sequencing Buffer	1.5 µl
3.2 pmol U6 primer	0.5 µl
DNA	0.5 µl

Cycler Program:

	Step	Temperature °C	Time
	1	96	10 min
30 cycles	**2**	96	45 s
	3	58	45 s
	4	70	1 min
	5	70	10 min
	6	4	Hold

3.6.5.2. Post-sequencing PCR Cleanup: Ethanol Precipitation

The next step involved the precipitation and purification of the sequencing amplification reactions. After removing the tubes from the thermocycler, the centrifuge was cooled down to 4°C. 10 µl of chromatography-grade water and 2 µl of 3 M sodium acetate were added to each vessel. The strips were then sealed, vortexed briefly, and centrifuged for a short time. Following this, 50 µl of 100% ethanol was added to each mixture. The PCR strips were centrifuged at 4°C for 45 minutes at 4000 rpm. Once centrifugation was complete, the strips were inverted over a waste container/sink to discard the supernatant. Next, 200 µl of 70% ethanol was added to

each vessel, and the strips were centrifuged again for 10 minutes at 4°C and 4000 rpm. After this second centrifugation, the strips were inverted over the waste container/sink once more to remove any remaining liquid. A final centrifugation was performed with the strips inverted in the centrifuge for 1 minute at 10°C and 1000 rpm to ensure all residual liquid was removed. The strips were then sealed with the appropriate lids and stored in the freezer until they were ready to be loaded into the sequencer.

Following the sequencing and sequence analysis, the correct plasmid was selected, and the corresponding E. coli stock solution was used to scale up the transformed plasmid yield. For this, 20 µl of the transformed E. coli stock was mixed with 50 ml of LB medium and 50 µl of ampicillin. The mixture was left to shake overnight at 37°C to ensure bacterial growth, and then the plasmid was purified using the Midi-prep kit protocol purchased from ThermoFisher.

3.6.6. Transfection of CRISPR/Cas9 Vectors & Generation of Single Cells

3.6.6.1. Cleavage Assay (T7 endonuclease I Assay)

i. Transfection, Cell Lysis and DNA Extraction

HEK293 cells were transfected with 1-2 µg prepared CRISPR/Cas9 vectors. 48 hours following transfection, cell were lysed and analyzed. After 48 hours of transfection, both transfected and non-transfected cells (serving as controls) were collected for DNA testing according to the procedure described below. First, the culture medium was removed, and the cells were washed with 1x PBS. Then, 500 µl of trypsin was added to each well to detach the cells, followed by a 2-minute incubation. Next, 1.5 ml of DMEM was added to neutralize the trypsin, and the cell suspension was transferred into a Falcon tube. The tubes were centrifuged, the supernatant was discarded, and 3 ml of fresh medium was added to re-suspend the cell pellet. From this 3 ml suspension, 1.5 ml was transferred to an Eppendorf tube, while the remaining 1.5 ml was added to 8.5 ml of DMEM for continued culture (to preserve the cells in case the cleavage assay was positive). The Eppendorf tube was then centrifuged for 2 minutes at 1200 rpm, and the supernatant was removed. For DNA testing, 50 µl of cell

lysis buffer was mixed with 2 µl of protein degrader from the GeneArt® Genomic Cleavage Detection Kit (A24372). The cells were re-suspended in 50 µl of this mixture and transferred to a PCR strip. The entire sample was then lysed using the following program:

Cycler Program:

Step	Temperature °C	Time
1	68	15 min
2	95	10 min
3	4	Hold

ii. DNA Amplification

Component	Sample (µl)	Control (µl)
Cell lysate	2	-
10 µM F/R primer mix	1	-
Control template and Primers	-	1
Amplitaq Gold® 360 MM	25	25
H_2O	22	24

PCR Programm:

Step	Temperature °C	Time	
1	95	10 min	
2	95	30 s	**40 cycles**
3	60	30 s	
4	72	30 s	
5	72	10 min	
6	4	Hold	

To verify PCR success , 3 µl of PCR product was loaded with 10 µl water and combined with 2 µL loading dye (1:40) on a 1% gel along with the 100 bp ladder.

iii. Re-annealing

Component	Amount
H_2O	6 µl
PCR product	2 µl
Detection Buffer (10X)	1 µl

Cycler Program

Step	Temperature °C	Time
1	95	5 min
2	95 - 85	-2 oC / s
3	85 - 25	-0.1 oC/s
4	4	Hold

iv. Enzyme detection

In this step, hetero-duplex DNA containing the introduced mutations (insertions, deletions, or mismatches) is cleaved by the detection enzyme (T7 endonuclease I). To each sample, 1 µl of the detection enzyme was added, mixed thoroughly, and incubated at 37°C for 1 hour. After incubation, 10 µl of the sample were mixed with 4 µl of 6X DNA loading dye and loaded onto a 2% agarose gel. The gel was run at 100 V for 40 minutes.

3.6.6.2. Generation of CRISPR/Cas9 –transfected Single Cells

In all CRISPR/Cas9 transfection procedures, whether targeting single or double genes for knockout (KO), the population of transfected cells was allowed to grow while the cleavage assay was performed. After the assay, cells were collected and centrifuged following the initial steps of cell passaging/splitting described in Section X. The cell pellet was re-suspended in 5 ml of fresh complete DMEM, and 50 µl of this suspension was further diluted into 50 ml of fresh complete DMEM. Cells from this dilution were then plated into 96-well plates with the goal of achieving 1 cell per well, from which a homogeneous cell population can grow. If the desired concentration of one cell per

well was not achieved, further dilutions are performed. Once the desired dilution was achieved, cells were plated across 8-10 96-well plates, allowed to grow, and monitored on the second day to ensure that single cells were present in each well. Colonies emerging from single cells were then picked and transferred into new 96-well plates for further analysis.

i. DNA Isolation

Using a specific buffer (miSeq Buffer) supplemented with proteinase K, cells were lysed (90 µl Lysis Buffer) and the lysates were transferred into PCR strips. Lysis was performed according to the following conditions.

PCR Program:

Step	Temperature °C	Time
1	65	10 min
2	95	15 min
3	4	Hold

ii. DNA Amplification

Component	Amount (µl)
H_2O	16
BB2 Buffer	2.5
S-solution	2.5
dNTPs (2.5 mM)	2.5
$MgCl_2$ (25 mM)	2.5
Primers (F/R)	1
Hot-Fire Taqpolymerase	0.7
PCR Product	2

Cycler Program: **(View Cleavage Assay)**

Gel agarose Electrophoresis was subsequently carried out to visualize PCR products.

iii. Sequencing

Component	Amount (µl)
H_2O	4
3.2 pmol (F or R) primers	1.2
Sequencing Buffer	1
Ready Mix	1
PCR Product	2

The PCR strips were loaded into the cycler, and sequencing PCR was carried out according to the previously described protocol. The samples were then purified using the same procedure as described earlier.

3.6.6.3. Transferring Positive Clones

After verifying all the picked clones, those with homozygous mutations were selected from the culture for further analysis. The first step involved transferring the clones to a 48-well plate using trypsin, with some clones being removed by scratching to serve as backup cultures. The same procedure was then used to transfer the clones sequentially to 24-well, 12-well, and 6-well plates, eventually culminating in plating onto a 10 cm dish.

The picked clones were ultimately verified through Western blotting (WB) and Immunofluorescence Staining to confirm complete protein knockout. Additionally, FVIII activity was measured and compared to that of the wild type cells.

3.7. Assessment of residual ATP content in living CRISPR/Cas9-KO Generated Cells

To measure residual ATP content within live CRISPR/Cas9-KOs cells, The Luminescent ATP Detection Assay Kit was purchased from abcam and the protocol was applied following manufacturer's instructions. Cells were grown and incubated in a white 96-well plate at a seeding concentration of 30 $x10^3$ cells/well (6 replicates for each clone). For the establishment of the standard curve, ATP standard stock was diluted in

substrate buffer provided by the kit to a final concentration of 100 µM followed by a serial 10-fold dilution until having 6 standards in addition to a blank. Next, 50 µl of the detergent was added to each well to lyse the cells and stabilize the ATP. The plate was then sealed and left to shake for 5 min in an orbital shaker at 600-700 rpm. Afterwards 50 µl substrate was added to each well and also left to shake at 600-700 for 5 min in an orbital shaker. The plate was finally covered and left in the dark for 10 min before entering the microplate reader for further luminescence assessment. ATP concentrations in the cells were calculated using the generated standard curve (luminescence against ATP concentration).

3.8. Transient Genetic Rescue of Stable CRISPR/Cas9- single and Double Kockout Cells

CRISPR/Cas9- KO cell-clones were seeded at a density of 250×10^3 cells per well in 24-well plates (in triplicates) using DMEM without antibiotic supplementation. Cells were cultured until reaching approximately 70% confluence. Transfection was performed using Lipofectamine 2000 with 2 µg of pcDNA3 vectors (diluted in OptiMEM reduced serum) carrying genes encoding CANX, CALR, LMAN1, MCFD2, and GABARAP. For single knockouts, cells were transfected with the corresponding individual gene, while double knockouts were generated by transfecting cells with vectors carrying each knockout separately, followed by co-transfection with both vectors to rescue the phenotype. The culture medium was switched to complete DMEM on the following day, and 48 hours later, supernatants were collected for FVIII quantification using a two-stage chromogenic assay. For the detailed experimental setup, refer to **Table 1**.

4. Chapter 4: Results

4.1. Stable CRISPR/Cas9-KOs & Transient siRNA-based- Knockdowns of Selected Genes showed Consistent Outcomes on FVIII secretion

Besides assessing FVIII activity in the media of the previously generated stable single CRISPR/Cas9-KO cells, a second approach was employed, involving gene silencing mediated by the siRNA (small interfering RNA) technology, which was directed against each of the CANX, CALR, LMAN1, MCFD2, and GABARAP(s) genes. In this strategy the aim was to compare the effects of stable (total) and transient (partial) silencing of the selected genes, thereby observing the short- and long-term effects on FVIII secretion. Interestingly, knockouts of CANX and CALR, two ER chaperones involved in quality control and proper protein folding, as well as in regulating calcium levels in the ER and cytoplasm [31, 32, 44, 78], showed different effects on FVIII secretion. $CANX^{KO}$ led to a reproducible increase in FVIII accumulation in the media, while $CALR^{KO}$ showed the opposite result. Similar to $CANX^{KO}$, deletion of proteins of the Atg8 family ($GABARAPL1^{KO}$, $GABARAPL2^{KO}$, and $ATG7^{KO}$) increased FVIII secretion. However, $GABARAP^{KO}$ aligned with $LMAN1^{KO}$ and $MCFD2^{KO}$, which were similar in response to $CALR^{KO}$, showing lower FVIII secretion levels compared to $HEK28^{WT}$ **(Figure 13. B)**. Moreover, it is noteworthy that FVIII secretion levels were consistently comparable between $GABARAP^{KO}$ and $CALR^{KO}$. Monitoring the results from a different angle following transient transfection with selected gene- silencing siRNAs, demonstrated patterns paralleling those of the stable single CRISPR/Cas9-KOs. Specifically, $CANX\text{-}_{siRNAs}$ and $GABARAPL1\text{-}_{siRNAs}$ increased FVIII activity, while $CALR\text{-}_{siRNAs}$, $GABARAP\text{-}_{siRNAs}$, $LMAN1\text{-}_{siRNAs}$, and $MCFD2\text{-}_{siRNAs}$ reduced FVIII accumulation in the extracellular media. Additionally, a negative control of randomly scrambled siRNA was used and did not show any change in FVIII secretion **(Figure 13. A).**

Both approaches were strongly correlated (r= 0.889, p value = 0.0074; **Figure 13. C**), highlighting first, the reproducible opposite effects of the two ER chaperone knockouts, CANX and CALR, on FVIII secretion; and second, the persistent alignment of $GABARAP^{KO}$ with control knockout clones (CALR, LMAN1, and MCFD2 knockouts), rather than with $GABARAPL1^{KO}$, $GABARAPL2^{KO}$, and $ATG7^{KO}$. These results aligned as

well with earlier work (by earlier team members) which involved transient co-expression of FVIII with transient transfection of siRNA against Calnexin, Calreticulin, LMAN1, MCFD2, GABARAP, and GABARAPL1.

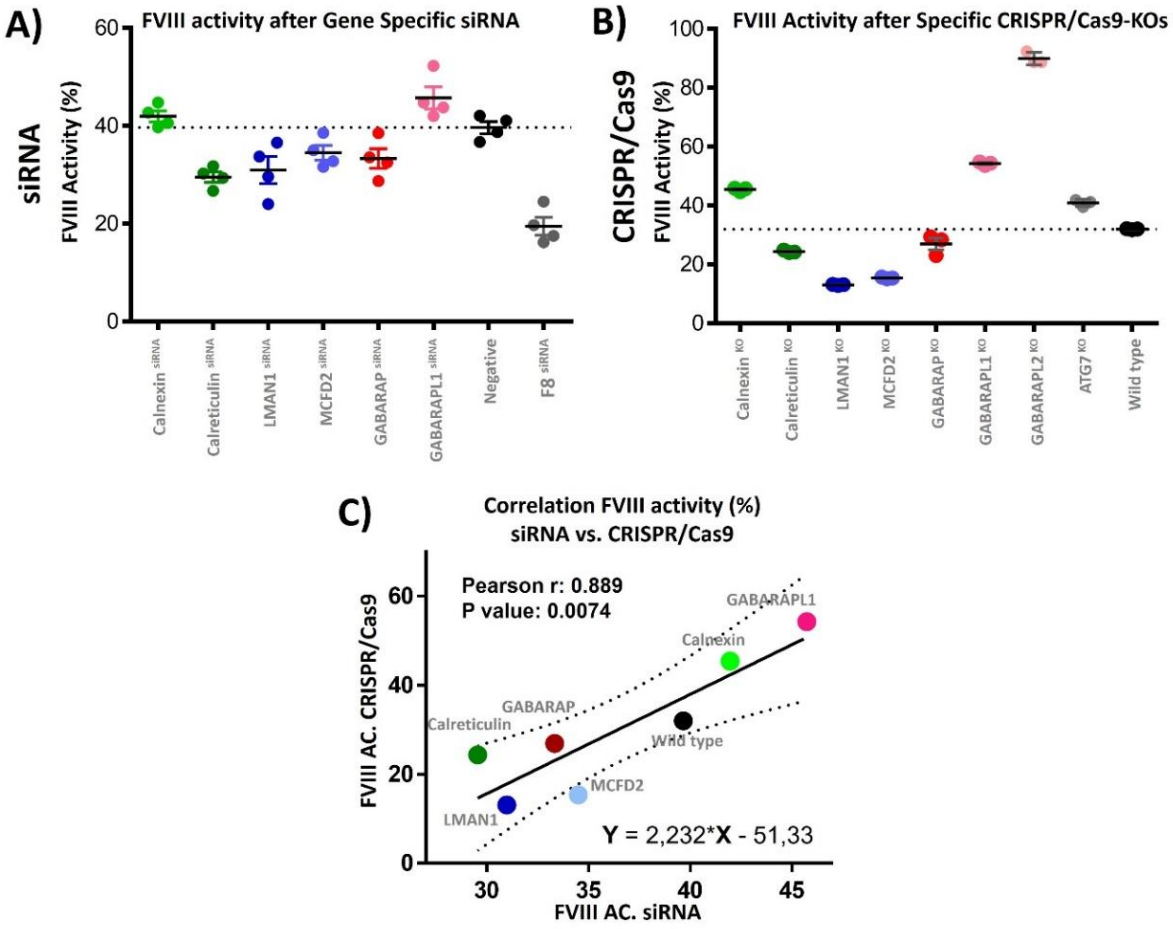

Figure 13. Effects of Protein Knockouts/Knockdowns on FVIII Secretion Assessed by a Two-Stage Chromogenic Assay. A) Dot plot showing FVIII activity levels (%) in the culture medium 48 hours after transfection with gene-specific siRNAs targeting individual proteins in HEK28^{WT} cells. **B)** FVIII activity in the medium of stable CRISPR/Cas9-generated knockout clones. Each dot in **A)** and **B)** represents one of the triplicate measurements per cell clone. **C)** Correlation curve comparing FVIII activity in the medium of siRNA-mediated knockdown cells to that of CRISPR/Cas9-based knockout cells (Pearson's r = 0.889, P = 0.0074).

4.2. Secretion levels of FV and vWF correlated with FVIII-Secretion in HEK28^{WT} and CRISPR/Cas9-KO Cells

To investigate the effects of the same set of single CRISPR/Cas9-KOs on two other heavily glycosylated, high molecular weight coagulation factors—Factor V (FV) and von Willebrand factor (vWF)—in parallel to FVIII, FV and vWF were transiently separately expressed in the parental HEK293 cell line (HEK293p), HEK28^{WT}, and the single CRISPR/Cas9-KO clones. The aim of this experiment was to monitor the effects of these gene-KOs on FV and vWF secretions and to further compare it to those of FVIII secretion levels. FV was chosen since, like FVIII, it interacts with the cargo receptor complex composed of LMAN1 and MCFD2, besides sharing with FVIII the characteristic of having a heavily glycosylated B-domain [33]. VWF was selected due to its shared characteristics with FVIII, including extensive glycosylation and high molecular weight. Additionally, vWF serves as a chaperone for FVIII in the bloodstream and is co-stored with FVIII in Weibel-Palade bodies (WPBs) when both proteins are co-expressed [84].

Before assessing the activity measurements of FV and vWF in the whole experimental set up, their expression was confirmed by WB and IF Staining. FV was expressed using 4 µg of the plasmid (pMT2-V [GI 5138] 40515 TM) containing an SV40 ori and adenovirus major late (AdMLP) promoters responsible for constitutive expression of FV. Media and lysates were collected post-transfection in HEK28^{WT} and HEK293p cell lines as a preliminary step before expanding to a larger experimental setup. WB analysis revealed the presence of FV in the media (300-330 kDa for single-chain FV and ~100 kDa for heavy-chain FV) but FV was not easily detected in cell lysates **(Figure 14 A).** Immunofluorescence staining further confirmed FV expression, though the number of cells expressing FV appeared to be low **(Figure 14 C, FV shown in red).** After verifying successful FV expression, the experimental setup as scaled up to include the KO-cell lines **(Figure 14 B).**

For the verification of vWF expression, 2 µg of pcDNA3.1-WT-vWF (containing a CMV promoter therefore constitutively expressing vWF) were also first transfected into, HEK28^{WT} and Atg7^{KO} cells before scaling up the experimental set up. Unlike FV, vWF was detected in the cell lysates, appearing as a condensed smear with a MW >250 kDa

(Figures 14 D and E), but was not detected by WB in media samples. However, the detection of vWF by WB in cell lysates was sometimes challenging and not consistently straightforward. Despite these difficulties in WB detections of vWF, IF microscopy clearly confirmed its expression **(Figure 14 F, vWF shown in green),** with a higher number of cells expressing vWF compared to FV. In summary, the results from both Western blotting and immunofluorescence microscopy were consistent, showing detectable amounts of vWF protein **within the cells** and abundant FV in the **extracellular media (secreted).**

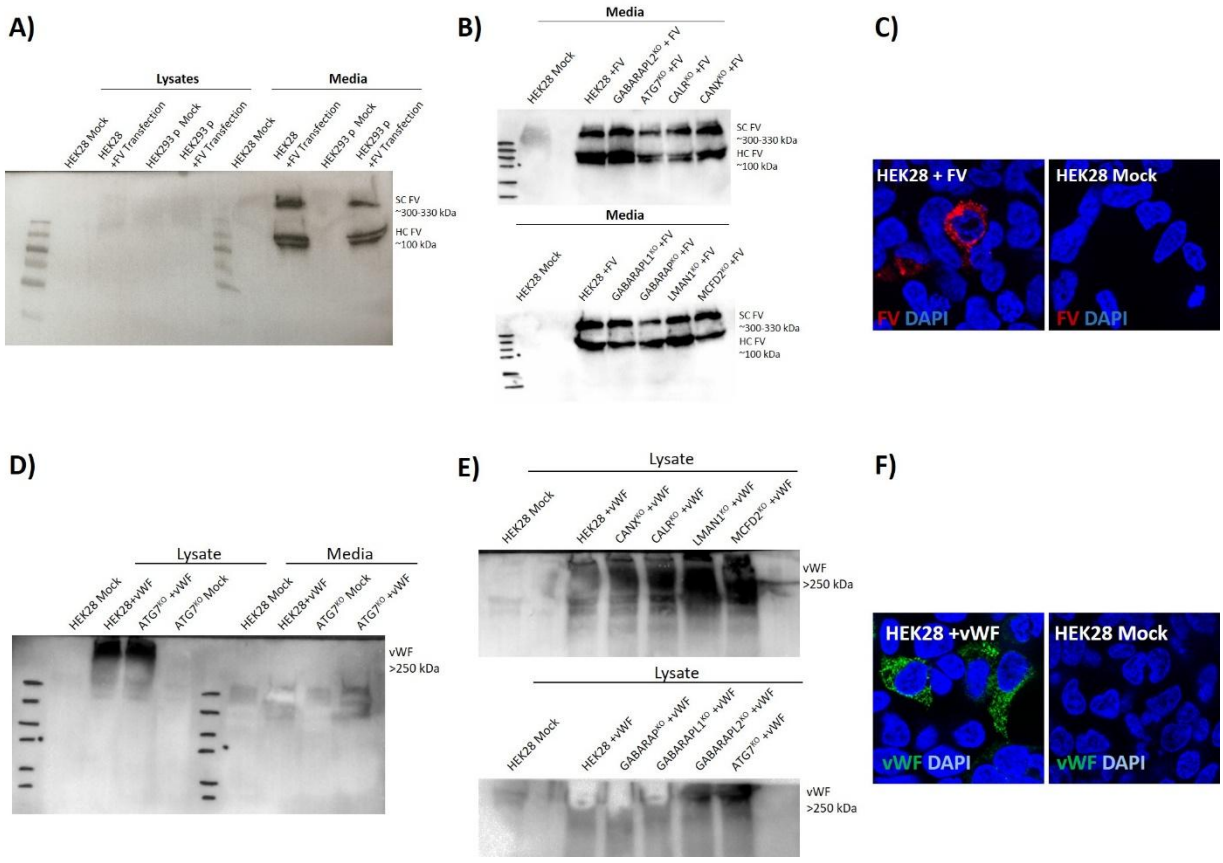

Figure 14. Establishment of FV and vWF Expression in HEK28^{WT} and Single CRISPR/Cas9 Knockouts. The upper and lower panels show the procedures for establishing FV and vWF expression, respectively. The left panel **(A, D)** presents Western blot analyses detecting FV and vWF in media and lysates of HEK293p and HEK28^{WT} cells for FV, and in HEK28^{WT} and ATG7^{KO} cells for vWF. The middle panel **(B, E)** shows Western blot results for FV expression in media and vWF expression in lysates of HEK28^{WT} and CRISPR/Cas9 single knockout cells. The right panel **(C, F)** displays representative immunofluorescence images of FV (red) and vWF (green) in HEK28^{WT} cells before and after transfection with FV and vWF expression plasmids. Blue is DAPI.

After establishing the expression of both FV and vWF proteins, their extracellular activity levels upon cell media collection was assessed. FV activity was measured using a one-stage clotting assay (using Owren's Veronel Buffer, Dade® Innovin® and Factor V deficient Plasma from Siemens Healthineers), while vWF activity was evaluated through a latex-particle-based immunoturbidimetric assay (INNOVANCE® VWF Ac assay kit, Siemens Healthineers), and FVIII activity was determined using a two-stage chromogenic assay and an aPTT-clotting assay (using Factor VIII Chromogenic Assay kit from Siemens Healthineers). Despite the discrepancies in protein detection of FV and vWF in media and lysates, both proteins showed measurable activity levels in the media of transfected cell lines. In general, levels of FV activity were significantly higher than those of FVIII and vWF levels, e.g., with FV levels reaching approximately a range of 140% in HEK293p cells **(Figure 15, upper lane).** In contrast, vWF activity measurements were similar in magnitude to FVIII activity levels, e.g., reaching around 53% in GABARAPL1^{KO} **(Figure 15, lower lane).**

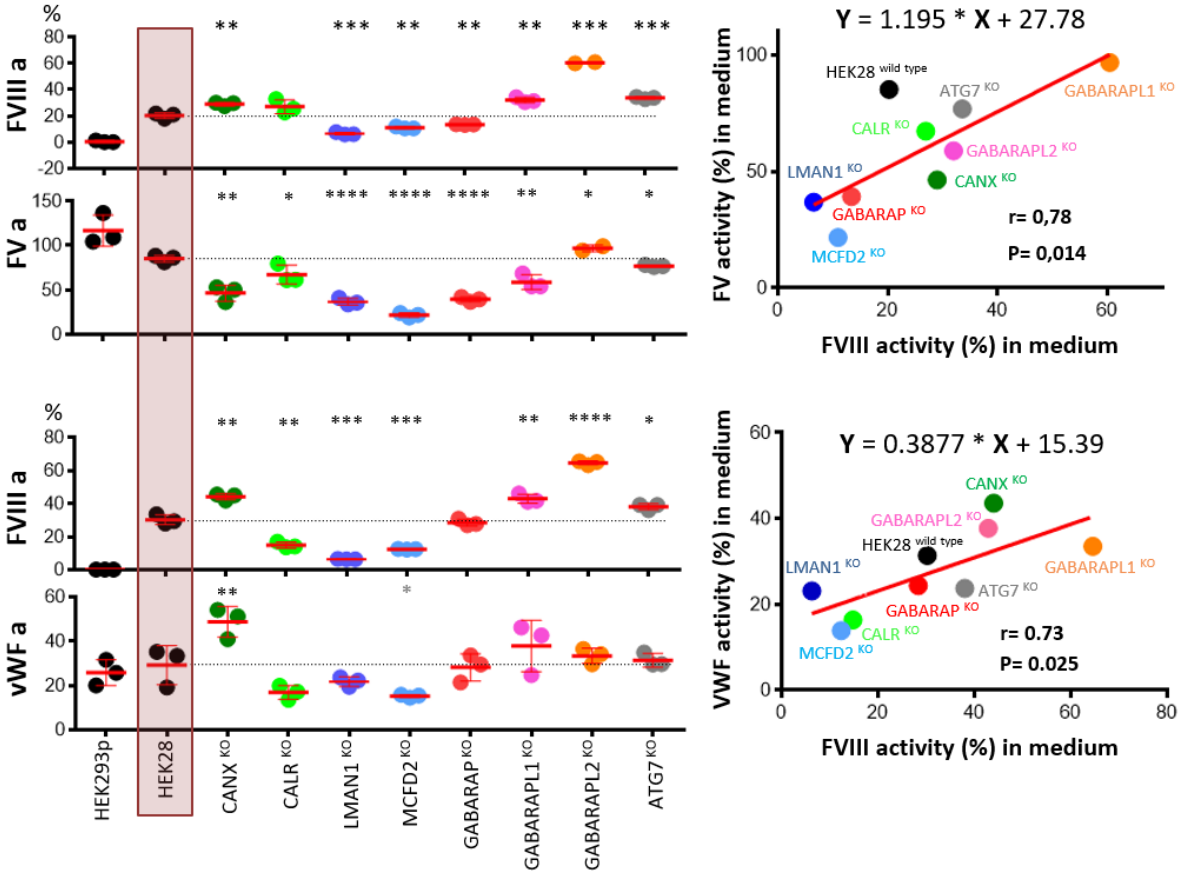

Figure 15. Effects of Stable CRISPR/Cas9 Knockouts on Transient secretions of FV and vWF. The upper and lower left dot plot diagrams represent FV and vWF (along with FVIII) secretion levels, respectively. Each dot represents one of the technical triplicates for each cell clone. Different cell clones are distinguished by specific color codes. The right panel presents a correlation diagram between FVIII activity and either FV or vWF activities in the various cell clones. Significant differences compared to HEK28^{WT} controls are indicated by asterisks ($p < 0.05$; $p < 0.01$; *$p < 0.001$; **$p < 0.0001$).

These findings aligned with previous observations showing the FV protein to be more readily detected in the media, while the vWF protein was more prominent in cell lysates **(Figure 14, Western Blots).**

Trends of FV and vWF secretions were very similar to those of FVIII in the different knockouts, showing only slight notable differences. For instance, CANX^{KO} and GABARAPL1^{KO} did not increase FV secretion above the levels of HEK28^{WT}, as observed for FVIII. On the other hand, in the GABARAPL2^{KO} cells, vWF activity was more comparable to vWF secretion levels in HEK28^{WT}, which was different for FVIII showing much higher levels in the absence of GABARAPL2. Furthermore, when analyzing the

effects of KO-cells on vWF and FV secretions in relation to FVIII, both FV and vWF activities showed a strong positive correlation to FVIII media activity levels (r = 0.78, p value = 0.014; r = 0.73, p value= 0.025 for FV and vWF, respectively) **(Figure 15, Right).**

It is also noteworthy to mention that the observed levels of FV accumulation in the media of HEK293 parental cells (i.e., in the absence of FVIII expression and secretion) were higher compared to HEK28^{WT} cells, where both FV and FVIII were co-expressed. In contrast, this pattern was not observed with vWF. The expression levels of vWF in the HEK293 parental cell line were very similar to those in the HEK28^{WT} cells hinting that the co-expression of vWF with FVIII did not impose the same burden or pathway conflict. **(Figure 15)**

4.3. FVIII and GABARAP Interact Weakly, Transiently, or Potentially via an Intermediary Protein

In order to assess the interaction between FVIII and GABARAP, three interaction approaches were employed: the **Bio-layer Interferometry (BLItz)**, **immunofluorescence microscopy** and **co-localization** as well as **immunoprecipitation** experiments. In fact, Bio-layer interferometry is capable of detecting weak or transient interactions as its purpose is actually the assessment of the strength or the binding affinity (KD) between two proteins in real time based on protein dissociation/association ratios [(85)]. On the other hand, Immunofluorescence staining and further co-localization analysis evaluate the extent of spatial proximity between two proteins, however does not always reflect a direct physical contact between them. This is actually achieved by the assessment of the fluorophore signal overlaps and intensity relationships [(86-88)]. While the first two approaches give hints on weak and transient interactions, protein immunoprecipitation and co-immunoprecipitation procedures capture stable and strong protein interactions, which are likely to be in stable complex with each other [(89)].

4.3.1 Bio-layer Interferometry Assay Reveals Weak Binding of FL-FVIII to GABARAP, and no-binding of BDD-FVIII variant to GABARAP

i. Immobilization of GABARAP on anti-His coated Biosensors

As earlier described, the recombinant GABARAP protein was readily purchased (rGABARAP C-terminal-His-tagged) and verified by running on SDS-PAGE using 16% Tris-Tricine gels, followed by a WB probing **(Figure 16. A, Detection His-tag).** Along with GABARAP, FVIII products were included (Full length-FVIII: Kovaltry/Advate; BDD-FVIII: Nuwiq/Refacto; Plasma-derived-FVIII: Octanate/Beriate), in addition to HEK293p cell extract. All proteins were loaded at a final amount of 300 ng per lane.

Membrane first probing with an anti-His antibody showed bands of 16 kDa in the lane where rGABARAP-His was loaded, corresponding to the MW of the GABARAP protein. Bands of 70-100 kDa, 130 kDa and above 250 kDa for Octanate; of 130 and 250 kDa for Beriate; and a band of 70-100 kDa in Nuwiq were observed, indicating the presence of the His peptide in these FVIII concentrates **(Figure 16. A, Detection His-Tag)**.

Second membrane probing using a polyclonal FVIII antibody showed for Kovaltry and Advate bands corresponding to the FVIII protein at 250 kDa, 100 kDa and very slight bands of 70 kDa representing the expected bands for the full-length variant of FVIII; for Nuwiq and Refacto bands of 170 kDa and 100 kDa chains going in parallel with the lower molecular weight of the B-deleted-domain FVIII; and for Octanate and Beriate bands of 250 kDa and weaker bands of ~120 kDa and 70 kDa were observed **(Figure 16. A, detection FVIII).** Due to the difficulties in the separation of high molecular weight proteins on 16% Tris-Tricine gels, probing of FVIII was repeated using a 7.5% Tris-Glycine gel and band sizes were better determined and confirmed **(Figure 16. B)**. This observed heterogeneity in FVIII sub-types and configurations across the various FVIII concentrates was expected, given the variations occurring during purification processes and the nature of the FVIII protein being extracted during manufacturing. Finally, probing of GAPDH showed a thick band of 36 kDa in HEK293p cell lysates, as expected, and a slight band in Octanate **(Figure 16. A, Detection GAPDH)**.

Based on these results, the further Bio-layer interferometry assay (BLItz) was carried on using full-length FVIII Kovaltry and BDD-FVIII Refacto, to avoid any interference of an unspecific His peptide during the next procedure, as well as to assess possible differences in the binding of the GABARAP protein to both concentrates.

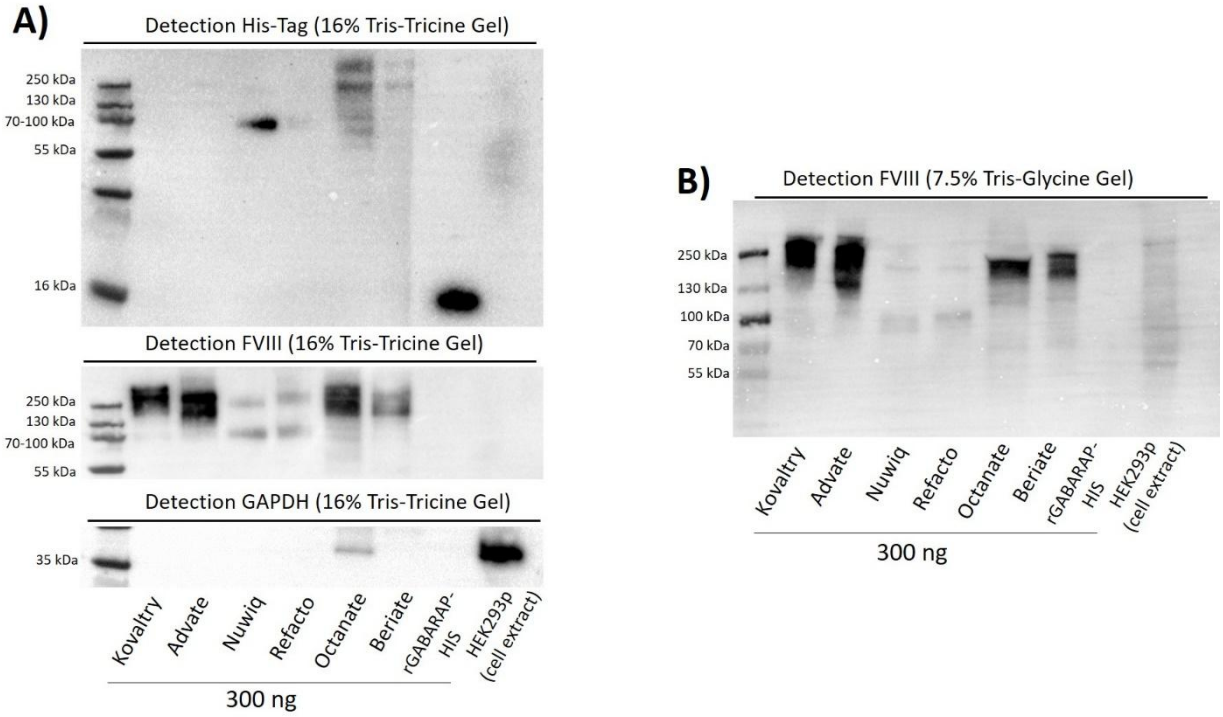

Figure 16. Verification of Recombinant FVIII and GABARAP Proteins for Bio-Layer Interferometry Assay. A) shows 16% Tris-Tricine Western blot gel analysis of recombinant FVIII proteins (full-length FVIII: Kovaltry, Advate; B-domain-deleted FVIII: Nuwiq, Refacto; and plasma-derived FVIII: Octanate, Beriate) and anti-His-tagged GABARAP proteins, each loaded at 300 ng in addition to cell-extract (lysate) of HEK293p as a control. Blots were probed with anti-His, FVIII polyclonal (SAF8C), and GAPDH (housekeeping gene) antibodies. **B)** Repeats the same experiment using a 7.5% Tris-Glycine gel to better resolve FVIII protein bands, as these gels are more suitable for visualizing larger molecular weight proteins.

ii. Immobilization of FVIII on Streptavidin Coated Biosensors

Since the Bio-layer Interferometry experimental set up included first immobilizing GABARAP on the biosensor and FVIII in solution, a reverse protocol was additionally performed: i.e. to fix the FVIII concentrates on the tip of the biosensors and to afterwards examine it's binding to GABARAP. For this, FVIII products were biotinylated using the EZ-Link™ Sulfo-NHS-LC-Biotin, No-Weigh™ Format kit from ThermoFisher. To

verify the success of the biotinylation procedure, raw (diluted in H_2O), desalted (only buffer exchange to PBS) and subsequent biotinylated FVIII products were probed using HRP conjugated Streptavidin by Dot Blot and Western Blot assays **(Figure 17).** Dot Blot visualization showed for biotinylated Kovaltry (octocog alfa: Kovaltry®) and Refacto (moroctocog alfa: Refacto®) along with an anti-Flag biotinylated antibody (used as positive control) clear black dots upon probing with HRP-Streptavidin. These results were mirrored in WB of the same samples in addition to a recombinant biotinylated BSA protein (used as a positive control). In the lane where biotin- Kovaltry was loaded, incubation with HRP-Streptavidin yielded a clear band of around 250 kDa corresponding to the single chain of full length- FVIII, whereas in the biotinylated Refacto- lane, a faint band of around 170 kDa corresponding to the single chain, a band of 100 kDa corresponding to the heavy chain, and a band of around 70 kDa representing the light chain (all) of BDD- FVIII, were documented.

After optimization of protein concentrations to be loaded on the biosensors (rGABARAP and FVIII- products), the binding of the other ‘’in solution‘’ proteins at five different concentrations was tested. At the end of each experiment binding affinities ($KD = K_{off}/K_{on}$) were calculated based on the ratios of dissociated (K_{off} or K_d) to

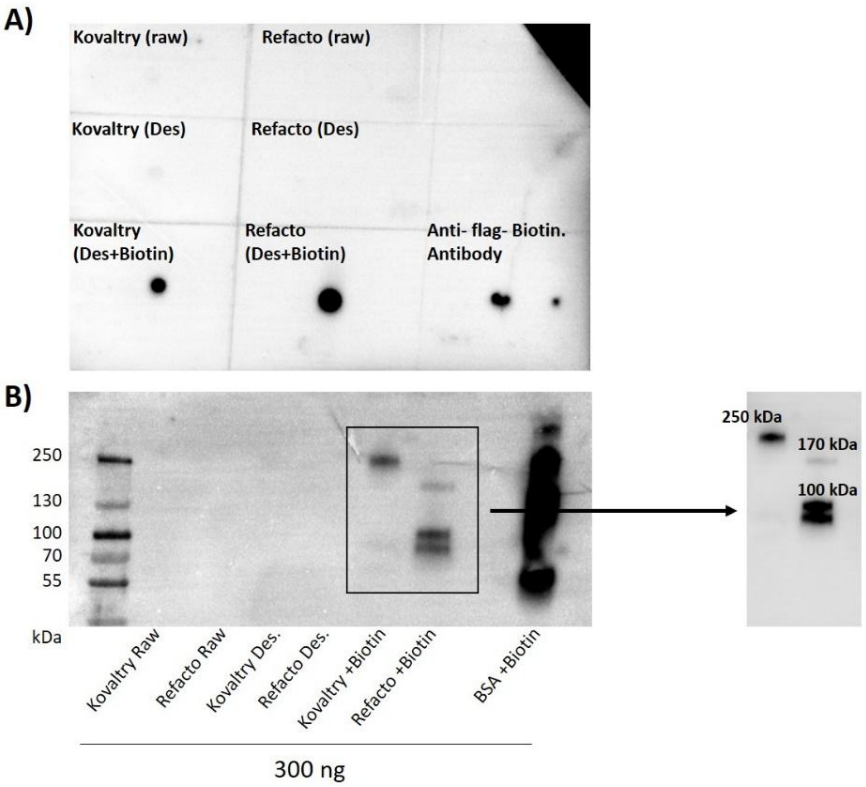

Figure 17. Verification of FVIII Biotinylation Procedure for Bio-Layer Interferometry Assay. A) Dot Blot of where raw, desalted (PBS buffer-exchanged), and biotinylated Kovaltry (full-length) and Refacto (B-deleted-domain) FVIII products were loaded (300 ng) and detected following biotinylation using EZ-Link™ Sulfo-NHS-LC-Biotin, No-Weigh™ Format kit from ThermoFisher. A biotin-conjugated antibody was used as a control. **B)** Western blot where the same biotinylated FVIII proteins, along with recombinant BSA, were loaded and probed with a biotin-specific antibody. The **right panel** provides a magnified and optimized image (after background noise reduction and exposure adjustment) highlighting the successful biotinylation of Kovaltry and Refacto FVIII products. Detections were done using HRP-Streptavidin.

associated (K_{on} or K_a) estimated amount of proteins (visualized as association and dissociation curves). This was done through the optical shift- based detection system executed by the N1 instrument (BLItz) device. Using the analysis tool integrated in the BLItz Pro™ software (SARTORIOUS;

Version 1.2.1.5), curves were normalized to a common association and dissociation starting points and KDs (binding affinities) were calculated accordingly.

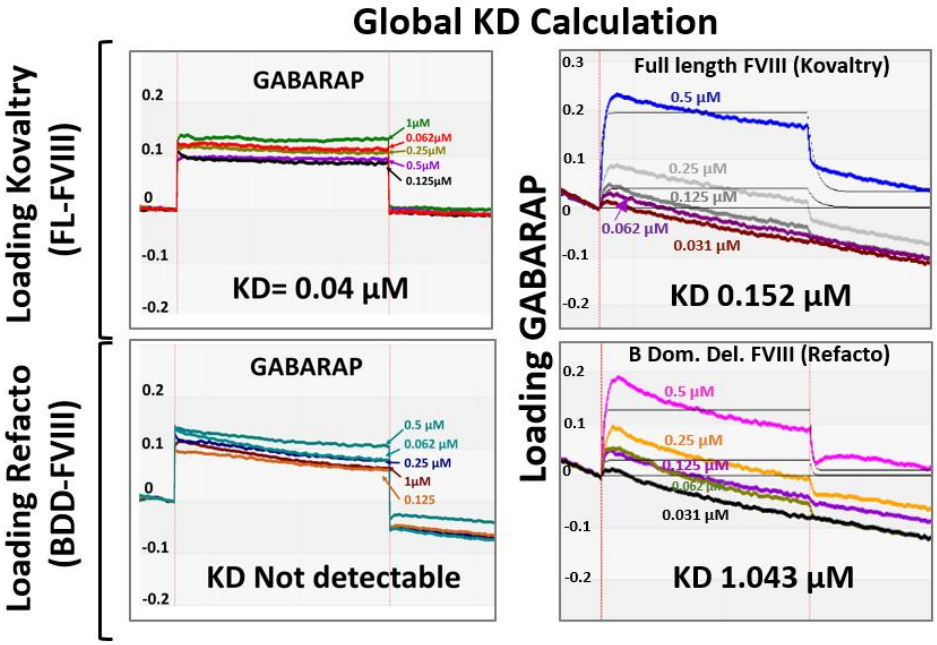

Figure 18. Assessment of GABARAP-FVIII Interaction by Bio-Layer Interferometry (BLI) Assay. BLItz-based interaction analysis was performed to assess the binding dynamics between GABARAP and FVIII. The **left** and **right** panels represent experiments in which recombinant FVIII proteins (upper panel: full-length FVIII [Kovaltry], lower panel: B-domain deleted FVIII [Refacto]) or GABARAP were immobilized on streptavidin and anti-His biosensors, respectively. Following immobilization, the analytes (GABARAP or FVIII proteins) were introduced to measure association phases. For each of the four binding tests, different protein concentrations were used, and the global dissociation constant (KD) was determined as the ratio of $K_{dissociation}$ to $K_{association}$ (K_{off}/K_{on} or $K_{diss.}/K_{ass.}$) using BLItz Pro™ software (Sartorius, version 1.2.1.5). Each experimental setup included five analyte concentrations to ensure accurate KD assessment.

Full length- FVIII (Kovaltry) immobilization on Streptavidin biosensors, showed binding to GABARAP (KD = 0.04 µM) whereas no interaction nor binding was detected between BDD-FVIII (Refacto) and GABARAP. Reversely, fixation of the His-tagged-rGABARAP protein on Histidine- coated biosensors, showed a lower KD= 0.152 µM for FL-FVIII (Kovaltry) and a higher one for BDD-FVIII (Refacto) KD= 1.043 µM which translates to a stronger binding of GABARAP to Kovaltry and a lower one to Refacto **(Figure 18).**

4.3.2. IF- Staining reveals low co-localization levels of FVIII with GABARAP in HEK28^{WT}

Fluorescence co-staining in HEK28^{WT} cells showed a moderate to low co-localization of FVIII and GABARAP in a punctuate-structured manner **(Figure 19. white arrows showing yellow dots in HEK28^{WT}).** In addition, quantification of this co-localization by the Zen Blue Pro 2.6 software revealed an average of Pearson correlation coefficients (PCCs) of approximately 0.3 **(Figure 19. Dot plot boxes).** This average, derived from a cell population of around 250, which showed considerable fluctuation in individual PCC values before converging to the mean of 0.3. These findings reinforce the notion of a transient weak or indirect association between GABARAP and FVIII, which can be challenging to detect consistently in different cells.

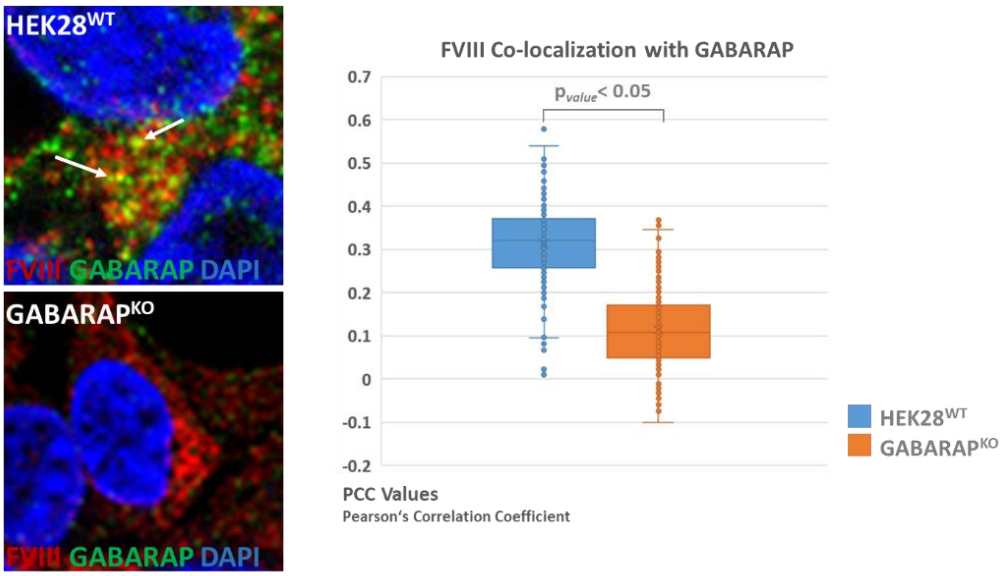

Figure 19. Immunofluorescence Staining and Co-localization Assessment of FVIII with GABARAP in HEK28^{WT} Cells. The left panel presents immunofluorescence images showing FVIII (red) and GABARAP (green) staining in both HEK28WT and GABARAPKO cells. Yellow overlaps, indicated by white arrows, highlight the co-localization of FVIII with GABARAP (in a dotted manner). The right panel displays a dot plot box diagram showing the co-localization values of FVIII with GABARAP in both HEK28WT (blue box) and GABARAPKO (orange box) cells. Co-localization was assessed using Zen 2.6 Pro software, with Pearson's correlation coefficients (-1 to 1) calculated for a population of 240 cells.

4.3.3. Immunoprecipitation and Co-Immunoprecipitation Reveal No Direct Interaction between FVIII and GABARAP

The interaction between FVIII and GABARAP using immunoprecipitation (IP) and co-immunoprecipitation (co-IP) assays was as well investigated. Cell lysates were collected and incubated with a polyclonal FVIII antibody (SAF8C), followed by IP procedures. The samples were then subjected to SDS-PAGE and WB analysis.

A band above 250 kDa was detected in the HEK28^{WT}, CANX^{KO}, CALR^{KO}, LMAN1^{KO}, and GABARAP^{KO} lanes, all of which were subjected to IP using FVIII **(Figure 20. A, first gel)**. In the input lanes, a smear of nonspecific bands was observed. Following this, the membrane was stripped and re-probed with an anti-CANX and anti-CALR antibodies. The two ER chaperones were chosen as a positive controls, given the established knowledge on their interaction with FVIII. This revealed, CANX bands at 100 kDa in HEK28^{WT}, CALR^{KO}, LMAN1^{KO} and GABARAP^{KO} samples but not in CANX^{KO} **(Figure 20. A, second gel).** Similarly, bands around 55kDa for CALR were observed in the FVIII-IP samples from HEK28^{WT}, CANX^{KO}, LMAN1^{KO}, and GABARAP^{KO} cells but not in CALR^{KO}, confirming the expected direct interaction/binding between FVIII and Calreticulin **(Figure 20. A, third gel).** The same samples were then loaded onto 16% Tris-Tricine gels, to ensure clear detection of the small GABARAP protein (~14-16 kDa). Probing the membranes with an anti-GABARAP antibody revealed bands around 15 kDa in the input lanes of HEK28^{WT} cells and in the flow-through collected during IP **(Figure 20. A, fourth gel).** However, GABARAP did not immunoprecipitate with FVIII in neither HEK28^{WT}, nor modified cells. **Figure 20. B** shows a magnified view of the gels after extensive washing and re-imaging for enhanced clarity.

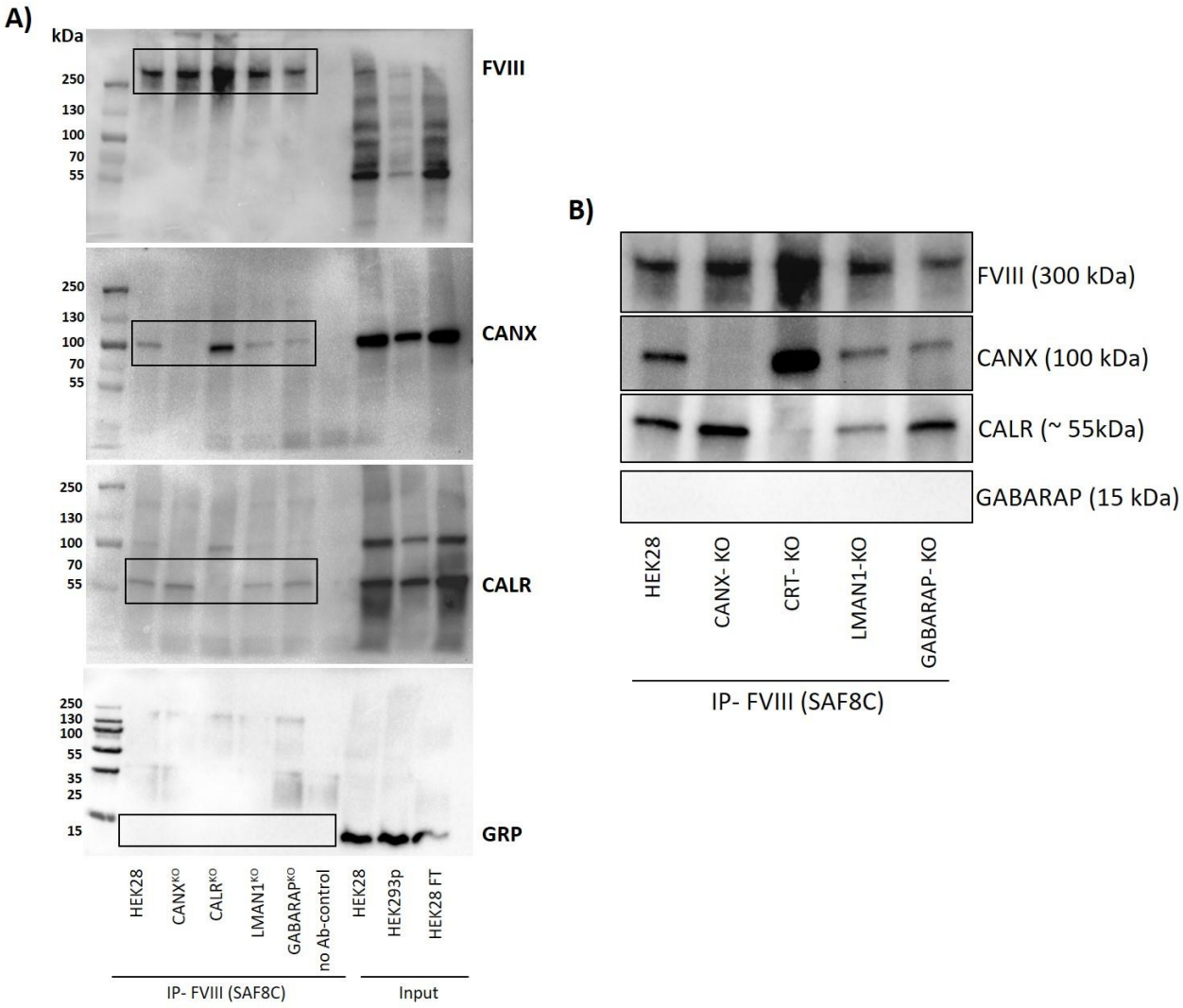

Figure 20. Assessment of FVIII-GABARAP Physical Interaction by IP (immunoprecipitation) and Co-IP (Co-Immunoprecipitation) Assays. A) Western blot analysis of cell extracts following immunoprecipitation (IP) of FVIII using a polyclonal antibody (SAF8C) from HEK28^{WT}, CANX^{KO}, CALR^{KO}, LMAN1^{KO}, and GABARAP^{KO} cell extracts. The PVDF- membrane containing transferred proteins was probed with antibodies against FVIII, CANX, CALR, and GABARAP, and a set of corresponding secondary HRP-antibodies. Controls include HEK28WT, HEK293p, and the flow-through of HEK293p, were all loaded on the same gel. **B)** Magnified image of the same gel, focusing on the lanes where each protein is expected to appear.

4.4. Clustering Analysis of FVIII Co-localization with Thirteen Intracellular Markers brings GABARAP^{KO}-, CANX^{KO}- and CALR^{KO} -clones *''Together''*.

Characterizing the effect of each CRISPR/Cas9-KO on FVIII intracellular whereabouts and secretion was the first step toward unveiling the potential roles of GABARAP(s) through which these proteins operate in the trafficking machinery of FVIII. In combination with corresponding FVIII measurements, this provides hints regarding the potential mechanisms in which these proteins are involved, as well as the possible compensatory phenomena occurring upon KO-induced stresses.

This was approached by co-staining FVIII with 13 intracellular markers. These markers included coat and ERGIC proteins such as Sec31a, COPB; Cis- and Trans- Golgi markers such as GM130, TGN46; Post-Golgi markers like Rab8, lysosomal proteins like LAMPI and ARL8B, Autophagosomal markers/related- markers such as LC3B, VAMP8, and Rab26; early endosomes like Rab5, recycling endosomes like Rab11, and late endosomes like Rab7. Immunofluorescence staining procedures were performed on 4% paraformaldehyde fixed cells, using appropriate combinations of primary and fluorophore conjugated secondary antibodies. Quantitative co-localization measurements using the Pearson's Correlation Coefficients (integrated by the Zen 2.6 pro Software) was adapted. This aims to calculate the degree of co-occurrence between two fluorophore channels per pixel using "Costes" thresholding. The obtained values were incorporated into Qlucore omics explorer 3.6 to organize the Data into Principal Component Analysis (PCA) plots and Heat Map Matrices. **(Figure 21)**

FVIII was initially tracked in HEK28^{WT} cells in order to determine a standard pattern of its distribution under normal conditions **(Figure 21. A).** In parallel, this pattern was identified in the remaining of the CRISPR/Cas9-KOs and compared to that of HEK28^{WT} **(Figure 21. B)**. In wild type cells, FVIII was detected at moderate to high levels with markers belonging to the ERGIC compartment (**Sec31a (COPII)** PCC= 0.33, SD= 0.15; **COPB (COPI)** PCC= 0.64, SD= 0.1) as well as the Golgi apparatus (**GM130** PCC= 0.47, SD= 0.09; **TGN46** PCC= 0.38, SD= 0.18). FVIII also mildly co-localized to **Rab7** (PCC=

0.31, SD= 0.1), **VAMP8** (PCC= 0.37, SD= 0.1) and **Rab8** (PCC= 0.29, SD= 0.1), proteins marking the late endosomes (Rab7), autophagosomes/amphisomes (VAMP8), and Golgi-to-plasma membrane vesicles (Rab8). Nevertheless, very less to almost undetectable levels of co-occurrence were observed for FVIII in other autophagosomal and lysosomal (**LC3B** PCC= 0.06 SD= 0.08; **Rab26** PCC= -0.03, SD= 0.06; **LAMPI** PCC= 0.05, SD= 0.08, **ARL8B** PCC= 0.06, SD= 0.08) related structures, as well as early (**Rab5** PCC= 0.02, SD= 0.1) and recycling endosomes (**Rab11** PCC= 0.07, SD= 0.1). **(Figure 21. A)**

Following the same strategy, FVIII intracellular patterns were identified in the remaining of the CRISPR/Cas9-KO clones. The latter investigation revealed the clustering of the cell lines within three groups visualized by the samples PCA plot **(Figure 21. B left):** group **S1** included the ERGIC transporters LMAN1^{KO} and MCFD2^{KO} (along the PC1 (43%)); group **S3** involved ER Chaperones knockouts CANX^{KO}, CALR^{KO} along with GABARAP^{KO} (along PC2 (19%)); and group **S2** contained GABARAPL1^{KO}, GABARAPL2^{KO} (along PC3 (15%)) which were close to WT-HEK28 and ATG7^{KO} (between PC3 and PC1). When projecting onto the variables' PCA plot **(Figure 21. B right);** it was as well possible to determine the divisions of markers (variables) across three categories: category **V1** which included markers of lysosomal and late endosomal structures, **V2** involving mostly ERGIC and Golgi proteins (classical secretory route) and **V3** mainly consisting of autophagosomal-, early endosomal- and polarized secretory vesicles- related markers.

Interestingly, GABARAP^{KO} clustered closely with the ER chaperone knockouts CANX^{KO} and CALR^{KO} in S3, and unexpectedly ''distanced'' itself from its homolog knockouts, GABARAPL1^{KO} and GABARAPL2^{KO}, which were clustered in group S2. This indicates that GABARAP affects the trafficking machinery of FVIII more similarly to the ER Chaperones Calnexin and Calreticulin, rather than its homologs from the Atg8 protein family, GABARAPL1 and GABARAPL2. This emphasizes a certain functional divergence among the GABARAPs, which was evident not only in FVIII accumulations in media but also within the cells. Moreover, in S3-related knockouts, FVIII exhibited fewer co-localizations with markers from the V3 group, while showing higher co-localizations with markers belonging to the V1 and V2 groups. In contrast, LMAN1^{KO} and MCFD2^{KO},

both part of group S1, displayed lower co-localization of FVIII with proteins belonging to groups V1 and V2, as expected, but higher co-localization with markers of the V3 group.

Remarkably, S1 and S3 exhibited completely opposite phenotypes, with S1 demonstrating higher co-localization of FVIII with markers from one group (V3: VAMP8, LC3B, Rab26, Rab5 and Rab8a) and lower with markers belonging to V1 (sorting endosomes and late endosomal-lysosomal structures: LAMP1, Rab7 and Rab11) and V2 (mostly classical secretory proteins: TGN46, GM130, Sec31a (COPII), COPB (COPI) in addition to ARL8B) groups, whereas S3 showed a clear contrasting FVIII intracellular co-localization phenotype in comparison to S1, specifically in regards of co-localization of markers belonging to the V3 group, **(Figure 21. B, middle heat map).** These observations emphasize the roles of LMAN1 and MCFD2 transporter proteins in promoting specifically the ER to Golgi dependent secretion of FVIII as well as its processing with proteins related to the lysosomal machinery. On the other hand, it appears that Calnexin, Calreticulin and interestingly GABARAP aid the trafficking of FVIII with autophagosomes-, post-TGN transport-, and plasma membrane-related proteins.

Finally, clustering of the ER-chaperones knockouts $CANX^{KO}$ and $CALR^{KO}$ together, given the similarities in their roles as ER quality control officers on one hand, and of the ERGIC transporters knockouts $LMAN1^{KO}$ and $MCFD2^{KO}$ provided more confidence while interpreting the findings, as these results were already well anticipated.

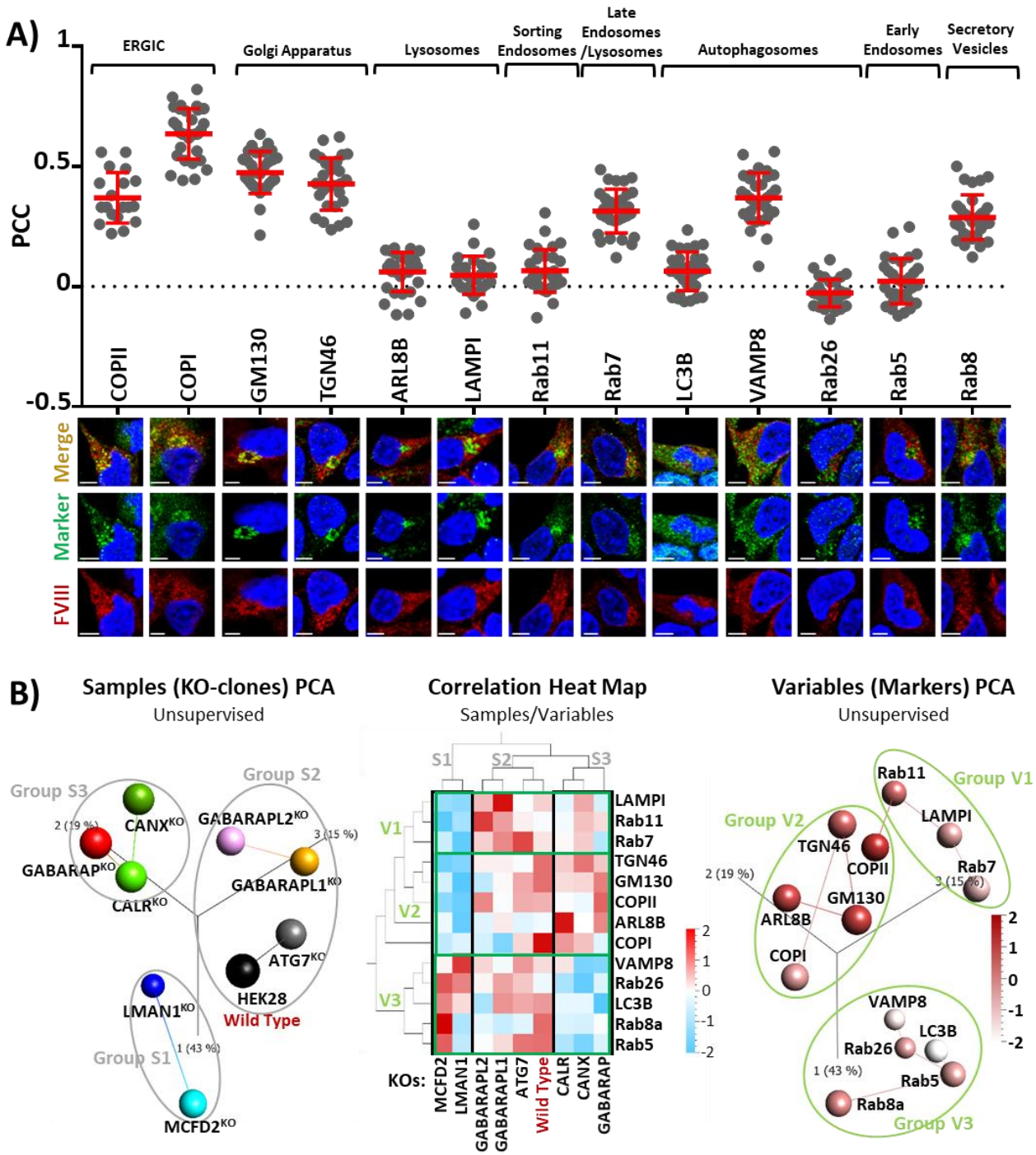
A)
ERGIC
Golgi Apparatus
Lysosomes
Sorting Endosomes
Late Endosomes /Lysosomes
Autophagosomes
Early Endosomes
Secretory Vesicles
PCC
1
0.5
0
-0.5
COPII
COPI
GM130
TGN46
ARL8B
LAMPI
Rab11
Rab7
LC3B
VAMP8
Rab26
Rab5
Rab8
Merge
Marker
FVIII
B)
Samples (KO-clones) PCA
Unsupervised
Group S3
Group S2
Group S1
CANX^KO
GABARAP^KO
CALR^KO
GABARAPL2^KO
GABARAPL1^KO
ATG7^KO
HEK28
Wild Type
LMAN1^KO
MCFD2^KO
2 (19 %)
3 (15 %)
1 (43 %)
Correlation Heat Map
Samples/Variables
S1
S2
S3
V1
V2
V3
LAMPI
Rab11
Rab7
TGN46
GM130
COPII
ARL8B
COPI
VAMP8
Rab26
LC3B
Rab8a
Rab5
KOs:
MCFD2
LMAN1
GABARAPL2
GABARAPL1
ATG7
Wild Type
CALR
CANX
GABARAP
2
1
0
-1
-2
Variables (Markers) PCA
Unsupervised
Group V1
Group V2
Group V3
Rab11
LAMPI
TGN46
COPII
Rab7
GM130
ARL8B
COPI
VAMP8
LC3B
Rab26
Rab5
Rab8a
2 (19 %)
3 (15 %)
1 (43 %)

Figure 21. Clustering Analysis of FVIII Co-localization with Thirteen Intracellular Markers brings GABARAP^{KO}-, CANX^{KO}- and CALR^{KO} -clones *"Together"*. A) Upper panel co-localization values (Pearson's Correlation Coefficients (PCCs) [-1, 1]) of FVIII (Y axis: PCC [-1, 1]) with 13 intracellular markers (X axis: COPII, COPI, GM130, TGN46, ARL8B, LAMP1, Rab11, Rab7, LC3B, VAMP8, Rab26, Rab5, and Rab8) in the wild type sample (HEK28), with each marker (n=10-30 cells). Lower panel displays microscopy images of FVIII co-staining (red) with 13 intracellular markers (green) in HEK28^{WT}. Blue is DAPI. Scale bar 5 µm. B) Multi-angled visualization (unsupervised 3D-Principal Component Analysis (PCA) plots and Heat map matrix) of average FVIII co-localization values (PCCs) with 13 intracellular markers in eight CRISPR/Cas9 Knockouts and HEK28^{WT}. Left, 3D-PCA plot of sample (cell lines) and right, of variables (intracellular markers) clustering. Middle, Heat map visualization combining both samples' and variables' PCA plots. The color scale ranges from -2 (blue-negative correlations), to 2 (red-positive correlations). Values close to 0 (white) indicate no correlation. Each square in the Heat map represents a PCC score.

4.5. Co-localization Analysis of the GABARAP Protein against 21 Intracellular Proteins showed Overlaps with FVIII Intracellular Localization

Upon observing the unexpected similarity in the influence of the GABARAP protein with the ER chaperones Calnexin and Calreticulin on the intracellular static distribution of FVIII, as well as its clear separation from its homologs GABARAPL1 and GABARAPL2, the dispersion of the GABARAP protein in HEK28^{WT} was further reviewed. Using immunofluorescence microscopy, GABARAP/FVIII were co-targeted against a broader range of proteins (21 proteins) using specific antibodies.

GABARAP exhibited the highest co-localizations with VAMP8 (PCC= 0.41; SD= 0.05) and Ubiquitin (PCC= 0.34; SD= 0.13), less pronounced co-localizations with GABARAPL1 (PCC= 0.23; SD= 0.11), Rab7 (PCC= 0.2; SD= 0.1), GM130 (PCC= 0.16; SD= 0.08), COPI (PCC= 0.15; SD= 0.04), Sec31a (PCC= 0.15; SD= 0.04), LMAN1 (PCC= 0.17; SD= 0.06) and Calreticulin (PCC= 0.11; SD= 0.07), and almost no co-localization with the remaining of the markers. **(Figure. 22)**

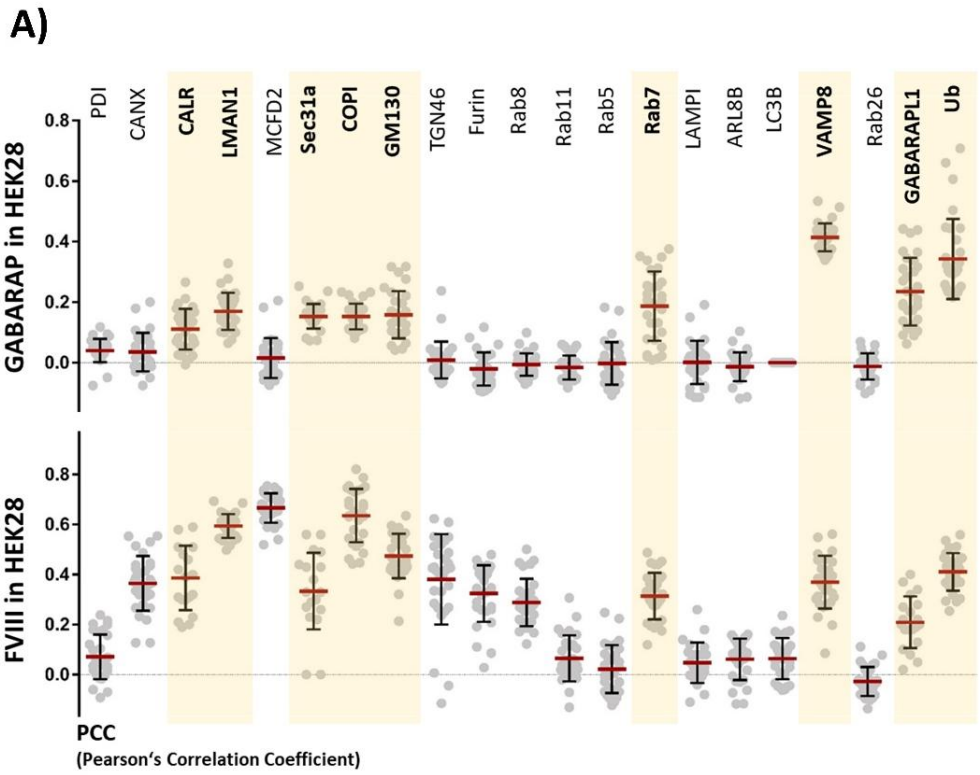
A)
PDI
CANX
CALR
LMAN1
MCFD2
Sec31a
COPI
GM130
TGN46
Furin
Rab8
Rab11
Rab5
Rab7
LAMPI
ARL8B
LC3B
VAMP8
Rab26
GABARAPL1
Ub
GABARAP in HEK28
FVIII in HEK28
0.8
0.6
0.4
0.2
0.0
PCC
(Pearson's Correlation Coefficient)

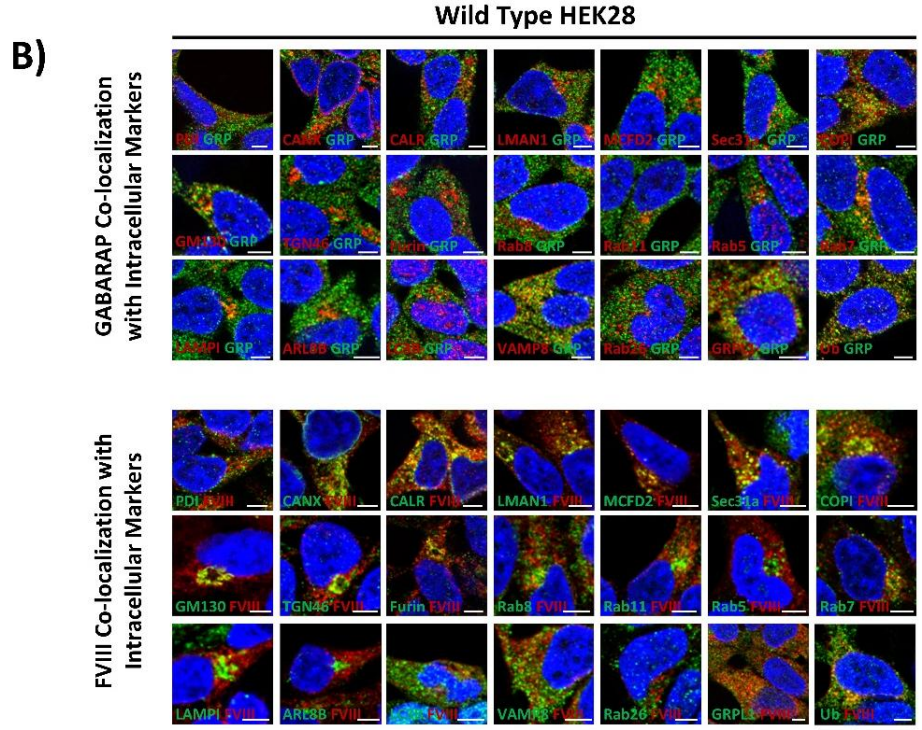
B)
Wild Type HEK28
GABARAP Co-localization with Intracellular Markers
FVIII Co-localization with Intracellular Markers

Figure 22. Both GABARAP and FVIII are localized to the ERGIC Compartment, as well as to Endosomal and Proteasomal Markers. A) Comparison Dot Plots of PCC (Pearson's Correlation Coefficients) co-localization values [-1, 1] of GABARAP (first panel) and FVIII (second panel) with 21 intracellular markers (X axis: PCC values [-1, 1], Y axis: markers; PDI, CANX, CALR, LMAN1, MCFD2, Sec31a, COPII, GM130, TGN46, Furin, Rab8, Rab11, Rab5, Rab7, LAMPI, ARL8B, LC3B, VAMP8, Rab26, GABARAPL1, Ubiquitin) in HEK28^{WT}. Standard deviation was calculated using Graphpad Prism. **B)** Representative immunofluorescence microscopy merged images of GABARAP (green- first panel) and FVIII (red-second panel) with the different marker proteins (red in combination with GABARAP and green in combination with FVIII), respectively. DAPI was used for nuclei staining. Scale bar 5 µm.

In fact, the observed proximity of GABARAP to VAMP8, Rab7, and GABARAPL1 was - more or less- expected since these three proteins represent a common characteristic of participating in regulation and fusion events of autophagosomes with lysosomes, thereby to the autophagy machinery. Moreover, GABARAP's overlap with Rab7 and VAMP8, could also signify a function of GABARAP in endosomal processes related to late-endosomal to lysosomal vesicular transition, as Rab7 is well known as a marker for the late –endosomes intended to maturate into lysosomes. On the other hand, VAMP8 has been described to contribute to the fusion of autophagosomes to lysosomes or endo-lysosomes. This fusion results in the formation of the hybrid so-called organelles: the amphisomes.

The co-localization of GABARAP to proteins of the ERGIC and Cis-Golgi compartments such as LMAN1, Sec31a (COPII), COPB (COPI), and GM130, further suggests functions of GABARAP in facilitating the trafficking of vesicles within these compartments. However, the co-localization of GABARAP to Sec31a and (COPII vesicles) and LMAN1 (ERGIC-53), could as well be linked to vesicle formation event of autophagosomes, as both protein has been described to have roles in facilitating such a process [63, 90].

When overlapping the distribution maps of both FVIII and GABARAP, both maps showed intersections at ERGIC markers LMAN1, Sec31a, COPI and GM130 (ERGIC and Cis-Golgi), endo-lysosomal/autophagosomal markers like Rab7, VAMP8 and GABARAPL1 as well as with Ubiquitin, a marker of proteasomal degradation **(Figure. 22, Figure. 23)**. Overall, these results emphasize the multi-functionality of the GABARAP protein in promoting and aiding FVIII processing and secretion. GABARAP

appears to regulate the trafficking machinery of FVIII either directly, by facilitating vesicle trafficking, or indirectly, by influencing cellular homeostasis and the overall machinery of the cell. Interestingly, and consistent with the latter findings, the lack of GABARAP (GABARAP^{KO}) resulted in less FVIII in the ER (Calnexin and Calreticulin), in the ERGIC compartment (LMAN1, MCFD2, COPB (COPI)), in the *trans*- and *post*- Golgi space, with endosomal markers (TGN46, Furin, Rab7, Rab8a), as well as with ubiquitin,

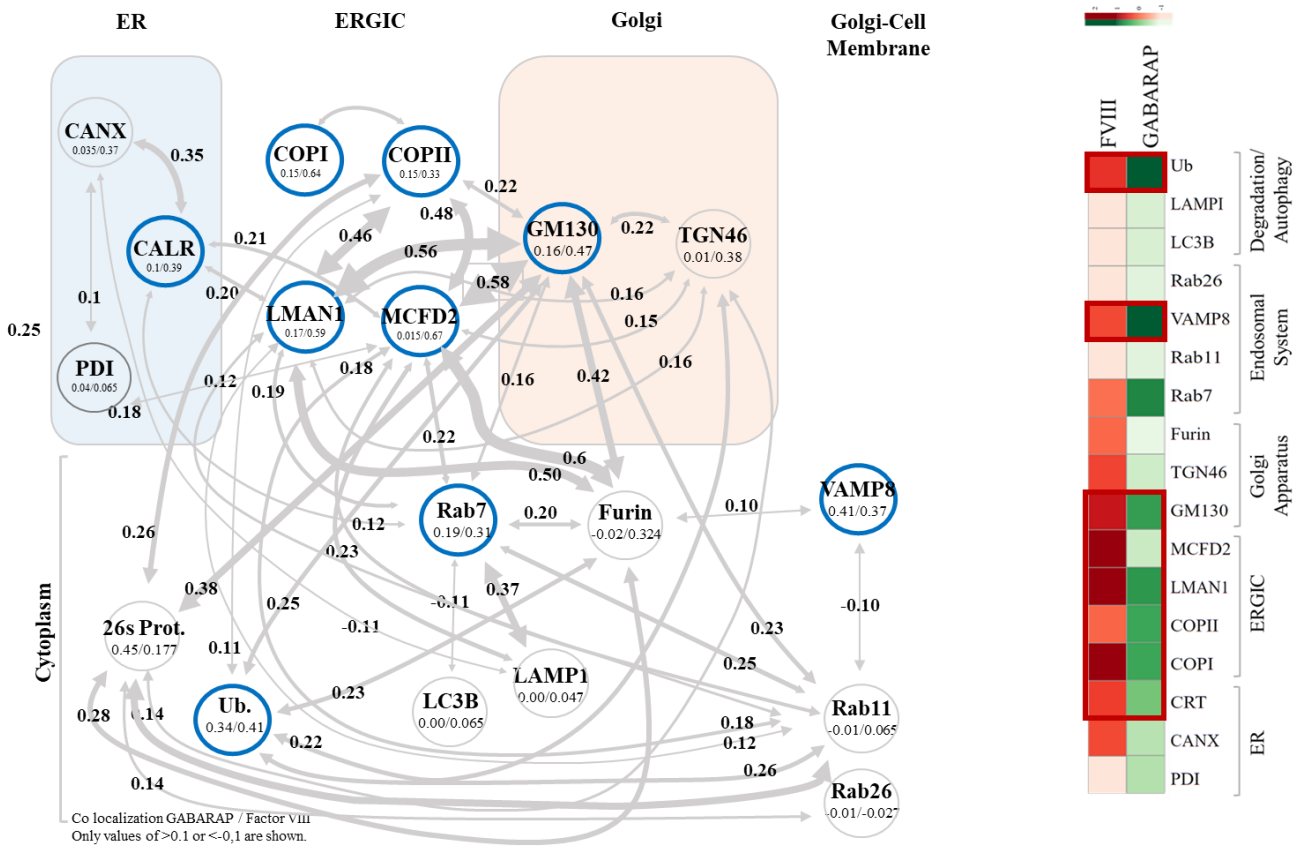

Figure 23. Schematic Representation of Distribution of intracellular proteins/markers in HEK28^{WT} Cells. This figure illustrates the compartmentalization of GABARAP and FVIII within the intracellular environment, showing key cellular compartments: ER, ERGIC, Golgi, cytoplasm, and cytoplasmic vesicles. For each compartment, the first value represents the Pearson's correlation coefficient (PCC) for co-localization of proteins with GABARAP, and the second value represents the PCC for co-localization with FVIII. Arrows indicate the co-localization values between the proteins within the cell. The right heatmap provides an alternative visualization of the co-localization data, with PCC values for FVIII (red) and GABARAP (green) co-localization against intracellular markers.

around the proteasomes. This means GABARAP influenced FVIII presence with the markers where GABARAP was found to localize **(Figure. 24).**

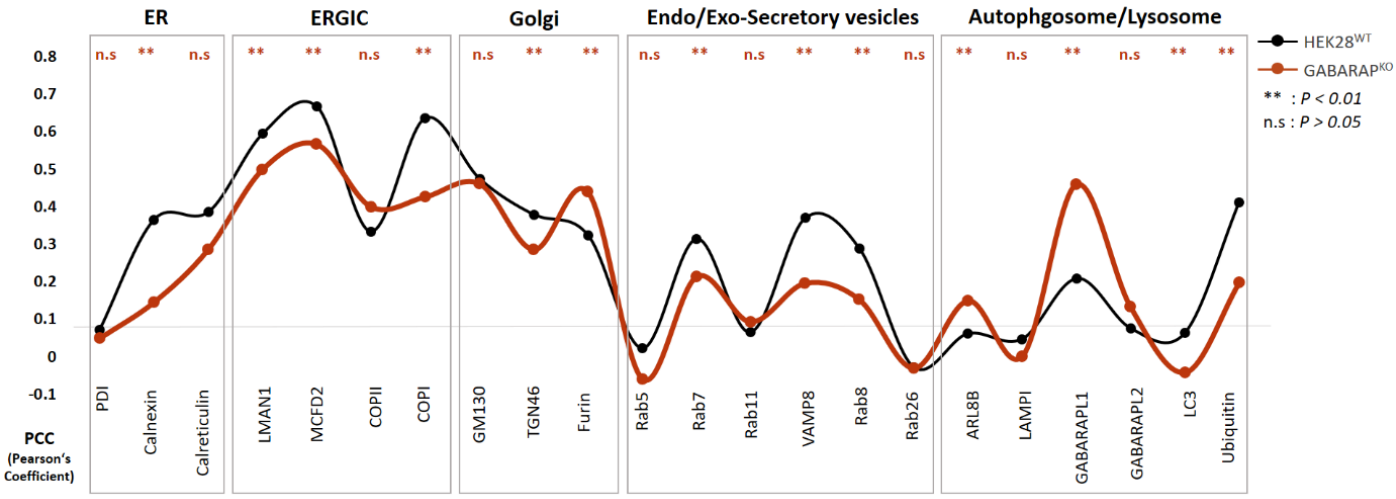

Figure 24. Comparison of FVIII co-localization values using Pearson's Correlation Coefficient (PCCs) in HEK28^{WT} and GABARAP^{KO} cells with 22 intracellular proteins. Curves (black: HEK28^{WT}; orange: GABARAPKO) connecting dots corresponding to PCC values (-1; 1) of FVIII with the different proteins (ER proteins: PDI, Calnexin, Calreticulin; ERGIC: LMAN1, MCFD2, COPII (sec31a), COPI (COPB); Golgi: GM130, TGN46, Furin; Vesicle markers: Rab5, Rab7, Rab11, VAMP8, Rab8, Rab26; Auto. & lysosomal markers: ARL8B, LAMPI, GABARAPL1, GABARAPL2, LC3B; Proteasomal degradation: Ubiquitin). ns: non-significant, p> 0.05; **: p <0.01.

Complementary to this procedure, a variety of intracellular markers were co-stained against each other in order to elucidate the cellular network present in the used HEK cell system **(Figure 23)**. A moderate proximity was observed between Calnexin and Calreticulin (PCC= 0.35), the two ER- chaperones, despite the absence of direct interaction reports in the literature. Their proximity could be due to the fact that while functioning independently, Calnexin and Calreticulin may operate in overlapping spaces within the ER, or at the same time with the same substrate, reflecting coordinated activity in the quality control or folding of proteins.

As anticipated, LMAN1 and MCFD2, showed moderate co-localization with Calreticulin (PCCs of 0.2 for both), a higher co-localization with Sec31a (COPII) (PCCs of 0.46 and 0.48, respectively), and with GM130 (cis-Golgi marker, PCCs of 0.56 and 0.58, respectively). Interestingly, LMAN1 and MCFD2 also co-localized significantly with Furin/PACE, a protein of the trans-Golgi Network (TGN) (PCCs of 0.5 and 0.6,

respectively). Moreover, COPII (Sec31a) vesicles were also found at the Cis-Golgi (GM130) (PCC=0.22), as well as with COPI (COPB) vesicles (PCC=0.21)

Rab7, a marker of late endosomes, showed the highest co-localization with LAMPI (PCC=0.37), a lysosomal marker, and with Rab11 (PCC=0.25), another anticipated outcome. Both Rab7 and Rab11 co-localized with Furin (PCCs of 0.2 and 0.25, respectively). The latter is known to localize at the TGN/endosomal interface [(91)]. Moreover, Rab11, which is typically associated with recycling endosomes, is also present in the late-TGN compartment [(92)]. The latter could serve as an early endosomal compartment which maturate later on into late endosomes, preparing its cargo for further degradation by the lysosomal/ auto-lysosomal system [(92)].

Interestingly, some unexpected co-localization patterns were observed. For example, Rab7 co-localized with LMAN1 (PCC=0.19), MCFD2 (PCC=0.22), and, to a lesser extent, with Calreticulin (PCC=0.12) and GM130 (PCC=0.16), markers of the ERGIC and cis-Golgi compartment, respectively. Additionally, LAMPI, showed unexpected co-localization with MCFD2 (PCC=0.23). LMAN1 and MCFD2 co-localized as well with Rab11 (PCCs of 0.12 and 0.18, respectively), and Rab11 showed an association with GM130 (PCC=0.23), suggesting an interplay between ERGIC, cis-Golgi, and TGN-sorting/endosomal compartments.

Overall, these pattern-connections reinforce the link between the early secretory pathway and sorting endosomal pathways, as evidenced by the co-localization of ERGIC proteins (LMAN1 and MCFD2) with components of the endosomal system, such as Rab7, Rab11 and LAMPI. The strong co-localization of LMAN1 and MCFD2 with Furin, a protein situated at the intersection of the TGN and multiple sorting pathways, further highlights this interplay.

Further detailed connections and expansion of co-markers co-localization are schematically represented in **Figure 23**.

4.6. Deletion of GABARAP Highly Disrupts the Golgi Morphology

To further understand the effect of the GABARAP protein on FVIII in the conventional secretory pathway, knowing that single, double and triple KOs of the GABARAP family

of proteins resulted in apparent alterations of the Golgi morphology [70], tracking of the changes occurring to the Golgi apparatus in HEK28^{WT} and the CRISPR/Cas9-KOs was considered. For this, the Golgi morphology was classified into three distinct categories: **Type I** including the normal compact (crescent) Golgi- shape, **Type II** showing slightly dispersed Golgi stacks and **Type III** exhibiting the highest Golgi-dispersions (punctuate structures), using immunofluorescence staining and imaging of Cis- (GM130) and trans-Golgi (TGN46) networks **(Figure 25. Microscopy images)**.

In comparison to HEK28^{WT} cells, no major alterations in Cis-Golgi morphology (by GM130 staining) were observed across the CRISPR/Cas9-KO cell lines. In nearly all of the KOs, the Type II Golgi morphology remained the dominant phenotype. However, subtle but notable disruptions were detected in the MCFD2^{KO} and GABARAPL2^{KO} cell lines, as indicated by Chi-Square tests yielding p-values of 3.63E-02 and 2.26E-02, respectively. These results suggest a slight shift towards the Type II Golgi morphology in these two knockout cell lines, indicating a potential influence of MCFD2 and GABARAPL2 on the Cis- Golgi structure.

In contrast, more pronounced disruptions were observed in the trans-Golgi network **(by TGN46 staining)** across all cell lines, with the majority of cells displaying a dominant Type III Golgi morphology. Among these, the GABARAP^{KO} showed the most significant change, with a highly significant Chi-Square p-value of 3.89E-50, indicating a considerable deviation from the expected Golgi morphology distribution, particularly with more cells with Type III morphology. **(Figure 25. right panel)**

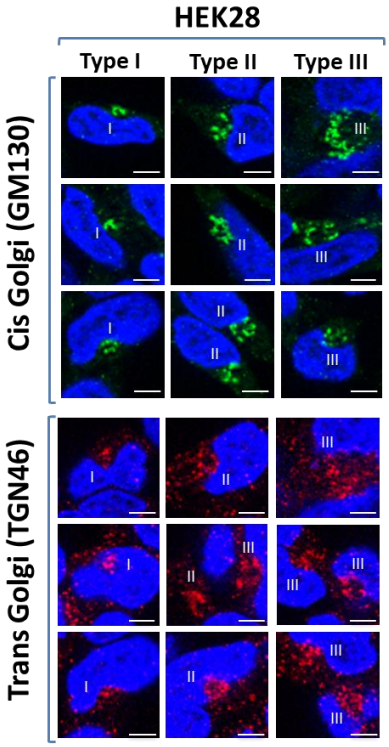

	Type I	Type II	Type III	Chi-test
HEK28	11	73	15	
CANX	17	67	16	2,78E-01
CALR	19	68	12	1,24E-01
LMAN1	17	69	15	3,66E-01
MCFD2	18	73	9	3,63E-02
GABARAP	18	71	11	1,64E-01
GABARAPL1	15	75	10	1,36E-01
GABARAPL2	21	69	10	2,26E-02
ATG7	17	64	19	1,20E-01

	Type I	Type II	Type III	Chi-test
HEK28	10	61	29	
CANX	2	32	66	5,81E-20
CALR	4	39	57	1,07E-08
LMAN1	1	28	71	4,27E-30
MCFD2	1	37	62	8,72E-22
GABARAP	2	14	84	3,89E-50
GABARAPL1	5	20	75	3,72E-26
GABARAPL2	2	31	68	3,37E-21
ATG7	4	38	58	3,68E-09

Figure 25. Absence of the GABARAP protein disorganized the Golgi Morphology in HEK cells. Left panel displays microscopy images of cis- (GM130 marker in green) and trans- (TGN46 marker in red) Golgi stacks in HEK28^{WT}. DAPI (blue) was used for nuclei staining. Graded types I, II and III correspond to intact, semi-dispersed and dispersed/degenerated Golgi morphologies, respectively. Scale Bar 5 µm. Right panel represents ''number of cell'' percentage in each of the three categories type I, type II and type III for HEK28^{WT} and the eight CRISPR/Cas9-KOs. Results of Chi-squared (χ^2) test comparisons to HEK28^{WT} with respect to the corresponding Golgi compartments are also shown.

4.7. Cell (Chemical) Treatments Assessment

4.7.1. Chemical Treatments influenced FVIII secretion and placed GABARAP^{KO} in proximity to CALR^{KO}

Having previously observed that the effects of GABARAP^{KO} on the intracellular redistribution of FVIII were similar to those of CANX^{KO} and CALR^{KO}, specific intracellular pathways were further disrupted towards better understanding of the involvement of the GABARAP protein in FVIII trafficking. To achieve this, four treatment conditions were chosen to be applied to HEK28^{WT}, CANX^{KO}, CALR^{KO}, LMAN1^{KO}, and GABARAP^{KO} cell lines. These cellular treatments involved Glucose starvation, the inhibition of the Rab7 GTPase protein, Brefeldin A and Chloroquine **(Figure 26).**

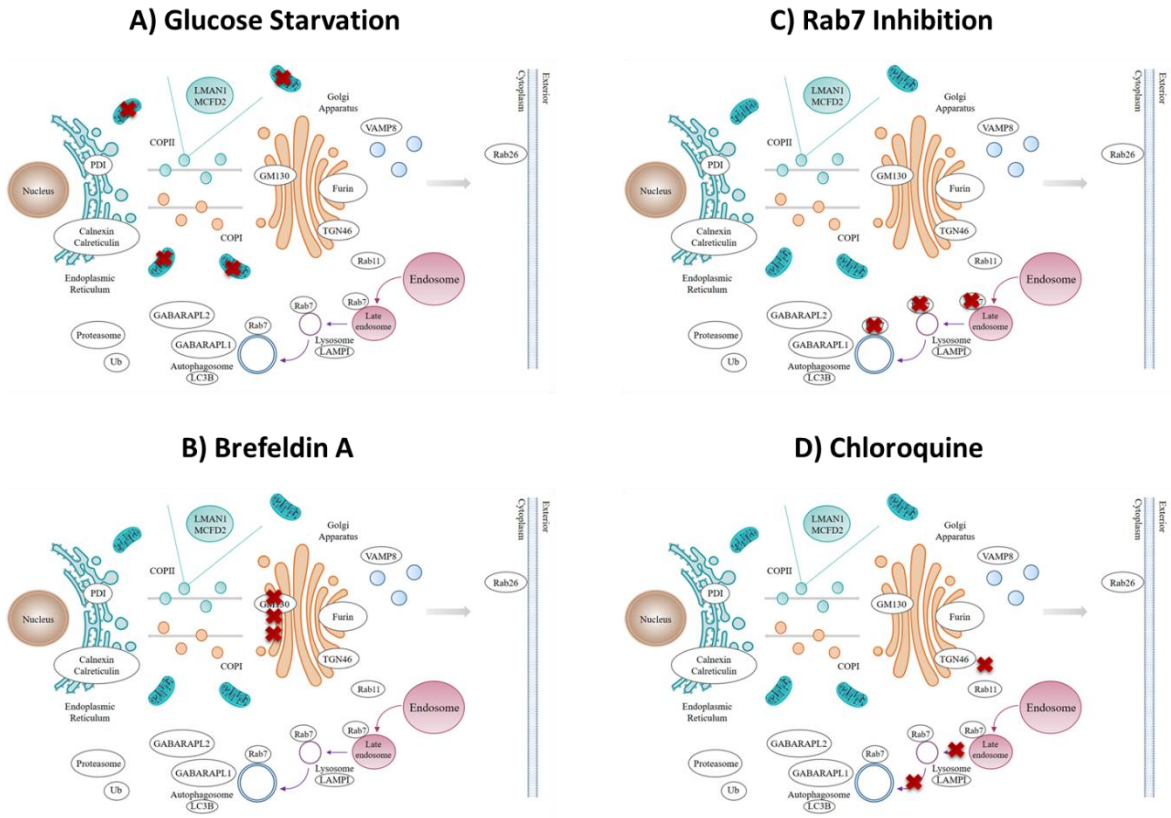

<u>Figure 26.</u> Schematic Representation of the Four Employed Chemical Treatments and Their Effects on Cellular Compartments and Pathways. A) Illustrates glucose starvation, which interferes with metabolic and energetic cellular levels, symbolized by red crosses on the mitochondria. **B)** Shows Brefeldin A treatment, which disrupts vesicular flow in the ERGIC compartment and prevents protein transport to the Golgi apparatus. **C)** Represents Rab7 inhibition, which blocks fusion events between lysosomes and endosomes, as well as the fusion of lysosomes with autophagosomes. **D)** Depicts the effect of chloroquine treatment, which impairs the fusion of autophagosomes with lysosomes, the endosomal system, and the trans-Golgi network.

HEK28^{WT} cells were subjected to starvation conditions by treatment with glucose-deprived media **(Figure 26. A)** for 24–36 hours. Under basal conditions, without any external stimuli (like chloroquine), detecting the LC3B protein (15 kDa) is challenging. This difficulty remained present when the LC3B protein was detected by WB in conditions of amino acid deprivation and in the absence of both glucose and amino acids. However, thicker bands of both LC3B isoforms, LC3B-I and LC3B-II, were much clearer in lysates from cells treated with low-serum and glucose-deprived media. Notably, the band representing the LC3B-II isoform was the most prominent in cells treated with glucose-deprived media. It is important to highlight that the appearance of a thicker LC3B-II band (the lipidated/ PE-conjugated form of the LC3B protein) in conditioned media (glucose deprivation) compared to HEK28^{WT}, indicates a successful activation of the autophagy machinery **(Figure 27 A. upper panel).**

Furthermore, staining of the LAMP1 protein **(Figure 27 A. lower panel)**, a marker of lysosomal vesicles, showed enlarged lysosomal vacuoles in cells treated with glucose-deprived media, suggesting an increase in autophagy processing.

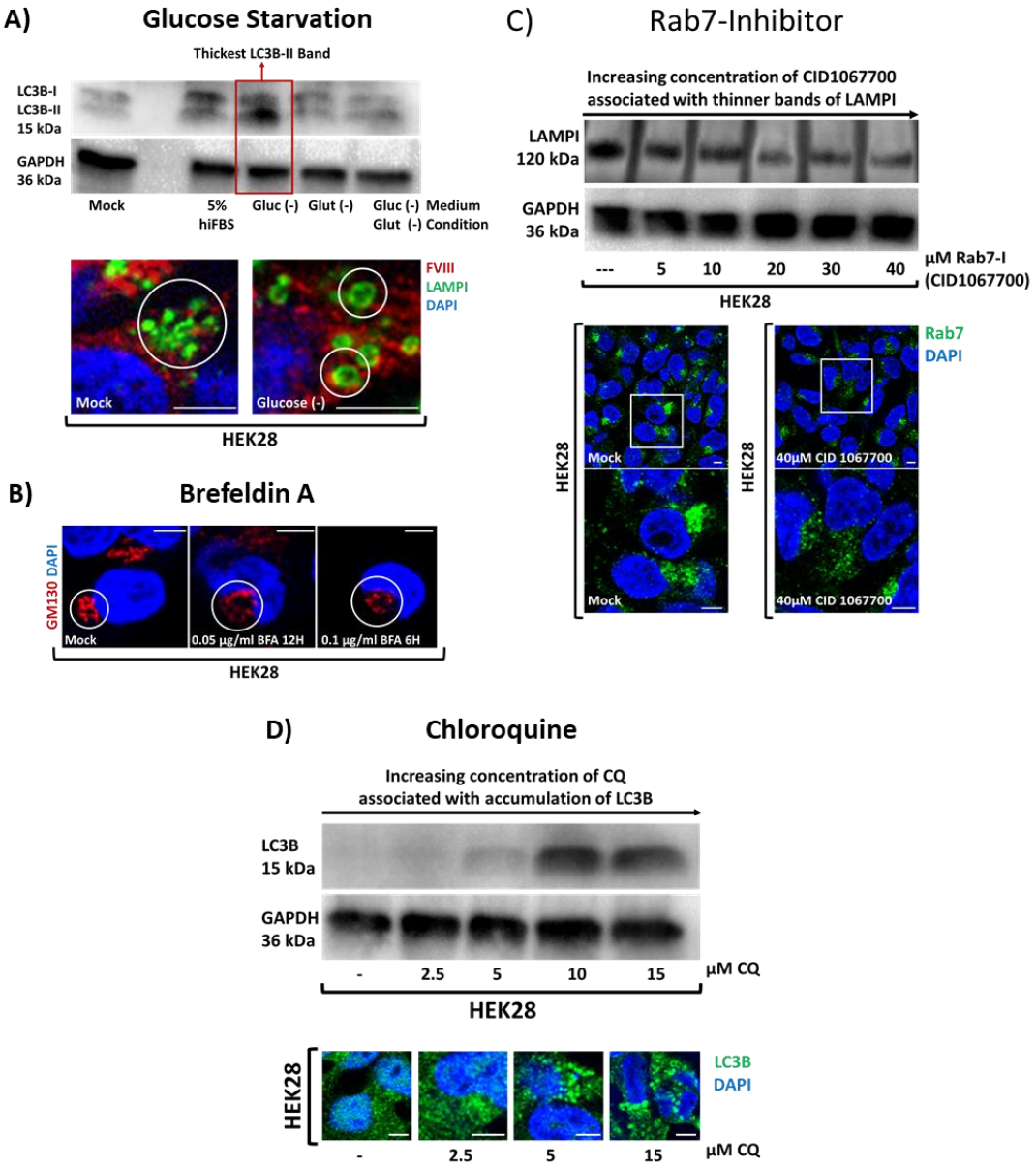

Figure 27. Establishment of Chemical Treatments. A) Glucose Starvation was established by detecting autophagy stimulation selected based on the thickest detected LC3B-II band. A clear variation in the size of lysosomes (bigger vesicles marked by LAMPI in green) was also observed. **B)** Different Brefeldin A concentrations/Time points were tested revealing a disruption of the Golgi morphology marked by the Cis-Golgi marker GM130 (red). **C)** Rab7 Inhibition was accomplished by applying 40µM CID1067700 upon detecting thinner bands of LAMPI with increasing concentrations (5µM to 40µM) of CID1067700. **D)** Increasing concentrations of Chloroquine (CQ) (2.5µM to 15µM) reflected accumulated LC3B. Thicker LC3B bands were also detected by WB and IF-staining (green). Scale Bar for microscopy images is 5µm.

Following this initial procedure, glucose-deprived media were used to treat the single KO-clones. In addition to its role in autophagy activation, the results' interpretations also took into consideration the effect of low-glucose conditions on overall cellular metabolism. Upon glucose deprivation, a significant drop in FVIII secretion was observed across most cell lines, with HEK28^{WT} showing a 48%, CANX^{KO} a 53%, CALR^{KO} a 54%, and GABARAP^{KO} a 48%, reduction in media levels of FVIII. This consistent reduction underscores the critical role of glucose in maintaining normal cellular metabolism and energy levels, which are essential for optimal FVIII production and secretion. In contrast, LMAN1^{KO} cells exhibited a 36% increase in FVIII activity under glucose starvation **(Figure 28. upper left panel);** however the absolute value increase was quite small from about 3 to 5% which is negligible and much below the significance of the system. Nevertheless, this slight increase further correlated with enhanced FVIII co-localization with Golgi markers, specifically GM130 (cis-Golgi) and TGN46 (trans-Golgi), which renders it reportable **(Figure 29. third row 4th graph)**. These findings suggest that in the absence of LMAN1, glucose starvation may trigger compensatory mechanisms that enhance FVIII trafficking in the Golgi apparatus or in direct post-Golgi exocytosis, leading to increased secretion. It could be here speculated that the autophagy machinery may play a role in this process.

In the aim of blocking the normal vesicular flow of the conventional secretory pathway, cells were treated with the antiviral fungal drug Brefeldin A (BFA) **(Figure 26. B)**. BFA functions by stabilizing ARF1 in an inactive GDP-bound state which in turn perturbs the biogenesis of COPI vesicles, affecting consequently the equilibrium of the ERGIC compartment and leading thereby to the disruption of the Golgi morphology [93-95]. Consistent with previous experimental framework, HEK28^{WT} was first treated with BFA concentrations ranging from 1 µg/ml to 10 µg/ml. Media were collected after 30 min, 1 hour, 2 hours, 4 hours, 6 hours and 12 hours. Under these conditions, intracellular staining of the GM130 protein- marker of the Cis-Golgi Network- showed a clear disruption of the Golgi apparatus where its compact structure clearly shifted to a more dispersed and diffuse pattern. However, no detectable FVIII activity was measured extracellularly. The range of tested BFA concentrations was therefore lowered (0.05 µg/ml and 0.1 µg/ml) and the time intervals were increased (16 – 20

hours) prior to media collection. Even with this range of lowered BFA concentrations, a clear disruption of the Golgi morphology in comparison to HEK28^{WT} was well observed **(Figure 27. B).** Upon this, FVIII became successfully detectable in cell media. The rest of the single KO-clones were afterwards treated with 0.05 µg/ml for 20 hours. FVIII secretion was significantly affected following BFA treatment, as expected. Reductions of 61%, 74%, and a complete abolishment of FVIII secretion were observed in HEK28^{WT}, CANX^{KO}, and LMAN1^{KO} cells, respectively. This highlights the substantial impact of BFA on FVIII secretion, particularly in cells with intact or partially disrupted secretory pathways. However, FVIII secretion appeared to be less affected in the absence of CALR and GABARAP proteins. This was reflected by a moderate 32% decrease in FVIII activity in CALR^{KO} cells, and almost no detectable variation (2%) in GABARAP^{KO} cells. These results suggest that CALR and GABARAP proteins confer some resilience to BFA-induced disruption of the FVIII secretion pathway, in contrast to the stronger effects seen in HEK28^{WT}, CANX^{KO}, and LMAN1^{KO} cells. **(Figure 28. lower left panel).** Based on the above, it appears that the effect of GABARAP^{KO} on the decrease in FVIII secretion is linked to GABARAP's role in maintaining the normal morphology of the Golgi apparatus, with Calreticulin also contributing, however to a lesser extent. Therefore, BFA cannot further affect the Golgi, as it is already compromised by the knockouts of Calreticulin and GABARAP.

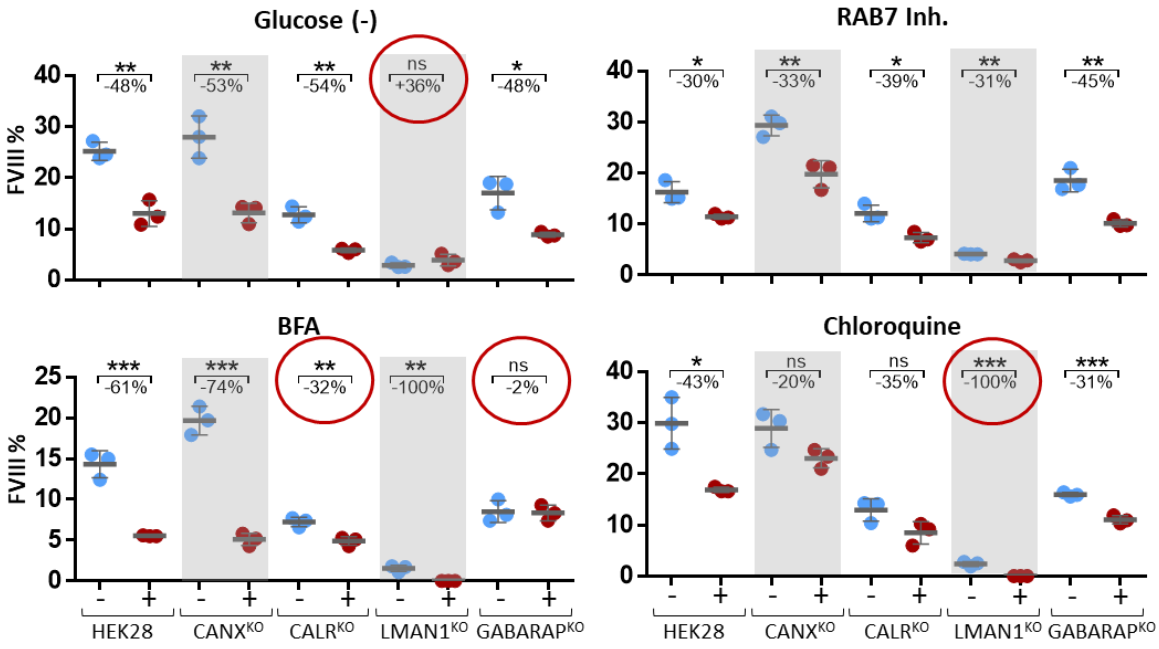

Figure 28. Chemical Treatments place GABARAP^{KO} close to CALR^{KO} in its effect on FVIII secretion. Dot Plot diagrams sowing percentage secreted FVIII activity measurements obtained by two-stage-chromogenic assay (Y axis) in HEK28^{WT} and five CRISPR/Cas9-KO cells plotted on the X axis, in treated (red dots) by glucose starvation, Rab7 inhibition (CID 1067700), Brefeldin A and Chloroquine (CQ), and mock conditions (blue dots) (n.s.: non-significant; *: p <0.05; **: p <0.01; ***: p <0.001; ****: p <0.0001).

Next, an approach to target late endosomes was applied, by competitively inhibiting the GTPase Rab7 using the compound CID 1067700. CID 1067700 exhibits high binding affinity to the guanine nucleotide-binding sites of Rab7 (https://www.axonmedchem.com/product/2184), preventing thereby Rab7 from switching between its GDP- and GTP-bound states. This inhibition disrupts Rab7's normal function, which in turn affects endosomal-lysosomal fusion and trafficking **(Figure 26. C)**.

For these experiments, cells were treated with a range of CID1067700 concentrations, from 5 µM to 40 µM, for 24–36 hours. After treatment, as in previous experiments, cell lysates and media were collected for further analysis. Rab7 inhibition has been previously shown to result in decreased expression of the LAMP1 protein [96]. Based on this, the success of the treatment was validated by monitoring changes in the LAMP1 protein levels in HEK28^{WT} cells. Increasing concentrations of CID 1067700 were accompanied by a progressive decrease in the thickness of the LAMP1 protein band

(observed at 120 kDa), as evidenced by WB analysis **(Figure 27 C. upper panel)**. Additionally, intracellular staining of Rab7 in HEK28^{WT} cells before and after treatment showed increased disruption of late endosomal compartments (dispersed pattern of Rab7), further confirming the effectiveness of the treatment **(Figure 27 C. lower panel)**. Subsequently, additional experiments were conducted using 40 µM CID1067700 to treat the rest of the single KO clones. Decreases in FVIII activity were observed in HEK28^{WT} (30%), CANX^{KO} (33%), CALR^{KO} (39%), LMAN1^{KO} (31%), and GABARAP^{KO} (45%) cells **(Figure 28. upper right panel).**

Finally, chloroquine (CQ) treatment was employed to inhibit the autophagy machinery by blocking the fusion of autophagosomes with lysosomes and, consequently, disrupting the endosomal system **(Figure 26. D)**. Additionally, CQ was used to disrupt the Golgi apparatus and its associated pathways. In the first stage, HEK28^{WT} cells were treated with increasing concentrations of CQ, ranging from 2.5 µM to 50 µM. Notably, cells treated with CQ concentrations above 20 µM were not viable when monitored 24 hours post-treatment, indicating the cytotoxicity of high CQ concentrations on the cells. The concentration range was therefore adjusted to 2.5 µM–15 µM. As shown in **Figure 27. D (upper panel)**, treatment with increasing concentrations of CQ (2.5 µM–15 µM) was positively correlated to the appearance of a progressively thicker LC3B protein band at a MW of 15 kDa detected by WB, a hallmark of autophagy inhibition. The thickest LC3B band was observed at CQ concentrations of 10 µM and 15 µM. This result was consistent with LC3B staining in cells treated with the same CQ concentrations' range (2.5 µM–15 µM). In parallel, microscopic visualization showed an increasing accumulation of LC3B, progressing from a diffuse pattern to the formation of aggregated LC3B puncta **(Figure 27. D, lower panel)**.

Based on these results, and since autophagy appeared to be inhibited at CQ concentrations of 10 µM and 15 µM, 10 µM for the scaled-up experimental setup including the remaining KO-clones was chosen. Chloroquine (CQ) treatment resulted in a general drop in FVIII activity across all treated cells (HEK28^{WT}: 43%, CANX^{KO}: 20%, CALR^{KO} 35% and GABARAP^{KO} 31%), except for LMAN1^{KO}, where FVIII secretion was completely halted **(Figure 28. lower panel right)**.

4.7.2. Co-localization of FVIII with key intra-cellular markers following chemical treatments positions GABARAP^{KO} close to CANX^{KO}

Treatments of HEK28^{WT} and the selected CRISPR/Cas9-KOs cells were as well followed by tracking of FVIII intracellular pattern variation. For this, six proteins were selected: GM130 (Cis-Golgi network), TGN46 (Trans-Golgi network); Rab7 (late endosomes-lysosomes); LAMPI (lysosomes), VAMP8 (endosomal and autophagosomal structures) and LC3B (autophagosomes). Each of these proteins has the potential of guidance into detecting changes at key intracellular landmarks involving the Golgi apparatus (or otherwise classical secretory route), the endosomes, the lysosomes, and the autophagosomes.

Treatment with BFA led to a notable reduction in FVIII secretion across all the tested cell clones. In HEK28^{WT} cells, BFA appeared to have no effect on FVIII within the cis-Golgi (GM130), indicating that FVIII was still able to reach this compartment. However, FVIII displayed increased co-localization with TGN46, Rab7, VAMP8, and LAMP1 following treatment, suggesting enhanced trafficking of FVIII through endosomal sorting pathways **(Figure 29. 1st row (BFA), 1st graph)**. Furthermore, the most significant decrease in FVIII secretion under BFA conditions was observed in CANX^{KO} and LMAN1^{KO} clones. This was accompanied by a marked reduction in FVIII association with GM130 and TGN46 (Golgi-associated proteins) in CANX^{KO} **(Figure 28. Figure 29. 1st row (BFA), 2nd graph, yellow box),** as well as a reduction in the already minimal co-localization of FVIII with LAMP1, the lysosomal marker, in LMAN1^{KO} cells **(Figure 28. Figure 29. 1st row (BFA), 4th graph, yellow box).** In contrast, the lower impact of BFA on FVIII secretion in CALR^{KO} and GABARAP^{KO} cells was mirrored intracellularly by less pronounced disruptions in FVIII trafficking patterns within these KO-clones. This finding emphasizes the roles of GABARAP in maintaining the homeostasis of vesicular flow within the ERGIC compartment **(Figure 28. Figure 29. 1st row (BFA), 3rd and 5th graphs).**

Moreover, disrupting the Rab7 protein by CID 1067700 influenced FVIII localization within the cis-Golgi (increase in HEK28^{WT}**, Figure 29. 2nd row, 1st graph, yellow box**), trans-Golgi compartments (increase in HEK28^{WT} but decrease in CANX^{KO}, LMAN1^{KO}, and GABARAP^{KO}) and VAMP8-related structures (decrease in CANX^{KO}, CALR^{KO}, and

LMAN1^{KO}). Moreover, in CANX^{KO}, FVIII showed increased co-localization with Rab7, suggesting a potential retention in Rab7-positive vesicles under combined Calnexin deletion and Rab7 inhibition **(Figure 29. 2nd row, 2nd graph, yellow box)**. An opposite effect was observed in CALR^{KO} cells **(Figure 29. 2nd row, 3rd graph).** This outcome underscores the importance of the endosomal pathway and reveals a potential link between the early secretory and endosomal pathways during FVIII cellular processing.

Additionally, glucose starvation further increased FVIII trafficking around VAMP8-related structures, particularly in HEK28^{WT} and CANX^{KO} cells **(Figure 29. 3rd row, 1st and 2nd graphs, yellow boxes).** This is consistent with the activation of autophagy under glucose-deprived conditions and the association of VAMP8 with both endo-lysosomal and autophagosomal vesicles. Another strikingly notable observation was the positive correlation between increased FVIII secretion levels and increased FVIII presence in the Golgi apparatus (GM130/TGN46) as well as its co-localization with LAMP1 and Rab7 (markers of late endosomes-lysosomes) in glucose-deprived LMAN1^{KO} cells **(Figure 29. 3rd row, 4th graph yellow boxes)**. Also, glucose deprivation in GABARAP^{KO}, CANX^{KO}, and CALR^{KO} cells decreased FVIII co-localization with the cis- and trans-Golgi compartments and caused minor alterations in FVIII trafficking around Rab7 **(Figure 29. 3rd row 4th graph 2nd, 3rd and 5th graphs)**.

Chloroquine (CQ), which reduced FVIII secretion across all cell lines, significantly impacted FVIII co-localization with nearly all examined compartments. In LMAN1^{KO} cells, CQ eliminated residual FVIII accumulation in the media, with no FVIII detected in the Golgi apparatus or LAMP1-positive lysosomal vesicles **(Figure 29. 4th row 4th graph)**. This striking correlation between FVIII secretion levels/co-localization with Golgi and lysosomal proteins was remarkably paralleled upon CQ and BFA treatments as well as glucose starvation conditions. In addition, In GABARAP^{KO} cells, CQ notably disrupted FVIII co-localization with Rab7, meanwhile, in CALRKO cells, it increased FVIII co-localization with VAMP8 **(Figure 29. 4th row 3rd and 5th graphs, respectively)**. Collectively, these results indicate that CQ interferes not only with the fusion dynamics of autophagosomes and lysosomes but also with vesicle fusion mechanisms in the Golgi and endosomal compartments, aligning with its documented roles in the literature.

Upon individually visualizing and analyzing the data, and considering the three parameters: cell line, treatment, and protein marker, it became challenging to interpret the results. Therefore, the differences of the average Pearson's Correlation Coefficients between treated and untreated cells were used to generate 3D principal component analysis (PCA) and Heat Map plots. The redistribution of FVIII after treatments in the KO clones revealed, once more, a proximity between $GABARAP^{KO}$ and $CANX^{KO}$. When examining the clustering of variables (markers' distribution) following treatments, close proximity between the protein markers affected by chloroquine treatment and glucose starvation (visualized as blue and red spheres, respectively) was observed. On the other hand, a clear close clustering tendency of markers influenced by both Rab7 inhibition and BFA supplementation was noted (marked as green and grey spheres, respectively). **(Figure 29. B)**

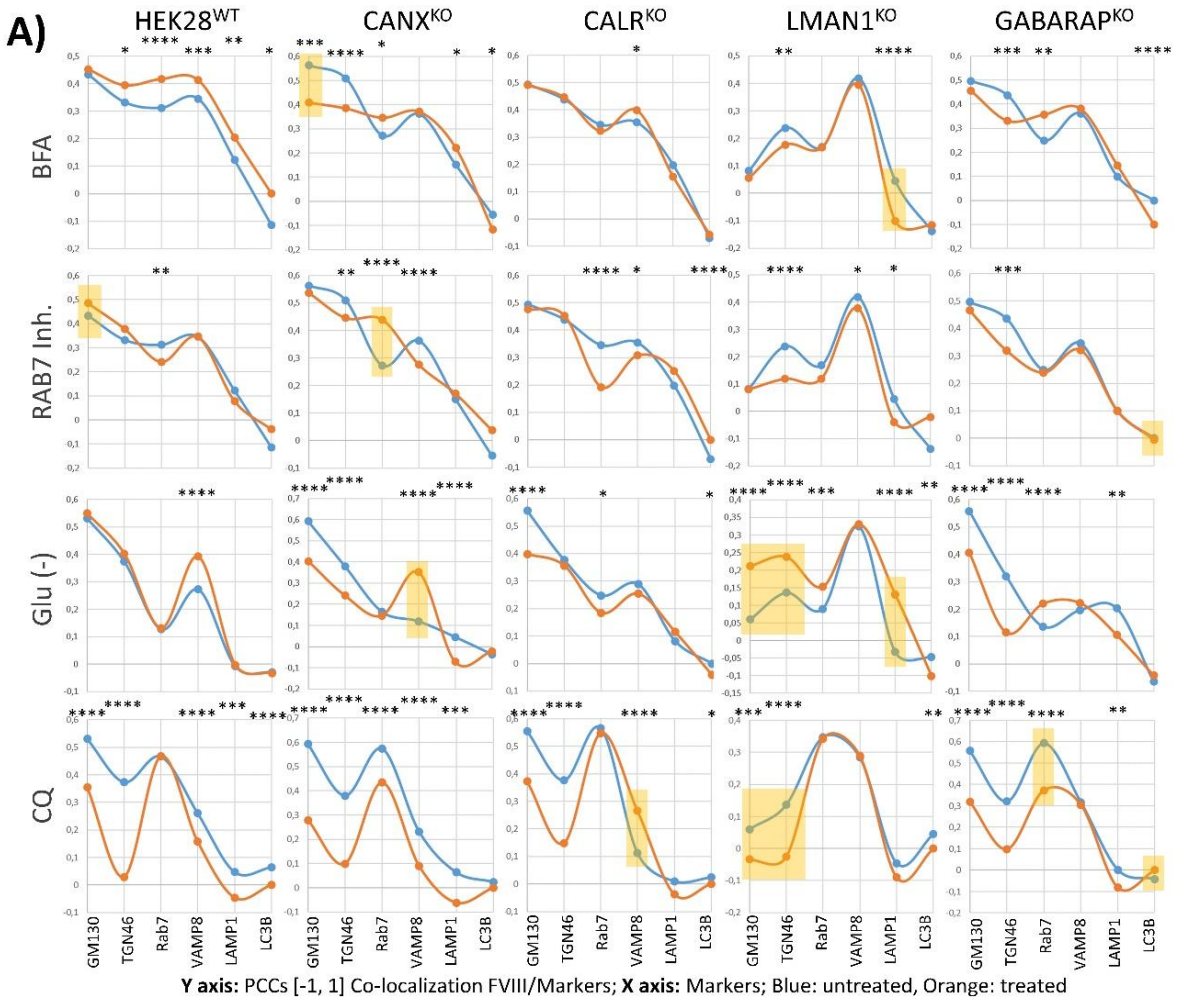
A)
HEK28WT
CANXKO
CALRKO
LMAN1KO
GABARAPKO
BFA
RAB7 Inh.
Glu (-)
CQ
GM130
TGN46
Rab7
VAMP8
LAMP1
LC3B
Y axis: PCCs [-1, 1] Co-localization FVIII/Markers; X axis: Markers; Blue: untreated, Orange: treated

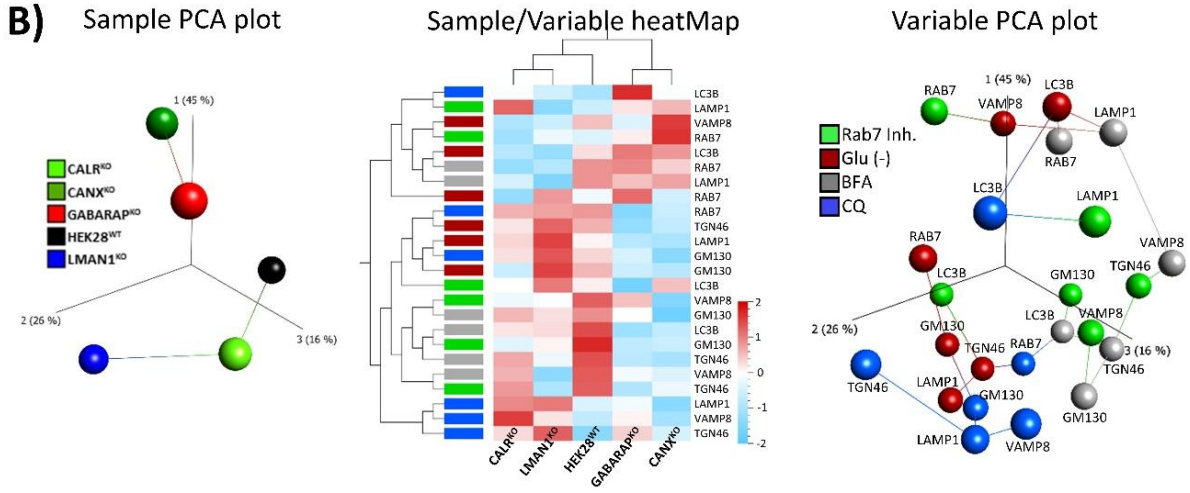
B)
Sample PCA plot
Sample/Variable heatMap
Variable PCA plot
CALRKO
CANXKO
GABARAPKO
HEK28WT
LMAN1KO
1 (45 %)
2 (26 %)
3 (16 %)
Rab7 Inh.
Glu (-)
BFA
CQ

Figure 29. Co-localization of FVIII with key intra-cellular markers following chemical treatments positions GABARAP^{KO} close to CANX^{KO}. A) Curve plots representing PCC [-1, 1] values of FVIII co-localization (X axis) with six intracellular markers (Y axis: GM130, TGN46, Rab7, VAMP8, LAMPI and LC3B), in HEK28^{WT} and CRISPR/Cas9- KOs, under normal (blue curves) and treated (glucose starvation, Rab7 Inhibitions CID 1067700, Brefeldin A, Chloroquine) conditions (orange curves). (*: p <0.05; **: p <0.01; ***: p <0.001; ****: p <0.0001). Significant differences are marked in yellow. B) Multi-angled Visualization of the same Data set (after subtraction to mock PCC values) using 3D unsupervised Principal Component Analysis (PCA) plots and a Heat Map Matrix showing clustering of samples (left) and variables (right) of cellular responses to chemical treatments in HEK28^{WT} and CRISPR/Cas9-KOs and a combination of both in the middle heat map matrix. The color scale in middle heat map ranges from -2 (blue-negative correlations), to 2 (red-positive correlations). Values close to 0 (white) indicate no correlation. Each square in the Heat map represents a PCC score.

4.8. Generation of GABARAP^{KO}/CANX^{KO}, CANX^{KO}/LMAN1^{KO} and CANX^{KO}/GABARAPL1^{KO}

4.8.1. Verification of Transfection and Generation of Single Cells

CANX^{KO} cells were transfected with CRISPR/Cas9-KO vectors targeting LMAN1, GABARAP, and GABARAPL1. Following the transfection with in-house designed and prepared CRISPR/Cas9-KO vectors, lysates were collected 48 hours post-transfection. DNA was extracted and amplified **(Figure 30. A, WT un-transfected:** lanes 1, 4, and 8, **Transfected**: lanes 2, 5 and7, **Positive control**: 3, 6 and 9, and **negative controls**: LW1 and LW2, where *GABARAP-Ex1*, *LMAN1-Ex1*, and *GABARAPL1-Ex2* were amplified, respectively) using a gene- specific set of forward and reverse primers.

The DNA product was then digested by cleavage assay, and mismatches were monitored to confirm transfection and targeting efficiencies. During this step, T7 endonuclease I detects non-complementary hybridized DNA strands that occur as a result of mutations such as deletions, insertions, and point mutations, based on structure-specific recognition of the DNA **(Figure 30. B)**. The visualized outcome, using gel electrophoresis shows that **wild-type** samples (un-edited genome) exhibit a single DNA band which was not cleaved by T7 endonuclease I **(Figure 30. B**, lanes 1, 3 and 7 for amplified *GABARAP-Ex1*, *LMAN1-Ex1*, and *GABARAPL2-Ex2*, respectively). In

contrast, successfully **transfected** samples display two additional smaller bands that, when summed, equal the size of the uncut band **(Figure 30. B**, Lanes 2, 4, and 6 for **muted** *GABARAP-Ex1*, *LMAN1-Ex1* and *GABARAPL1-Ex2*, respectively, in addition to Lanes 5 and 8, **the positive controls**). The intensity of the latter bands indicates the efficiency of the transfection. These bands were observed when *GABARAP-Ex1* **(Figure 30. B, lane 2)** and *GABARAPL1-Ex2* **(Figure 30. B, Lane 6)** were amplified in corresponding transfected cells, however, for *LMAN1-Ex1* only a single additional smaller fainter band was detected alongside un-cleaved (un-edited) DNA, in transfected cells **(Figure 30. B lane 4).** The positive control provided by the commercial kit showed clear cleavage and resulted in three distinct bands corresponding to the uncut DNA and 2 of the edited DNA **(Figure 30. B Lanes 5 and 8)**.

A)

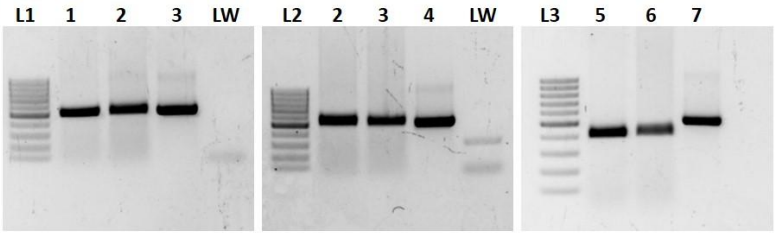

B)

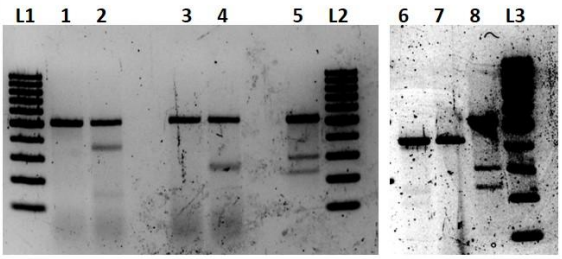

C)

PCR Amplification GABARAP-Exon1/ Picked single-cell clones

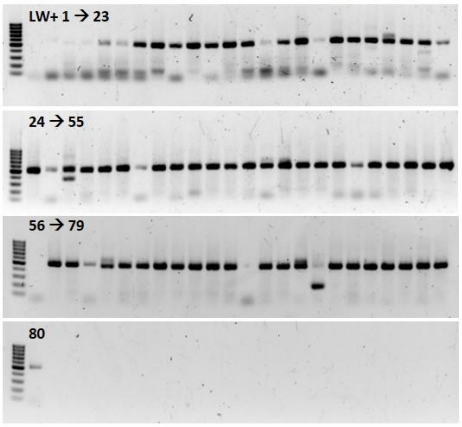

PCR Amplification LMAN1-Exon1/ Picked single-cell clones

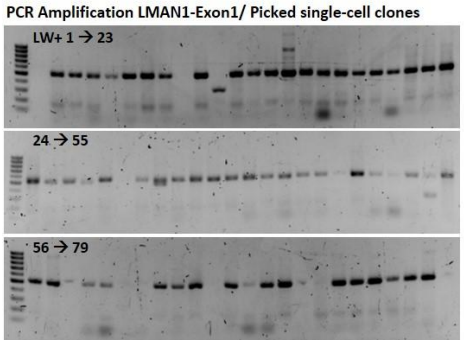

PCR Amplification GABARAPL1-Exon2/ Picked single-cell clones

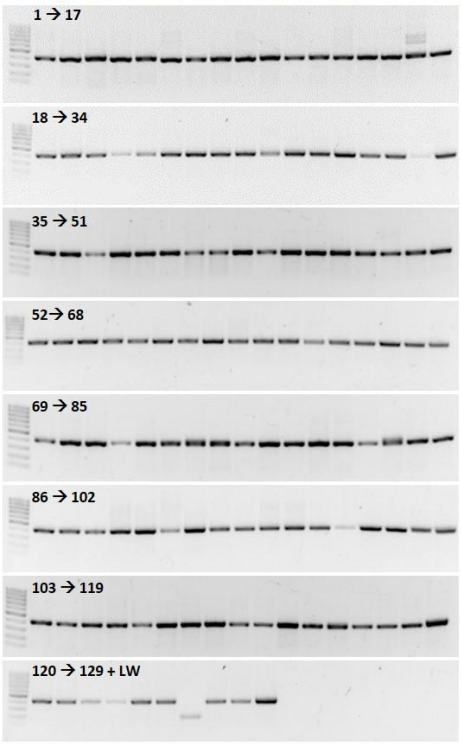

Figure 30. Genomic Validation of CRISPR/Cas9 Knockouts by T7 Endonuclease Cleavage Assay and Gene Amplification after Single-Cell Generation of GABARAP, LMAN1, and GABARAPL1 Knockouts. A) Gene amplification by PCR followed by gel electrophoresis using specific forward and reverse primers for *GABARAP-Ex1*, *LMAN1-Ex1*, and *GABARAPL1-Ex2*. Lanes 1, 4, and 8 represent un-transfected wild-type cell DNA for the three genes respectively, while lanes 2, 5, and 7 show DNA from transfected cells with corresponding CRISPR/Cas9 knockout vectors targeting the three genes (in the same order). Lanes 3, 6, and 9 are positive controls for the cleavage assay, and lanes LW1 and LW2 serve as negative controls (no DNA lysate). **B)** Cleavage assay showing transfected samples display two smaller bands, the sum of which equals the size of the uncut (un-mutated) DNA band. For *GABARAP-Ex1* and *GABARAPL1-Ex2* (lanes 2 and 6), two bands were detected, while for *LMAN1-Ex1* (lane 4), only a single fainter band was observed alongside uncut DNA. Positive controls (lanes 5 and 8) show clear cleavage, with three distinct bands corresponding to the uncut and two edited DNA fragments**. C)** Amplified DNA of the three genes in modified cell populations.

Upon confirming successful transfections, modified cell populations were further seeded after undergoing several dilutions onto 96 well plates to obtain one cell per well. Cells were subsequently expanded, duplicated and further lysed. DNA was extracted and further amplified **(Details in Figure 30. C).** PCR products visualized by gel electrophoresis were further sequenced using gene specific set of primers and analyzed using *Geneious* **(Figure 31).** Based on the sequencing results, type of mutations were defined for selected clones, selected clones were further expanded and subsequently verified using Western blotting (WB), and immunofluorescence (IF) staining and checked for complete protein-KOs. Gene nomenclatures were assigned to indicate specific mutations. WB and IF staining confirmed the complete absence of target proteins in clones to be used for further analysis (including existing and newly generated double CRISPR/Cas9-KOs) **(Figure 31).**

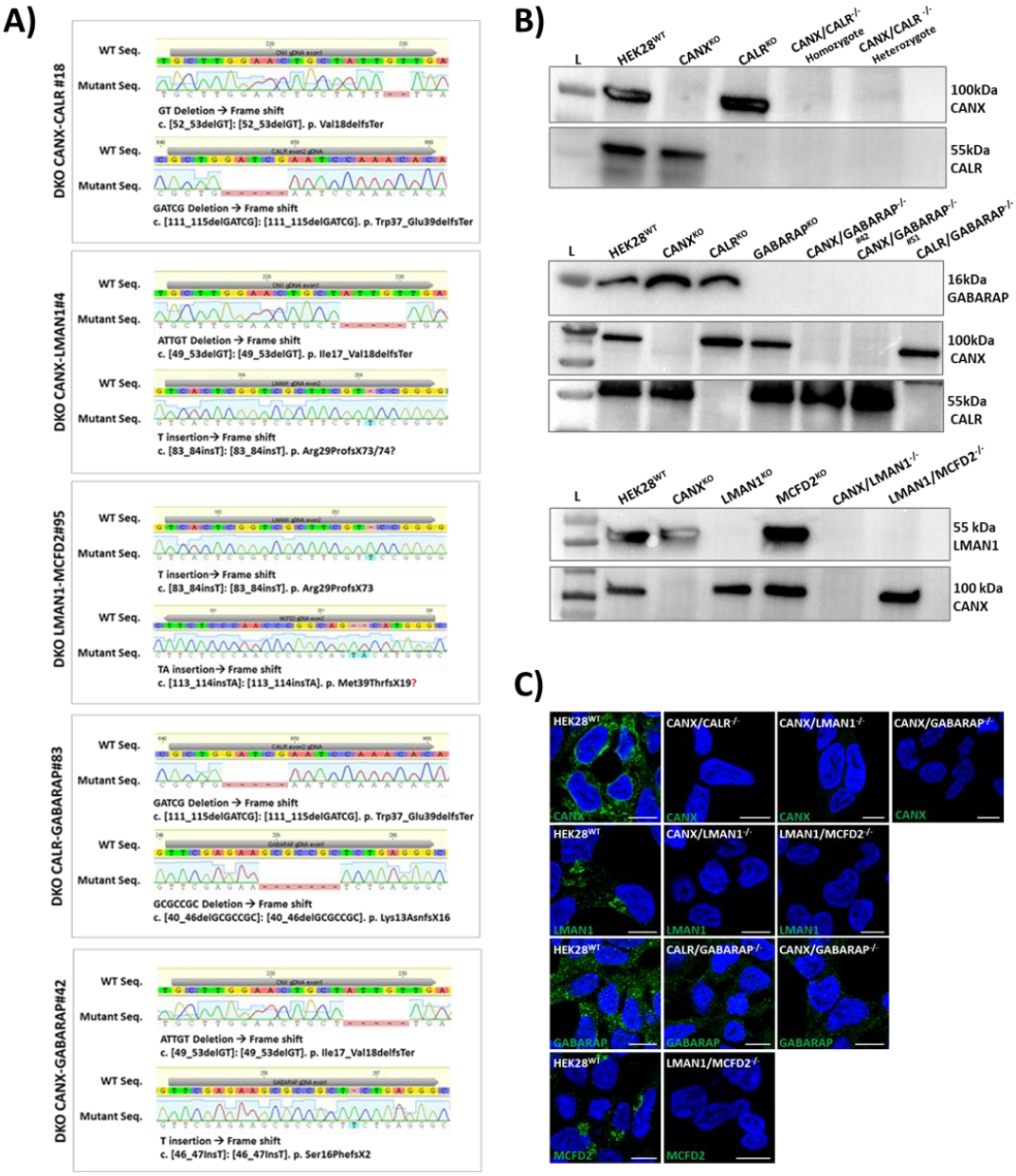

<u>Figure 31</u>. Validation of CRISPR/Cas9-Mediated Double Knockouts. (A) Representative DNA sequence chromatograms from Geneious software confirming the presence and type of mutations, along with corresponding nomenclature, for each double knockout (DKO) combination, compared to the WT unmutated clone. **(B)** Western blot analysis of cell lysates demonstrating the complete loss of target proteins in knockout cells, validating successful gene disruption, with WT clones serving as controls. **(C)** Immunofluorescence (IF) - staining of 4% paraformaldehyde-fixed cells, further illustrating protein loss. Proteins of interest are visualized in green, while nuclei are stained with DAPI (blue). Scale bar: 10 µm.

4.8.2. Analysis of FVIII Secretion, FVIII Co-localization with Intracellular markers, and residual ATP content in the CRISPR/Cas9 KO clones

Following the development and characterization of double CRISPR/Cas9 knockouts targeting FVIII-associated chaperones—CANX, CALR, LMAN1, and MCFD2—as well as GABARAP **(Figure 32)**, FVIII secretion levels were evaluated using a two-stage chromogenic assay both before and after the genetic rescue of the knocked-out proteins. The secretion and rescue patterns varied across the different DKO combinations compared to their respective single knockouts. (Note: For reference $HEK28^{WT}$ FVIII Activity: 26.3%; ATP concentration: 1.24 µM). The following observations were noted:

$CANX^{KO}$/$CALR^{KO}$: In line with previous findings, $CANX^{KO}$ led to an increase in FVIII secretion, whereas $CALR^{KO}$ caused a reduction compared to $HEK28^{WT}$ **(Figure 32)**. The combined knockout ($CANX^{KO}$/$CALR^{KO}$) resulted in an overall decrease in secretion, indicating an additive effect where the opposing influences of the single knockouts converged to reduce FVIII secretion. Rescue experiments showed that re-introducing CANX reduced secretion, while CALR restoration significantly enhanced it. Simultaneous rescue of both CANX and CALR in the DKO setting led to only a slight improvement in secretion, suggesting limited recovery. Intracellular FVIII tracking in the DKO revealed differences compared to the respective single knockouts. Particularly, FVIII was more present in the DKO with endosomal and post-Golgi vesicle markers Rab11 and Rab8a, respectively, when compared to the single-KOs. Additionally, ATP measurements showed residual ATP levels in $CANX^{KO}$ (1.25 µM) and lower levels in $CALR^{KO}$ (1.17 µM) and $CANX^{KO}$/$CALR^{KO}$ (1.08 µM), suggesting a link between FVIII secretion efficiency and cellular energy status **(Figure 32)**.

$CANX^{KO}$/$LMAN1^{KO}$: While $CANX^{KO}$ enhanced FVIII secretion, $LMAN1^{KO}$ resulted in a decrease **(Figure 32).** In $CANX^{KO}$/$LMAN1^{KO}$, FVIII secretion was primarily impacted by LMAN1 loss, leading to a substantial reduction similar to the $LMAN1^{KO}$ phenotype. This was associated with reduced FVIII presence at the Golgi (GM130 and TGN46), reinforcing LMAN1's critical role in ER-Golgi transport. Intracellular FVIII localization shifted toward the $CANX^{KO}$ phenotype with Rab7 and the $LMAN1^{KO}$ phenotype with VAMP8. Despite the additive effect of the DKO, the phenotype largely resembled that

of LMAN1^{KO} due to its greater impact on FVIII intracellular trafficking. Rescue of CANX and LMAN1 in their respective single knockouts, as well as double rescue in the DKO, successfully restored FVIII secretion. ATP levels were higher in CANX^{KO} (1.25 µM) compared to LMAN1^{KO} (1.18 µM) and the DKO (1.18 µM), aligning with the observed FVIII secretion profiles **(Figure 32).**

LMAN1^{KO}/MCFD2^{KO}: Both LMAN1^{KO} and MCFD2^{KO} led to decreased FVIII secretion and impaired FVIII co-localization with Sec31a (COPII vesicles), TGN46 (Golgi), and Rab7 (late endosomes). Interestingly, LMAN1^{KO}/MCFD2^{KO} exhibited a distinct phenotype. Despite reduced secretion, FVIII levels remained higher than in either single knockout. ATP levels followed a similar pattern, with the DKO displaying higher levels (1.46 µM) compared to LMAN1^{KO} (1.18 µM) and MCFD2^{KO} (1.14 µM). This suggests a positive epistasis effect of the dual mutation/deletion of ERGIC cargo-receptor complex proteins. Rescue experiments restored FVIII secretion in both single knockouts, with a stronger effect in MCFD2^{KO}. However, simultaneous rescue of LMAN1 and MCFD2 yielded only minimal improvement. Co-localization patterns varied; FVIII presence in COPII vesicles (Sec31a) was higher than in single knockouts, while GM130-associated localization in the DKO mirrored LMAN1^{KO}. Co-localization with TGN46 was more prominent than in either single knockout, and Rab8a association was relatively high, resembling the MCFD2^{KO} phenotype **(Figure 32).**

GABARAP and ER Chaperones DKOs: Rescue experiments demonstrated that while restoring CANX or CALR in their respective single knockouts successfully restored FVIII secretion, overexpressing GABARAP in GABARAP-deficient cells unexpectedly reduced FVIII secretion. In contrast, double rescue of CALR^{KO}/GABARAP^{KO} and CANX^{KO}/GABARAP^{KO} restored FVIII secretion—decreasing it in CANX^{KO}/GABARAP^{KO} (which initially exhibited elevated secretion compared to HEK28^{WT} and CANX^{KO}) and increasing it in CALR^{KO}/GABARAP^{KO} (which displayed lower secretion than HEK28^{WT}). This suggests a synergistic effect in CANX^{KO}/GABARAP^{KO} and a slightly additive effect in CALR^{KO}/GABARAP^{KO}. Notably, the secretion profiles in both DKOs closely mirrored the effects of CALR or CANX single knockouts, implying that the loss of either ER chaperones dominated over GABARAP's impact on FVIII secretion. The synergistic effect in CANX^{KO}/GABARAP^{KO} was evident through enhanced co-localization of FVIII

with Rab8a vesicle markers compared to their single knockouts. In CALR/^{KO}GABARAP^{KO}, despite reduced FVIII secretion, intracellular FVIII was more strongly associated with Rab11, Rab5, and Rab8a. ATP levels were higher in CANX^{KO} and lower in both CALR^{KO} and GABARAP^{KO}. However, in DKO combinations, no significant correlation was observed between FVIII secretion and ATP levels **(Figure 32).**

Finally, integrating the co-localization analysis and average PCC values into a PCA plot showed that, similarly to CANX^{KO}, CALR^{KO} and GABARAP$^{KO\ that}$ clustered together slightly further from the group containing LMAN1^{KO} and MCFD2^{KO} **(Figure 21),** DKO combinations involving deletions of CANX, GABARAP, and CALR formed a distinct cluster, separate from the CANX^{KO}/LMAN1^{KO} and LMAN1^{KO}/MCFD2^{KO} groups **(Figure 33).**

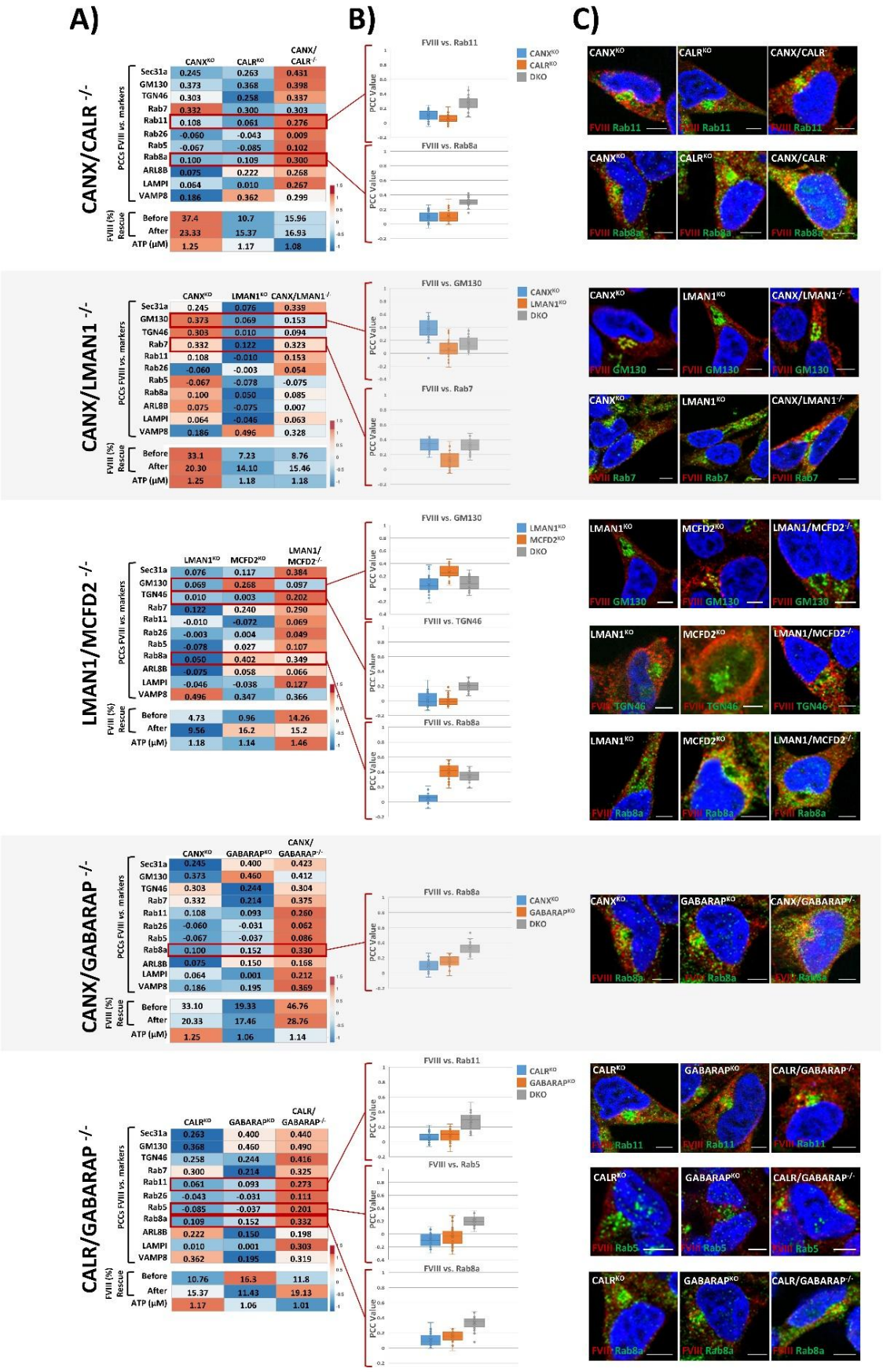
A)
B)
C)
CANX/CALR -/-
CANX/LMAN1 -/-
LMAN1/MCFD2 -/-
CANX/GABARAP -/-
CALR/GABARAP -/-
PCCs FVIII vs. markers
FVIII (%) Rescue
ATP (μM)
Before
After
FVIII vs. Rab11
FVIII vs. Rab8a
FVIII vs. GM130
FVIII vs. Rab7
FVIII vs. TGN46
FVIII vs. Rab5
PCC Value
DKO

Figure 32. Double Knockouts of ER / ERGIC Chaperones and GABARAP uncover differential Effects on Secretion and Trafficking profiles of FVIII. A) Heatmaps of FVIII co-localization with intracellular markers (Sec31a, GM130, TGN46, Rab5, Rab7, Rab8a, Rab11, Rab26, ARL8B, LAMP1, and VAMP8), quantified using Pearson Correlation Coefficient (PCC) values [-1, 1], measurements of FVIII secretion (residual FVIII activity in the media) assessed via a two-stage chromogenic assay before and after genetic rescue (%), as well as residual ATP concentrations (µM) determined using a luciferase-based assay. B) Boxplots comparing PCC values (Y axis: [-1, 1]) between single knockouts (SKOs) and their corresponding double knockouts (DKOs), highlighting markers with the most pronounced differences. C) Representative microscopy images of intracellular markers with the most significant changes between DKOs and their respective SKOs. FVIII is shown in red, intracellular markers in green, and nuclei (DAPI staining) in blue. Scale bar: 5 µM.

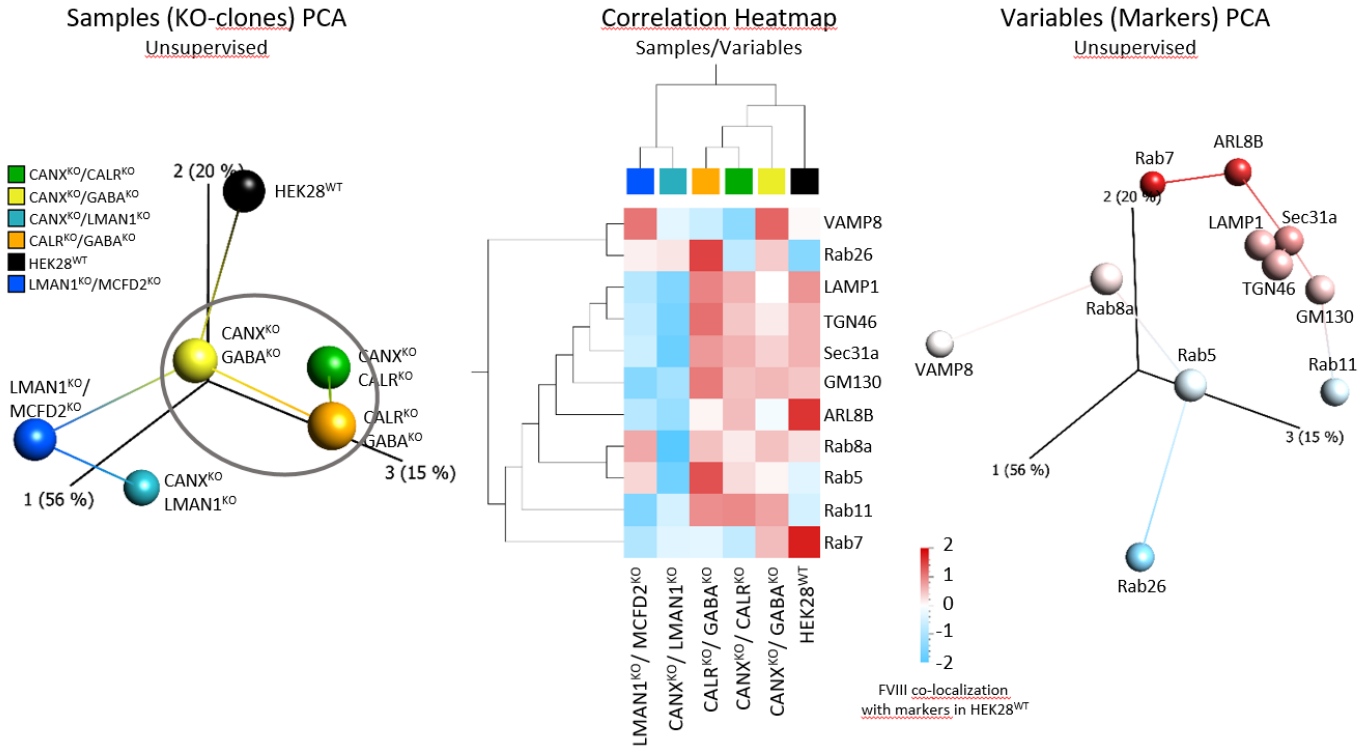

Figure 33. Clustering Analysis of FVIII Co-localization with 11 Intracellular Markers brings GABARAP-, CANX^{-} and CALR –DKO combinations once more *''Together''*. Multi-angled visualization (unsupervised 3D-Principal Component Analysis (PCA) plots and Heat map matrix) of average FVIII co-localization values (PCCs) with 11 intracellular markers in five CRISPR/Cas9 double knockout combinations and HEK28^{WT} (designated by a color code left). Left, 3D-PCA plot of sample (cell lines) and right, of variables (intracellular markers) clustering. Middle, Heatmap visualization combining both samples' and variables' PCA plots. The color scale ranges from -2 (blue-negative correlations), to 2 (red-positive correlations). Values close to 0 (white) indicate no correlation. Each square in the Heat map represents a PCC score.

5. Chapter 5: Discussion

5.1. The Rationale behind Investigating the Intracellular Life of FVIII

''Blood Coagulation'' and ''Wound Healing'' have been topics of interest and targets for new discoveries since the dawn of times. Over the years, scientists have gradually deciphered the biological and medical mechanisms which explain both injury and wound healing events, including their triggers, how they originate, as well as additional downstream related processes. Toward this end, a cascade of proteins capable of activating one another to achieve the ultimate goal of blood clot formation and injury closure, known as the "Blood Coagulation Cascade", was thoroughly investigated and uncovered [3-9, 18].

Among those proteins, FVIII shone to be a crucial component of the intrinsic coagulation pathway, playing an important role in the activation of FX, when collaborating with FIX, which subsequently stimulates thrombin generation and in turn fibrin clot formation and amplification [3, 8, 10]. Defects or loss of proteins within the coagulation cascade have been reported to give rise to pathophysiological conditions and blood-related diseases [11, 12]. Specifically, disruptions in the levels of FVIII in the bloodstream have been attributed to the disease known as Hemophilia A, an X-linked recessive bleeding disorder that primarily affects 1 in 5 000 to 1 in 10 000 males [11, 12, 24, 26]. In the course of attempts to improve treatments for Hemophilia A, FVIII has been the focus of extensive research. Treatment regimens for HA have evolved to include Protein Replacement Therapies (PRT), the administration of by-passing agents like FVIIa, strategies to stabilize and extend the half-life of recombinant FVIII products, reaching developments in gene therapy trials which have gained great momentum [13, 16, 21]. Despite the success achieved for Hemophilia B, gene therapy for Hemophilia A and the delivery of the FVIII-gene by the aid of AAV vectors (Adeno-associated- viral vectors) remain to encounter challenges. These included difficulties in integrating the large full-length FVIII gene in the vectors. This has led to the need of delivering a truncated form of the protein: the B-Domain Deleted-FVIII, with which results remained non satisfactory exhibiting lower and unstable FVIII expression over time,

when compared to FIX [22, 23]. This low secretion levels of FVIII also continued to appear in recombinant systems due to the low levels of FVIII mRNA (expression) as well as FVIII inefficient trafficking from the endoplasmic reticulum to the Golgi apparatus given the capacity of FVIII to aggregate in the ER [24, 25, 34, 50]. In order to address those challenges, researchers have approached the issue from various angles [97]. Efforts have been made first on a genetic level to optimize the codon sequence of the *F8* gene to achieve higher expression levels [97]. Other focusses were directed onto manipulating the bio-engineering of the FVIII protein product for enhanced specific activity and stability in the blood. This was achieved through addition of e.g. polyethylene glycol (PEG) moieties (PEGylating) or other protein fragments such as the Fc component of IgG1 or albumin [13, 97]. One specific branch in improving HA treatment included maneuvering the **secretory pathway of FVIII** by playing its **interactions** and **binding to ER- Chaperones** e.g. with immunoglobulin-binding protein (BiP) and Calnexin/Calreticulin (Mutation F309S in the A1-domain; Replacing the A1-domain of FVIII with the A1-domain of FV…etc.), in the aim of elevating the secretion yield of the protein [33, 97, 98]. In this regard, also some so-called ''Chemical Chaperones'' or ''Pharmacological Chaperones'' were employed and their effects on FVIII secretion was monitored. It was shown that administration of chemical chaperones like Betaine improved FVIII secretion as well as the efficiency of FVIII trafficking by increasing solubility of the FVIII protein and its further transport intracellularly [99].

The latter executed efforts highlight the importance of investigating the intracellular interactions and mechanisms which govern FVIII trafficking prior to its release into the circulation. During my PhD studies, my project revolved around the intracellular aspects and behavior of the FVIII protein, with focus on the GABARAP protein in this regard. In the following section I will discuss and elaborate on the obtained results and Data.

5.2. Comparative Effects of Selected CRISPR/Cas9-KOs on FVIII, FV and vWF: Overlaps and Differences

Expression of FV and vWF in parental HEK293p, HEK28^{WT} and the KO cells, **first** showed clear discrepancies in detecting the two proteins; FV was less detectable intracellularly

but was apparent by WB in cell media (extracellularly), while the opposite was seen for vWF, as illustrated in **Figure 14**. Despite these differences, both FV and vWF exhibited measurable activity levels in the media **(Figure 15)**. **Second**, FV was generally more efficiently secreted than FVIII, whereas vWF activity was comparable to that of FVIII. **Third**, positive correlations were observed between the secretion levels of either FV or vWF and FVIII across various CRISPR/Cas9-KO clones, which reflects more or less close influences of the targeted proteins on the processing of FV, vWF and FVIII **(Figure 15)**. However, **Exceptionally**, $CANX^{KO}$ and $GABARAPL1^{KO}$ clones showed parallel effects, increasing FVIII and vWF secretions yet decreasing FV secretion **(Figure 15)**.

These results align with what is reported in earlier literature, where FV was documented to circulate in plasma at significantly higher levels than FVIII—8 µg/mL for FV compared to 0.2 µg/mL for FVIII [100]. Even in recombinant systems, FV exhibited enhanced secretion in comparison to FVIII; in this case, FVIII was more detected intracellularly, whereas FV was instead found to be more secreted, as obtained in our system [100].

Additionally, the variation between the secretion levels of the three proteins, where FV appears more efficiently secreted than both FVIII and vWF, could be linked first, to the ''aggregation'' characteristic attributed to the FVIII protein which allows it to form reversible ATP-dependent amyloid-like structures within the ER [34]. Second, to the fact that FVIII and vWF appear to possess a wider protein interactome in the ER when compared to FV, e.g. FVIII interacts with Calnexin and BiP, and vWF interacts-transiently- also with BiP, two ER resident chaperones, which were not evidenced to interact with FV [33, 45, 100].

Furthermore, the contrast between the parallelism in effects of $CANX^{KO}$ and $GABARAPL1^{KO}$ between FV (decrease) and FVIII (increase) secretions, highlights a potential functional distinction in how both proteins are processed. This observation conforms to the fact that despite the close homology between FV and FVIII and the overlapping characteristic of interacting with LMAN1 and MCFD2 proteins in the ERGIC compartment, their interactome with other cellular proteins, like CANX and BiP in the ER [33] differs, subsequently influencing differential ER and ER- associated regulative processes. For example, Calnexin, which interacts with FVIII and not with FV, is linked

to autophagy processes (ER-phagy) in which GABARAPL1 plays a key role during autophagosome formation and fusion events with lysosomes, a potential explanation in the parallel effects observed for $CANX^{KO}$ and $GABARAPL1^{KO}$. Therefore, the differential spectrum of FVIII, FV and vWF interactome(s) strongly appears to guide their intracellular trajectories as well as these trajectories' requirements (e.g. energetic, kinetic…etc.) and to further immensely impact the levels at which these coagulation factors are secreted.

5.3. Effects of CRISPR/Cas9-KOs on Intra- and Extracellular FVIII phenotypes

5.3.1. Insights into The Cooperative Roles of LMAN1 & MCFD2 in FVIII Transport in the ERGIC and TGN-related Organelles

As anticipated, compared to $HEK28^{WT}$ cells, $LMAN1^{KO}$ and $MCFD2^{KO}$ significantly reduced FVIII secretion **(Figure 13)**. Furthermore, $LMAN1^{KO}$ and $MCFD2^{KO}$ clustered together based on the average Pearson Correlation Coefficients (PCCs) of FVIII co-localizations with 13 cellular markers **(Figure 21)**. This observation aligns with the well-established cooperative roles of LMAN1 and MCFD2 together.

Both LMAN1 and MCFD2 form together a 1:1 stoichiometric cargo-receptor complex in a pH and Ca^{2+}dependent manner capable of transporting glycosylated proteins with a high-mannose N-linked glycan core ($Man_9GlcNAc_2$), such as FVIII and FV, within the ER-Golgi intermediate compartment (ERGIC) [52, 54, 101, 102]. The findings obtained in our HEK cell system mirror the pathophysiology of combined FV/FVIII deficiency, which arises from mutations in the transport proteins LMAN1 and MCFD2, rather than in the coagulation factors themselves [52, 101].

These results showed additionally that the absence of LMAN1 or MCFD2 clearly disrupted the ERGIC-mediated trafficking of FVIII, significantly hindering its Golgi-dependent secretion **(Figure 13. Figure 21)**. Also, FVIII showed decreased co-localization with endosomal vesicle markers (Rab7, Rab11) and lysosomal markers (ARL8B, LAMP1) in the absence of LMAN1 and MCFD2 **(Figure 21)**. These results suggest that disruption of FVIII-Golgi-dependent trafficking caused by the depletion of

LMAN1 or MCFD2 impairs as well FVIII sorting between the trans-Golgi network (TGN) and endosomes, or vice versa.

5.3.2. Insights into the Regulatory Roles of CANX & CALR -the ER Chaperones- and GABARAP- the ATG8-Protein

Despite the contrasting effects of $CANX^{KO}$ and $CALR^{KO}$ on FVIII secretion levels—increased for $CANX^{KO}$ and reduced for $CALR^{KO}$ **(Figure 13)**, both clones clustered together (considering the co-localization with intracellular markers), interestingly adding to their group one more member: the $GABARAP^{KO}$ **(Figure 21)**.

In fact, it is very comprehensible for Calnexin and Calreticulin to cluster together as this outcome reflects their common operative mechanisms as ER chaperones and QC officers. The latter is carried out by the binding of CANX/CALR to newly synthesized mono-glycosylated proteins ($Glc_1Man_9GlcNAc_2$), such as FVIII, and subsequent recruiting of additional ER aiding chaperones such as ERp57, thereby slowing down the kinetic flux of glycoproteins until reaching a stable conformation before escaping the endoplasmic reticulum for further trafficking [32, 103]. Although the two ER chaperones share structural and functional commonalities, aspects like their different roles in regulating calcium homeostasis inside and outside of the endoplasmic reticulum, varying molecular weights, distinguishable ER localizations, as well as their differing mobility characteristics, proposes distinct functions [32, 40, 44, 103]. Examining these similarities and differences provides deeper insights into how CANX and CALR function in regulating quality control mechanisms. Both proteins employ a similar mode of action in binding glycoproteins within the ER ensuring proper folding, however, CANX's role in the ER extends beyond this, as it also participates in processes associated with proteasomal degradation through binding and substrate delivery to Endoplasmic Reticulum Degradation-Enhancing α-Mannosidase-Like Protein (EDEM), therefore through direct participation in the ER- associated degradation (ERAD) [43, 104]**.** In contrast, Calreticulin appears to regulate not only the interior of the endoplasmic reticulum but also the broader intracellular environment. It achieves this by expanding its range of interactions with a multitude of substrates and signaling pathways [44, 103, 104]. In fact, CALR is a multifunctional protein involved in various cellular processes, including gene expression, cell adhesion, autoimmunity, apoptotic cell clearance and

cell migration in addition to its well-established roles in the ER, specifically in lectin chaperoning and regulation of Ca^{2+} homeostasis [105-107]. For example, based on the ability of CALR of binding the synthetic "KXFF ($^{K}/_{R}$) R" peptide, researchers proposed that it might also interact with the C-terminal cytoplasmic domain of α-integrins, influencing thereby their processing and function and subsequently cell adhesiveness. Furthermore, by binding to the "KXFF($^{K}/_{R}$)R" peptide in the DNA-binding domain of steroid receptors and transcription factors, CALR interferes with their binding with DNA in *in vitro* models [105].

Previously, the absence of data in early literature led to the assumption that CALR functions exclusively within the ER lumen, with no evidence of its presence in the cytosol [105]. However, more recent findings have demonstrated the presence and translocation of CALR outside of the ER lumen, e.g. the CALR-GABARAP interactions that were identified through microscopic co-localization experiments in Neuro-2a cells, identifying these interactions as punctate structures in several compartments with no clear and exclusive ER localization pattern [80]. Additionally, CALR has been shown to translocate to the cell surface during immunogenic cell death (ICD) in multiple myeloma cells [82]. Even in viable cells, evidence of surface CALR functioning as a ligand for LDL-receptor related protein (LRP) was reported [108]. Beside these cited examples, the scientific literature extensively explores the involvement of CALR in many other biological mechanisms in health and also in pathophysiological conditions and disease.

These differential roles of Calnexin and Calreticulin could somehow help explain the disparity observed in the KO-effect of the two ER chaperones on FVIII secretion levels, as despite their shared roles in lectin chaperoning, they present a broad range of functional differences **(Figure 13)**. Furthermore, when comparing the interactions of Calnexin and Calreticulin with FV and FVIII, it appears that both chaperones interact with FVIII while only Calreticulin bind FV. This notion along with the correlation of these interactions to the secretion levels of FV and FVIII (FV higher than FVIII), these findings emphasize the dominant role of Calnexin in retaining FVIII within the ER. In contrast, Calreticulin appears to influence the efficiency of FVIII folding. [33, 104]

Supplementary to its role in protein quality control, CANX has also been identified as a co-receptor in ER-phagy, a process during which recycling of ER size and proteome is facilitated, thereby maintaining ER homeostasis upon ER extension and ER stress recovery phase [109]. ER-phagy is a form of selective autophagy stimulated by ER stress, which could also be triggered by FVIII aggregation and accumulation in the endoplasmic reticulum [109, 110]. During ER-phagy, CANX interacts with a protein called FAM134B [110], the latter contains a C-terminal LIR domain (LC3B Interacting Region) allowing its binding to LC3 and GABARAP proteins, promoting thereby the clearance of unwanted or damaged ER components [109]. For certain proteins, like procollagen I, the involvement of other ER quality control components along this process, such as CALR, is essential to facilitate their efficient degradation via lysosomal pathways [110]. The coordinated interactions between ER chaperones (CANX/CALR), ER-phagy receptors (FAM134B), and autophagy-related proteins (e.g., GABARAP) likely account for the similar intracellular localization patterns of FVIII observed in $CANX^{KO}$, $CALR^{KO}$, and $GABARAP^{KO}$ cells. This suggests that, like CANX and CALR, GABARAP might be playing a role in regulating ER- related machineries and ER homeostasis, though it likely acts indirectly or at a later stage. While CANX and CALR stabilize misfolded glycoproteins by directly binding to their carbohydrates and linking them to the autophagy machinery via ER-phagy receptors such as FAM134B, GABARAP likely participates in the subsequent steps in the ER-phagy process.

In addition, it was evident in that $CALR^{KO}$ was closer to $GABARAP^{KO}$ – behaving almost identically-, in effect on different aspects of the FVIII phenotypes (intra- and extracellularly). Actually, the research group led by *Prof. Dr. Willbold* has studied the ligand properties of the GABARAP protein [111], where they identified CALR as an interacting partner of GABARAP [80]. They have also demonstrated the protein sites involved in this interaction, their binding affinity, and their intracellular co-localization, which was visualized as a cytosolic dotted pattern [80, 81, 112, 113]. Based on the latter findings, GABARAP appears to favor the binding of the cytosolic over the ER form of CALR, especially that GABARAP was also never reported to co-localize to the Endoplasmic Reticulum. This might be due to the functional specificity of CALR that is linked to its specific localization, given that CALR has been described over the history

to participate in a myriad of intra- and extracellular processes [114-116]**.** We, therefore, rule out a synchronized effect of Calreticulin and GABARAP on FVIII within the endoplasmic reticulum.

In another study**,** *Gulla et. al.* have demonstrated that the absence of GABARAP led to altered immunogenic cell death (ICD) and a reduced phagocytosis of multiple myeloma cells. They observed that the deletion of GABARAP disrupted the Golgi morphology as well as the autophagy machinery, which in turn affected the intracellular trafficking of CALR and subsequently its further exposure on the cell surface, a crucial step for recruiting phagocytes. Notably, Bortezomib, a proteasomal inhibitor which enhanced CALR-GABARAP interaction, highlights the importance of specific conditions in enabling such interactions [82, 83].

Nevertheless, in HEK28^{WT}, no physical interaction between FVIII and GABARAP nor between CALR and GABARAP under normal conditions, without interference or induction by specific cell treatments (e.g. Bortezomib) was detected **(Supplementary Figure 2.).** On the other hand, in reported studies, the interaction between CALR and GABARAP was approached via *in vitro* assays such as phage display screening, fluorescence titration, Surface Plasmon Resonance (SPR) spectroscopy, as well as cell-based assays including either neural or tumorous cells (brain lysate extracts, N2a, AMO1 cells)[80-83]. This suggests that the HEK293 cell system might not accurately harbor these interactions due to physiological and mechanistic differences in comparison to other cell types and tissue systems. It could be therefore that in HEK293 cells GABARAP influencing the trafficking of CALR- a secreted protein like FVIII- which might thereby indirectly affect FVIII trafficking.

Moreover, there was a clear evidence of GABARAP participation in the ER-Golgi intermediate compartment, especially in experiments where cells were under Brefeldin A exposure FVIII secretion reduced the most in HEK28^{WT}. This effect is expected since BFA directly targets the ERGIC compartment, which is considered as a key route during FVIII biogenesis and synthesis [24, 25]. However, despite the significant impact of BFA on HEK28^{WT} cells, GABARAP^{KO} cells appeared unaffected by BFA exposure **(Figure 28)**. This observation suggests that BFA targeted compartments/mechanisms might as well be maintained or regulated by the

GABARAP protein. In fact, BFA interferes with the formation of COPI vesicles by maintaining the ARF1-Sec7 complex in an inactive GDP-bound state, which in turn inhibits the vesicular traffic in the ERGIC compartment [93].

BFA has been also demonstrated to alter Golgi stacks and to therefore fragment the Golgi apparatus [93]. Similarly, the lack of the GABARAP protein under normal conditions, showed the highest alteration of the trans-Golgi network, when compared to other gene-KOs and wild-type cells **(Figure 25)**. In addition, the intersection of co-localization maps of GABARAP and FVIII showed a clear overlap around proteins of the ERGIC compartment including COPI vesicles **(Figure 22- 23-24)**. These findings help clarify the neutral effect of BFA on FVIII secretion in GABARAP^{KO} cells.

Furthermore, GABARAP interacts with GM130, a marker of the cis-Golgi network, which plays a role in maintaining the structural integrity of the Golgi apparatus [77]. The interaction between GM130 and GABARAP is regulated by the WAC protein (WW Domain-Containing Adapter with Coiled-Coil), where WAC influences the interaction between GM130 and GABARAP, impacting whether GABARAP is retained in the Golgi or to be released to the pericentriolar matrix (PCM) which usually serves autophagosome formation under amino acid starvation conditions [77, 117]. Furthermore, numerous studies have highlighted the reciprocal relationship between the roles of GABARAP proteins in autophagy and their localization within the Golgi apparatus. This interplay influences both compartments, bridging autophagosome formation with Golgi-dependent mechanisms [72, 77, 117-119].

Calnexin and Calreticulin are well-known to physically interact with FVIII [24, 25, 33, 34], as also confirmed by IP- and co-IP experiments, however, GABARAP did not exhibit such complex formation with FVIII under normal conditions **(Figure 20)**. Nevertheless, immunofluorescence staining revealed low to moderate co-localization of GABARAP with FVIII **(Figure 19)**, a higher co-localization of GABARAP with FL-FVIII when compared to BDD-FVIII, as well as binding of GABARAP to FL-FVIII (Full-length FVIII), but not to the BDD-FVIII (B-deleted-domain FVIII) in Bio-layer interferometry assays **(Figure 18)**. These might be interpreted as follows: The interaction between FVIII and GABARAP may be transient or unstable, rendering it undetectable under normal experimental conditions, moreover, the differences between the very high molecular

weight of the FVIII protein (300 kDa) in comparison to GABARAP (16 kDa) hardens the possibility of detecting such a binding, also this binding, when existing would only be detectable in specific systems or cell models or even induced conditions. Such results also highlight the critical role of the B-domain, which is central to FVIII's glycosylation—a feature essential for interactions with ER chaperones and ERGIC proteins [24, 25, 120]. One possibility is that GABARAP could be indirectly associated to FVIII by relating to proteins which directly physically interact with FVIII (e.g. Calnexin and Calreticulin) or with cellular compartments involved in FVIII synthesis and trafficking (Endoplasmic Reticulum, ERGIC, Golgi apparatus).

5.3.3. Divergent Effects across the ATG8-proteins GABARAP, GABARAPL1 and GABARAPL2: Insights into Substrate & Functional Specificity

According to all obtained results in this project, the GABARAP^{KO} exhibited a very clear and obvious separation from the knockouts of its homologs: GABARAPL1 and GABARAPL2. **First**, GABARAP^{KO} showed decreased FVIII accumulation and activity in cellular media like CALR^{KO}, LMAN1^{KO} and MCFD2^{KO}, opposing GABARAPL1^{KO}, GABARAPL2^{KO} and Atg7^{KO}, which showed increased FVIII secretion, similarly to the CANX^{KO} **(Figure 13). Second,** as shown in **Figure 21**, GABARAP^{KO} influenced the intracellular distribution of FVIII in a closely aligned manner with the ER chaperones knockouts Calnexin and Calreticulin. In contrast, GABARAPL1^{KO} and GABARAPL2^{KO} formed a distinct, separate cluster, close to Atg7^{KO}. **Third**, quantification analysis of Mitochondria in the different cell lines, mirrored this divergence, showing less mitochondrial occupied area (per cell), and less mean mitochondrial pixel intensity for GABARAP^{KO}, like CALR^{KO}, and more for GABARAPL1^{KO} and GABARAPL2^{KO} similarly to CANX^{KO}, in comparison to HEK28^{WT} **(Supplementary Figure 1).** These results were as well paralleled in experiments where ATP and energetic levels were assessed using ATP-luciferase and ATP-linked respiration Seahorse experiments [El. Maarri et. al., Manuscript in Submission]. In the same study, ATP levels measured using both the Luciferase and Seahorse assays showed a positive correlation with FVIII secretion levels in various CRISPR/Cas9 knockout clones.

This connection becomes particularly relevant when considering autophagic events like ''Mitophagy''. Mitophagy is a selective autophagy process targeting damaged mitochondrial material or entire mitochondria organelles for catabolic degradation [121]. In fact, Mitophagy is a very crucial process through which quantity and quality of Mitochondria is well maintained, optimizing thereby energy production to meet the functional demands of the cell [121, 122]. The GABARAP proteins, as essential players of the autophagy machinery, also participate in Mitophagy [72]. According to Schaaf et. al, although GABARAP, GABARAPL1 and GABARAPL2, all three function in mitophagy-associated processes, their interactome in this regard appears specific. In their review they have classified the GABARAP(s) interactions as follows: GABARAP interacts with ALFY and NBR1, GABARAPL1 with PLEKHM1 and GABARAPL2 with TRIM5α during mitophagy [72]. However, a deeper analysis of the literature shows overlaps of these interactions among proteins of the GABARAP subfamily. It is in fact easier to distinguish between the LC3 and the GABARAP subfamilies, yet much harder to identify specific and differential interacting partners among the GABARAPs. Although it is difficult to differentiate precisely between the GABARAPs due to the great similarity between them, there is clarity regarding their differential effect on the general energetic and homeostatic condition of the cell, as reached through the presented results.

5.4. Cell Treatment Analysis: Insights into FVIII Trafficking in the Endomembrane System

In parallel to the observation concerning the neutral effect of BFA treatment on GABARAP^{KO} cells (discussed in details in the previous section), BFA significantly interfered with FVIII secretion in HEK28^{WT}, CANX^{KO}, and less with CALR^{KO} **(Figure 28)**. This outcome is anticipated, likely due to the known effect of this anti-viral fungal drug on vesicular trafficking between the ER and Golgi compartments) [93, 95], thereby disrupting the conventional secretory pathway utilized by FVIII during ERGIC transport. However, the residual levels of FVIII activity in the media following BFA treatment suggest the involvement of alternative or unconventional secretion or trafficking pathways for FVIII. Supporting this hypothesis, the residual FVIII secretion in LMAN1-deficient cells was annulled when exposed to BFA **(Figure 28)**. This observation

coincided with reduced FVIII co-localization with LAMP1, the lysosomal marker **(Figure 29)**.

In LMAN1-deficient cells, the abolishment of FVIII secretion upon BFA treatment also suggests that the compound disrupts a machinery which might be compensating for ERGIC-dependent FVIII secretion. Interestingly, the lack of a global impact of BFA—which primarily affects Golgi-dependent trafficking—on the intracellular co-localizations of FVIII further supports the involvement of complex, unconventional, and compensatory mechanisms regulating FVIII secretion **(Figure 29)**. On the contrary, glucose starvation reduced FVIII secretion in all tested cell clones, except for LMAN1^{KO} cells, where an unexpected increase was observed **(Figure 28)**. This remarkable increase coincided, interestingly, with enhanced FVIII co-localization with GM130 and TGN46 (Golgi markers), as well as Rab7 and LAMP1 (markers of late endosomes, lysosomes, and late autophagosomes) **(Figure 29)**. These findings strongly suggest a link and a supportive role of the endosomal machinery in ERGIC-Golgi-dependent FVIII trafficking.

In fact, BFA perturbs ERGIC trafficking in mammalian cells primarily and results in the so-called ER-Golgi hybrids or ''BFA compartments''. During the formation of BFA compartments the Golgi morphology is not only disturbed but also proteins within this compartments are re-distributed and differently organized, for instance, elements of the *trans*- Golgi stacks and endocytic/endosomal organelles would contribute to the membrane formation of these special compartments [(94)]. Therefore, BFA also affects trafficking through the *trans*- Golgi Network (TGN), endosomes, and lysosomes [(94)]. Based on the latter and on the consistent correlation between FVIII secretion and its co-localization with endo-lysosomal markers, it could be strongly suggested that these compartments are potential contributors in FVIII trafficking (sorting, storage, regulation, or secretion).

Additionally, when Rab7, a Ras-related protein was inhibited by the competitor compound CID1067700, FVIII activity was reduced in the media across all cell lines **(Figure 28)**. Rab7 plays a role in the maturation of endosomes by participating in early endosomes- to late endosome conversion (by Rab5 to Rab7 conversion), and the subsequent fusion with lysosomes [(123)]. On the other hand, Rab7 is also found on the

membranes of late autophagosomes, which could intersect with late endosomes either at the lysosomes by fusing the lysosomes, or by directly fusing late endosomes forming a structure called ''amphisomes'' [123-125]. Amphisomes are known to primarily participate in the maturation of autophagosomes, meaning in autophagy and degradative mechanisms in the cells. It could as well be contributing to regulated secretion events like in cases such as mucin granules secretion in Goblet cells [125]. Noteworthy is that FVIII showed low to almost undetectable co-localizations with LAMPI, and LC3B but moderate with Rab7 and another distinguished protein found to localize autophagosomes, and amphisomes; VAMP8 [124]. Under Rab7 inhibited conditions, FVIII a major trend was observed in KO clones, but not in WT, which is that FVIII decreased in co-localization with VAMP8 **(Figure 29),** an outcome which raises the question of amphisomes involvement in FVIII trafficking.

Finally, chloroquine treatment resulted in a decrease in FVIII secretion across all clones, **(Figure 28)**. This result was paralleled intracellularly with reduced FVIII co-localization in most cellular compartments **(Figure 29)**. The effect of chloroquine was expected, given that chloroquine blocks autophagosome-lysosome fusion events [126, 127], endosomal-lysosomal trafficking [126], cause mitochondrial damage [128, 129] impairing therefore energetic levels which are the motors of cellular metabolism. Again, the residual FVIII secretion observed in the absence of LMAN1 (ERGIC protein) that was completely abolished upon CQ treatment- a similar observation to what happened after BFA treatment- further reinforces the participation of *trans*- Golgi and post- Golgi sorting events in the trafficking machinery of FVIII, as well as their close connection to pre-Golgi (ERGIC) and Golgi processing events.

5.5. Combined CRISPR/Cas9- DKO effects on Intra- & Extracellular FVIII Profiles

5.5.1. LMAN1^{KO}- DKO Related Phenotypes

Compared to HEK28^{WT}, the deletion of the whole cargo-receptor complex LMAN1/MCFD2 in cultured cells resulted in decreased FVIII activity (46% decrease)

(Figure 32). Notably, FVIII secretion was lower in MCFD2^{KO} (96% decrease) cells than in LMAN1^{KO} cells (77% decrease) **(Figure 32)**. These observations were completely consistent with studies involving LMAN1/MCFD2 double deficient mice, where the DKO exhibited FVIII levels (60.6%) closer to those of the LMAN1^{KO} (50.4%) and more than those obtained in MCFD2^{KO} mice (34.3%) [130]. In addition, double LMAN1 and MCFD2 deficient mice were partially lethal, a phenotype observed in LMAN1^{KO} but not in MCFD2^{KO} mice. The latter mice exhibited normal growth with no noted complications [130]. It is true that FVIII secretion in the DKO was closer to that observed in LMAN1^{KO} rather than in MCFD2^{KO}, however and more specifically, this secretion level appeared to be even higher in the DKO than in both single-KOs of the ERGIC transporters, suggesting the presence of the so-called ''positive epistasis''. The latter represents a sort of ''sign epistasis'' which refers to the situation in which the combination of certain mutations results in a fitter phenotype- in this context, higher FVIII activity [131, 132]. Furthermore, CANX^{KO}/LMAN1^{KO} dropped FVIII activity similarly to LMAN1^{KO} **(Figure 32)**, underscoring the **dominant** and significant role of LMAN1 in FVIII transport in the ERGIC compartment. Here, it appears that the effect of the CANX^{KO} was almost neglected due to the essential function of ERGIC transport in the secretion machinery of FVIII which shifted the phenotype towards that seen in LMAN1^{KO}.

These reductions in FVIII activity across LMAN1-related DKOs correlated with decreased FVIII delivery to the Golgi apparatus **(Co-localization with GM130/TGN46, Figure 32)**. However, FVIII still localized in the ER-Golgi intermediate compartment (ERGIC) (Sec31a/COPII vesicles) in these DKOs **(Figure 32)**, suggesting that FVIII may- in this case- utilize a non-selective COPII-related bulk-flow secretory mechanism, which does not involve specific molecules, proteins or receptors, but rather rely on the membrane bulk and fluid incorporations in transport vesicles [35]. However, despite its presence in COPII vesicles in these DKOs, FVIII failed to reach the Golgi apparatus, raising questions about potential underwent sorting mechanisms in the ERGIC and *cis*-Golgi compartments (e.g. ER retrograde transport through COPI vesicles) [31, 35]. In double LMAN1/MCFD2-deficient cells, FVIII non reduced co-localization with Rab8a in comparison to WT-cells and to respective single-KOs,

suggests the possibility of a Golgi-by passing secretory pathway for FVIII in case of ERGIC disruptions **(Figure 32)**. It is also of benefit to mention, that the family of L-type lectins, to which LMAN1 also known as ERGIC-53 belongs, also contains other L-type lectin members such as VIP36, VIPL and ERGL, which might as well alternatively assist in ER export and ERGIC transport in scenarios where LMAN1's function is impaired or deleted [35, 133]. The latter proteins are reported to be associated with ERGIC-53 (LMAN1) and the transport of glycoproteins in the ERGIC compartment, however, their specific binding potential to FVIII or other glycoproteins is yet to be investigated [133]. Additionally, lower co-localization with lysosomal markers (LAMPI, ARL8B and Rab7) in the LMAN1-associated DKOs **(Figure 32)** reinforces the involvement of the endo-lysosomal system in FVIII trafficking, and the role of LMAN1 and maybe MCFD2 in this route, or vice versa.

5.5.2. CANX^{KO}; CALR^{KO} and GABARAP^{KO}-DKO-Related Phenotypes

Compared to HEK28^{WT}, Double knockouts of ER chaperones CANX and CALR demonstrated a reduction in FVIII activity in the media. The single absence of Calnexin increased FVIII secretion, while the single deletion of CALR exhibited an opposite effect **(Figure 13. Figure 32.).** The absence of both CANX and CALR simultaneously resulted in an intermediate drop in FVIII secretion compared to their respective single knockouts, demonstrating a clear **additive** effect **(Figure 32)**. Additionally, in the absence of both CANX and CALR, FVIII co-localization with PDI (protein disulfide-isomerase) significantly increased compared to HEK28^{WT}, and the single-KOs of CANX and CALR **(not shown).** This finding aligns with another study that reported a DKO of CANX and CALR enhancing the association of Influenza Virus Hemagglutinin with other ER chaperones like BiP, while being under normal conditions a non-BiP-binding protein [104], hinting therefore to the presence of compensating events in the ER in cases where the efficiency of protein quality control mechanisms is triggered.

Further monitoring of DKOs involving ER chaperones CANX^{KO}/GABARAP^{KO} (78% increase) and CALR^{KO}/GABARAP^{KO} (55% decrease) revealed FVIII secretion patterns closer to those observed in CANX^{KO} (34% increase) or CALR^{KO} (59% decrease), respectively **(Figure 32).** This observation suggests that in the absence of CANX and

CALR, GABARAP function is automatically impaired, or that the knockout of either ER chaperones automatically abolishes or overpowers the influence of the GABARAP protein on FVIII secretion. This phenotype was also observed in rescue experiments, where the double rescue of CANX and CALR with GABARAP restored the DKO phenotype in a manner similar to the rescue of CANX and CALR in single $CANX^{KO}$ and $CALR^{KO}$ conditions. Notably, the rescue of GABARAP in $GABARAP^{KO}$ was not efficient, suggesting either permanent phenotypic damage or the involvement of compensatory mechanisms. These mechanisms might include other proteins or homologs of GABARAP, such as GABARAPL1.

One recurring observation was the increased co-localization of FVIII with Rab8a in $CANX^{KO}$/$GABARAP^{KO}$ cells compared to the respective single KOs. This outcome positively correlated with the higher FVIII activity observed in the media of the DKO compared to the respective single KOs, thereby emphasizing a role of the Rab8a in FVIII exocytosis on one hand, and its possible involvement in post- Golgi trafficking that may be compensating in case of ER functional or ERGIC transport events disruptions, on the other.

Finally, and based on the intracellular distribution of FVIII and the co-localization analysis (PCCs), the clustering of $CANX^{KO}$/$CALR^{KO}$, $CANX^{KO}$/$GABARAP^{KO}$, and $CALR^{KO}$/$GABARAP^{KO}$ in one group **(Figure 33),** on one hand, and their respective single knockouts on the other hand **(Figure 21),** suggests shared pathways, redundancy, or compensatory mechanisms involving the interplay between the ER chaperones and GABARAP. This interconnection also strongly hints to a downstream role for GABARAP in processes regulated by initially CANX and CALR in the endoplasmic reticulum, going further beyond to downstream intracellular compartments and machineries including GABARAP.

Conclusions

- GABARAP influences FVIII **secretion** in a manner similar to Calreticulin and FVIII **intracellular trafficking** similarly to both Calnexin and Calreticulin- the ER chaperones. It appears therefore that GABARAP regulates FVIII trafficking, contributing to ER-associated homeostasis and quality control mechanisms. However, its action is likely not directly within the ER but rather downstream of Calnexin and Calreticulin, involving adapter or bridge proteins which potentially modulates interactions between GABARAP and the ER chaperones. Besides, GABARAP plays a crucial role in maintaining the homeostasis of the ERGIC vesicular flow by preserving organized Golgi morphology. This regulation, in turn, impacts FVIII transport within the ERGIC.

- In addition to the well characterized trafficking of FVIII within the early secretory pathway (ER, ERGIC, and Golgi compartments), the above data suggest that FVIII may also undergo *trans*- Golgi sorting events involving VAMP8-, Rab7-, and Rab8- positive vesicles. This suggests the presence of FVIII in endosome-related vesicles and implies the participation of further components of the endomembrane system in FVIII exocytosis - an area which is still poorly investigated. Better understanding of this direction brings us nearer to the identification of the specific vesicular machinery supporting the biosynthesis of FVIII, the specific routes guiding its processing, as well as the type of secretion mechanisms it may undergo. This knowledge could as well enhance the ability to more efficiently manipulate recombinant systems utilized in FVIII concentrate production, thereby improving replacement therapies, and reducing manufacturing costs.

Appendix

Mitochondria Staining and Quantification

After staining mitochondria in the CRISPR/Cas9-KO cell lines, images were processed using CellProfiler 4.2.8. Nuclei and cells were outlined to define cytoplasmic areas, where mitochondrial objects were identified, segmented, outlined, and quantified according to the details and formulas provided in the Methods section. For visualization, a mitochondria detection intensity threshold of 0.25 was chosen after extensive testing. Based on the selected quantifications, $CANX^{KO}$, $GABARAPL1^{KO}$, and $GABARAPL2^{KO}$ exhibited the highest mean mitochondrial intensity (117%, 109%, and 149%, respectively, normalized to $HEK28^{WT}$) and the largest mitochondrial area per cytoplasm (107.5%, 120.4%, and 170%, respectively, normalized to $HEK28^{WT}$). In contrast, $CALR^{KO}$ and $GABARAP^{KO}$ displayed lower values for these two parameters: mitochondrial occupied area (63% and 6.5%, respectively) and mean mitochondrial pixel intensity/brightness (86% and 63%, respectively, normalized to $HEK28^{WT}$).

When plotting mitochondrial occupied areas and mean intensities against ATP production levels measured via the Seahorse Assay, a strong correlation was observed between mitochondrial parameters and cellular energetic levels in ER chaperone-related KOs and Atg8-protein-related KOs. The mitochondrial area versus Seahorse ATP levels showed a linear relationship ($y = 4.7502x - 354.83$, $R^2 = 0.8804$), as did mitochondrial intensity versus Seahorse ATP levels ($y = 2.5082x - 131.63$, $R^2 = 0.8755$).

Supplementary Figure 1.

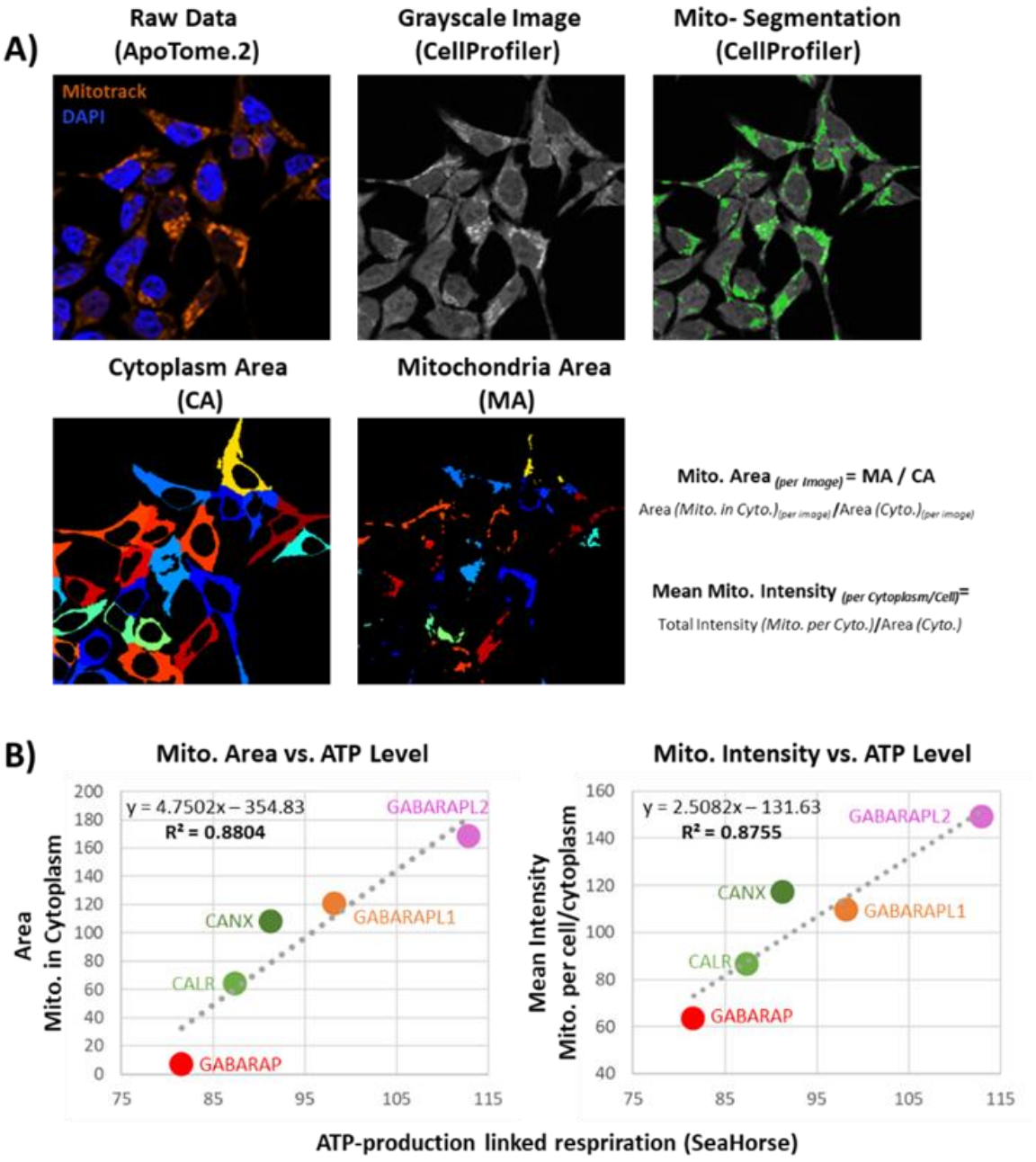

Supplementary Figure 1. Mitochondrial Staining, Quantification, and Correlation with ATP Production. **A)** Top Row (left to right): analysis and quantification workflow for mitochondrial staining. Raw images were captured using ApoTome.2 following mitochondria staining using MitoTracker® Red CMXRos (Invitrogen, #M7512) (orange) and processed into grayscale images by a ''Modules Pipeline'' in CellProfiler 4.2.8. Mitochondria were identified, segmented (green outlines) and further analysed. Second Row (left to right): Identification of cytoplasm and mitochondrial areas following cells and nuclei outlining and nuclei exclusion using specific modules of the CellProfiler 4.2.8 pipeline ("IdentifyPrimaryObjects," "IdentifySecondaryObjects," "IdentifyTertiaryObjects"). Second Row (right): Formulas calculating area (per image) and mean (pixel) intensity (per cell) of mitochondrial objects**. B)** Correlation of Mitochondrial Quantification with ATP levels (ATP-production linked respiration using the Seahorse assay). Correlation analysis of *Y-axis:* area occupied /Mean (pixel) Intensity of mitochondrial objects with *X-axis*: ATP production in $CANX^{KO}$, $CALR^{KO}$, $GABARAP^{KO}$, $GABARAPL1^{KO}$, and $GABARAPL2^{KO}$ (Normalized to $HEK28^{WT}$) shows *for Area*: $y = 4.7502x – 354.83$, $R^2 = 0.8804$; *For Intensity:* $y = 2.5082x – 131.63$, $R^2 = 0.8755$, respectively.

Supplementary Figure 2.

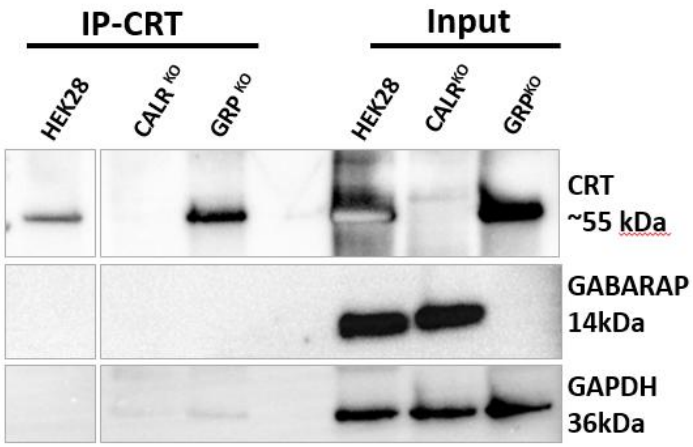

Supplementary Figure2. Assessment of Calreticulin-GABARAP Physical Interaction by IP (immunoprecipitation) and Co-IP (Co-Immunoprecipitation) Assays. Western blot analysis of cell extracts following immunoprecipitation (IP) of CALR in $HEK28^{WT}$, $CALR^{KO}$, and $GABARAP^{KO}$ cell extracts. The PVDF- membrane containing transferred proteins was probed with antibodies against CALR, GABARAP, and GAPDH in addition to corresponding secondary HRP-antibodies.

List of Figures

Supp. Figure 1. Mitochondrial Staining, Quantification, and Correlation with ATP Production.

Supp. Figure 2. Assessment of Calreticulin-GABARAP Physical Interaction by IP (immunoprecipitation) and Co-IP (Co-Immunoprecipitation) Assays.

List of Tables

References

1. L. D. Blood Groups and Red Cell Antigens [Internet] 2005 [Available from: https://www.ncbi.nlm.nih.gov/books/NBK2263/.
2. (ASH) ASoH. [Available from: https://www.hematology.org/education/patients/blood-basics.
3. Smith SA, Travers RJ, Morrissey JH. How it all starts: Initiation of the clotting cascade. Crit Rev Biochem Mol Biol. 2015;50(4):326-36.
4. Gale AJ. Continuing education course #2: current understanding of hemostasis. Toxicol Pathol. 2011;39(1):273-80.
5. Sung YK, Lee DR, Chung DJ. Advances in the development of hemostatic biomaterials for medical application. Biomater Res. 2021;25(1):37.
6. Amr SS, Tbakhi A. Abu Al Qasim Al Zahrawi (Albucasis): pioneer of modern surgery. Ann Saudi Med. 2007;27(3):220-1.
7. Periayah MH, Halim AS, Mat Saad AZ. Mechanism Action of Platelets and Crucial Blood Coagulation Pathways in Hemostasis. Int J Hematol Oncol Stem Cell Res. 2017;11(4):319-27.
8. Palta S, Saroa R, Palta A. Overview of the coagulation system. Indian J Anaesth. 2014;58(5):515-23.
9. Davie EW. A brief historical review of the waterfall/cascade of blood coagulation. J Biol Chem. 2003;278(51):50819-32.
10. Park S, Park JK. Back to basics: the coagulation pathway. Blood Res. 2024;59(1):35.
11. Napeñas JJ, Patton LL. Bleeding and Clotting Disorders. Burket's Oral Medicine2021. p. 665-704.
12. Triplett DA. Coagulation and bleeding disorders: review and update. Clin Chem. 2000;46(8 Pt 2):1260-9.
13. Franchini M, Mannucci PM. The More Recent History of Hemophilia Treatment. Semin Thromb Hemost. 2022;48(8):904-10.
14. Foundation NBD. [Available from: https://www.bleeding.org/bleeding-disorders-a-z/overview/history.
15. Schramm W. The history of haemophilia - a short review. Thromb Res. 2014;134 Suppl 1:S4-9.
16. Franchini M, Mannucci PM. The history of hemophilia. Semin Thromb Hemost. 2014;40(5):571-6.
17. Rogaev EI, Grigorenko AP, Faskhutdinova G, Kittler EL, Moliaka YK. Genotype analysis identifies the cause of the "royal disease". Science. 2009;326(5954):817.
18. Macfarlane RG. An Enzyme Cascade in the Blood Clotting Mechanism, and its Function as a Biochemical Amplifier. Nature. 1964;202(4931):498-9.
19. Pool JG, Shannon AE. Production of high-potency concentrates of antihemophilic globulin in a closed-bag system. N Engl J Med. 1965;273(27):1443-7.
20. Evatt BL. The tragic history of AIDS in the hemophilia population, 1982-1984. J Thromb Haemost. 2006;4(11):2295-301.
21. Franchini M. The modern treatment of haemophilia: a narrative review. Blood Transfus. 2013;11(2):178-82.
22. Jair Lara-Navarro I, Rebeca Jaloma-Cruz A. Current Therapies in Hemophilia: From Plasma-Derived Factor Modalities to CRISPR/Cas Alternatives. Tohoku J Exp Med. 2022;256(3):197-207.
23. Ay C, Frenzel L, Pinachyan K, Le Quellec S. Gene therapy for haemophilia A and B, from basic principles to clinical implementation: An illustrated review. Haemophilia. 2024;30(1):5-15.
24. Orlova NA, Kovnir SV, Vorobiev, II, Gabibov AG, Vorobiev AI. Blood Clotting Factor VIII: From Evolution to Therapy. Acta Naturae. 2013;5(2):19-39.

25. Callaghan MU, Kaufman RJ. Synthesis and Secretion of Coagulation Factor VIII. In: Tanaka K, Davie EW, Ikeda Y, Iwanaga S, Saito H, Sueishi K, editors. Recent Advances in Thrombosis and Hemostasis 2008. Tokyo: Springer Japan; 2008. p. 45-67.
26. Sarmiento Doncel S, Peláez RG, Lapunzina P, Corrales-Medina FF, Díaz Mosquera GA, Bonanad S, et al. Comprehensive Screening of Genetic Variants in the Coding Region of F8 in Severe Hemophilia A Reveals a Relationship with Disease Severity in a Colombian Cohort. Life. 2024;14(8):1041.
27. Shahani T, Covens K, Lavend'homme R, Jazouli N, Sokal E, Peerlinck K, et al. Human liver sinusoidal endothelial cells but not hepatocytes contain factor VIII. J Thromb Haemost. 2014;12(1):36-42.
28. El-Maarri O, Jamil MA, Oldenburg J. Molecular Profiling of Liver Sinusoidal Endothelial Cells in Comparison to Hepatocytes: Reflection on Which Cell Type Should Be the Target for Gene Therapy. Hamostaseologie. 2020;40(S 01):S26-s31.
29. Fomin ME, Zhou Y, Beyer AI, Publicover J, Baron JL, Muench MO. Production of factor VIII by human liver sinusoidal endothelial cells transplanted in immunodeficient uPA mice. PLoS One. 2013;8(10):e77255.
30. Elvevold K, Smedsrød B, Martinez I. The liver sinusoidal endothelial cell: a cell type of controversial and confusing identity. Am J Physiol Gastrointest Liver Physiol. 2008;294(2):G391-400.
31. Ellgaard L, Helenius A. Quality control in the endoplasmic reticulum. Nat Rev Mol Cell Biol. 2003;4(3):181-91.
32. Kozlov G, Gehring K. Calnexin cycle - structural features of the ER chaperone system. Febs j. 2020;287(20):4322-40.
33. Pipe SW, Morris JA, Shah J, Kaufman RJ. Differential Interaction of Coagulation Factor VIII and Factor V with Protein Chaperones Calnexin and Calreticulin*. Journal of Biological Chemistry. 1998;273(14):8537-44.
34. Poothong J, Pottekat A, Siirin M, Campos AR, Paton AW, Paton JC, et al. Factor VIII exhibits chaperone-dependent and glucose-regulated reversible amyloid formation in the endoplasmic reticulum. Blood. 2020;135(21):1899-911.
35. Barlowe C, Helenius A. Cargo Capture and Bulk Flow in the Early Secretory Pathway. Annu Rev Cell Dev Biol. 2016;32:197-222.
36. Oliver JD, Roderick HL, Llewellyn DH, High S. ERp57 functions as a subunit of specific complexes formed with the ER lectins calreticulin and calnexin. Mol Biol Cell. 1999;10(8):2573-82.
37. Kozlov G, Bastos-Aristizabal S, Määttänen P, Rosenauer A, Zheng F, Killikelly A, et al. Structural basis of cyclophilin B binding by the calnexin/calreticulin P-domain. J Biol Chem. 2010;285(46):35551-7.
38. Price ER, Jin M, Lim D, Pati S, Walsh CT, McKeon FD. Cyclophilin B trafficking through the secretory pathway is altered by binding of cyclosporin A. Proc Natl Acad Sci U S A. 1994;91(9):3931-5.
39. Brecker M, Khakhina S, Schubert TJ, Thompson Z, Rubenstein RC. The Probable, Possible, and Novel Functions of ERp29. Frontiers in Physiology. 2020;11.
40. Paskevicius T, Farraj RA, Michalak M, Agellon LB. Calnexin, More Than Just a Molecular Chaperone. Cells. 2023;12(3).
41. Papadopoulos N, Nédélec A, Derenne A, Şulea TA, Pecquet C, Chachoua I, et al. Oncogenic CALR mutant C-terminus mediates dual binding to the thrombopoietin receptor triggering complex dimerization and activation. Nature Communications. 2023;14(1):1881.
42. Michalak M. Calreticulin: Endoplasmic reticulum Ca2+ gatekeeper. Journal of Cellular and Molecular Medicine. 2024;28(5):e17839.
43. Oda Y, Hosokawa N, Wada I, Nagata K. EDEM as an acceptor of terminally misfolded glycoproteins released from calnexin. Science. 2003;299(5611):1394-7.
44. Michalak M, Groenendyk J, Szabo E, Gold LI, Opas M. Calreticulin, a multi-process calcium-buffering chaperone of the endoplasmic reticulum. Biochem J. 2009;417(3):651-66.

45. Dorner AJ, Wasley LC, Kaufman RJ. Protein dissociation from GRP78 and secretion are blocked by depletion of cellular ATP levels. Proc Natl Acad Sci U S A. 1990;87(19):7429-32.
46. Dorner AJ, Wasley LC, Kaufman RJ. Overexpression of GRP78 mitigates stress induction of glucose regulated proteins and blocks secretion of selective proteins in Chinese hamster ovary cells. Embo j. 1992;11(4):1563-71.
47. Georgakopoulos ND, Wells G, Campanella M. The pharmacological regulation of cellular mitophagy. Nat Chem Biol. 2017;13(2):136-46.
48. Padman BS, Bach M, Lucarelli G, Prescott M, Ramm G. The protonophore CCCP interferes with lysosomal degradation of autophagic cargo in yeast and mammalian cells. Autophagy. 2013;9(11):1862-75.
49. Gutierrez JM, Feizi A, Li S, Kallehauge TB, Hefzi H, Grav LM, et al. Genome-scale reconstructions of the mammalian secretory pathway predict metabolic costs and limitations of protein secretion. Nature Communications. 2020;11(1):68.
50. Sabatino DE. Clogging up the pipeline: factor VIII aggregates. Blood. 2020;135(21):1825-7.
51. Soukharev S, Hammond D, Ananyeva NM, Anderson JA, Hauser CA, Pipe S, et al. Expression of factor VIII in recombinant and transgenic systems. Blood Cells Mol Dis. 2002;28(2):234-48.
52. Zhang Y, Liu Z, Zhang B. Separate roles of LMAN1 and MCFD2 in ER-to-Golgi trafficking of FV and FVIII. Blood Adv. 2023;7(7):1286-96.
53. Zheng C, Liu H-h, Yuan S, Zhou J, Zhang B. Molecular basis of LMAN1 in coordinating LMAN1-MCFD2 cargo receptor formation and ER-to-Golgi transport of FV/FVIII. Blood. 2010;116(25):5698-706.
54. Zheng C, Zhang B. Combined deficiency of coagulation factors V and VIII: an update. Semin Thromb Hemost. 2013;39(6):613-20.
55. Watanabe S, Kise Y, Yonezawa K, Inoue M, Shimizu N, Nureki O, et al. Structure of full-length ERGIC-53 in complex with MCFD2 for cargo transport. Nature Communications. 2024;15(1):2404.
56. GM C. The Cell: A Molecular Approach. Sunderland (MA): Sinauer Associates2000.
57. Jékely G. Origin of Eukaryotic Endomembranes: A Critical Evaluation of Different Model Scenarios. Eukaryotic Membranes and Cytoskeleton: Origins and Evolution. New York, NY: Springer New York; 2007. p. 38-51.
58. Mysior MM, Simpson JC. Cell3: a new vision for study of the endomembrane system in mammalian cells. Biosci Rep. 2021;41(12).
59. Bonifacino JS, Glick BS. The Mechanisms of Vesicle Budding and Fusion. Cell. 2004;116(2):153-66.
60. Schmid SL. Clathrin-coated vesicle formation and protein sorting: an integrated process. Annu Rev Biochem. 1997;66:511-48.
61. Alberts B JA, Lewis J, et al. Molecular Biology of the Cell. 4th edition. Transport from the Trans Golgi Network to the Cell Exterior: Exocytosis. New York: Garland Science. 2002.
62. Cai H, Reinisch K, Ferro-Novick S. Coats, tethers, Rabs, and SNAREs work together to mediate the intracellular destination of a transport vesicle. Dev Cell. 2007;12(5):671-82.
63. Shima T, Kirisako H, Nakatogawa H. COPII vesicles contribute to autophagosomal membranes. J Cell Biol. 2019;218(5):1503-10.
64. Cui L, Li H, Xi Y, Hu Q, Liu H, Fan J, et al. Vesicle trafficking and vesicle fusion: mechanisms, biological functions, and their implications for potential disease therapy. Mol Biomed. 2022;3(1):29.
65. Venema CL, Schutgens REG, Fischer K. Pathophysiological Mechanisms of Endogenous FVIII Release following Strenuous Exercise in Non-severe Haemophilia: A Review. Thromb Haemost. 2017;117(12):2237-42.
66. Plantier JL, Guillet B, Ducasse C, Enjolras N, Rodriguez MH, Rolli V, et al. B-domain deleted factor VIII is aggregated and degraded through proteasomal and lysosomal pathways. Thromb Haemost. 2005;93(5):824-32.
67. Varga VB, Keresztes F, Sigmond T, Vellai T, Kovács T. The evolutionary and functional divergence of the Atg8 autophagy protein superfamily. Biologia Futura. 2022;73(4):375-84.

68. Chun Y, Kim J. Autophagy: An Essential Degradation Program for Cellular Homeostasis and Life. Cells. 2018;7(12).
69. Shpilka T, Weidberg H, Pietrokovski S, Elazar Z. Atg8: an autophagy-related ubiquitin-like protein family. Genome Biol. 2011;12(7):226.
70. Sanwald JL, Dobner J, Simons IM, Poschmann G, Stühler K, Üffing A, et al. Lack of GABARAP-Type Proteins Is Accompanied by Altered Golgi Morphology and Surfaceome Composition. Int J Mol Sci. 2020;22(1).
71. Mohrlüder J, Schwarten M, Willbold D. Structure and potential function of γ-aminobutyrate type A receptor-associated protein. The FEBS Journal. 2009;276(18):4989-5005.
72. Schaaf MB, Keulers TG, Vooijs MA, Rouschop KM. LC3/GABARAP family proteins: autophagy-(un)related functions. Faseb j. 2016;30(12):3961-78.
73. Albanesi J, Wang H, Sun H-Q, Levine B, Yin H. GABARAP-mediated targeting of PI4K2A/PI4KIIα to autophagosomes regulates PtdIns4P-dependent autophagosome-lysosome fusion. Autophagy. 2015;11(11):2127-9.
74. Coyle JE, Qamar S, Rajashankar KR, Nikolov DB. Structure of GABARAP in Two Conformations: Implications for GABAA Receptor Localization and Tubulin Binding. Neuron. 2002;33(1):63-74.
75. Chen J, Zhao H, Liu M, Chen L. A new perspective on the autophagic and non-autophagic functions of the GABARAP protein family: a potential therapeutic target for human diseases. Mol Cell Biochem. 2024;479(6):1415-41.
76. Goldin-Azulay K, Fraiberg M, Trofimyuk O, Levin Y, Reuven N, Kopitman E, et al. A new cellular platform for studying autophagy. bioRxiv. 2024:2024.03.28.587157.
77. Joachim J, Jefferies HB, Razi M, Frith D, Snijders AP, Chakravarty P, et al. Activation of ULK Kinase and Autophagy by GABARAP Trafficking from the Centrosome Is Regulated by WAC and GM130. Mol Cell. 2015;60(6):899-913.
78. Bansal S, Vachher M, Burman A. Calreticulin: a quintessential multifaceted protein with therapeutic potential. Journal of Proteins and Proteomics. 2023;14:1-14.
79. Jiang Y, Dey S, Matsunami H. Calreticulin: roles in cell-surface protein expression. Membranes (Basel). 2014;4(3):630-41.
80. Mohrlüder J, Stangler T, Hoffmann Y, Wiesehan K, Mataruga A, Willbold D. Identification of calreticulin as a ligand of GABARAP by phage display screening of a peptide library. Febs j. 2007;274(21):5543-55.
81. Thielmann Y, Weiergräber OH, Mohrlüder J, Willbold D. Structural framework of the GABARAP-calreticulin interface--implications for substrate binding to endoplasmic reticulum chaperones. Febs j. 2009;276(4):1140-52.
82. Gulla A, Morelli E, Johnstone M, Turi M, Samur MK, Botta C, et al. Loss of GABARAP mediates resistance to immunogenic chemotherapy in multiple myeloma. Blood. 2024;143(25):2612-26.
83. Zhao L, Shen Z, Kroemer G, Kepp O. Clinically relevant GABARAP deficiency abrogates bortezomib-induced immunogenic cell death in multiple myeloma. Oncoimmunology. 2024;13(1):2360275.
84. Rosenberg JB, Foster PA, Kaufman RJ, Vokac EA, Moussalli M, Kroner PA, et al. Intracellular trafficking of factor VIII to von Willebrand factor storage granules. J Clin Invest. 1998;101(3):613-24.
85. Shah NB, Duncan TM. Bio-layer interferometry for measuring kinetics of protein-protein interactions and allosteric ligand effects. J Vis Exp. 2014(84):e51383.
86. Dunn KW, Kamocka MM, McDonald JH. A practical guide to evaluating colocalization in biological microscopy. Am J Physiol Cell Physiol. 2011;300(4):C723-42.
87. Costes SV, Daelemans D, Cho EH, Dobbin Z, Pavlakis G, Lockett S. Automatic and quantitative measurement of protein-protein colocalization in live cells. Biophys J. 2004;86(6):3993-4003.
88. Aaron JS, Taylor AB, Chew TL. Image co-localization - co-occurrence versus correlation. J Cell Sci. 2018;131(3).

89. Scientific T. Co-immunoprecipitation (Co-IP) [Available from: https://www.thermofisher.com/de/de/home/life-science/protein-biology/protein-biology-learning-center/protein-biology-resource-library/pierce-protein-methods/co-immunoprecipitation-co-ip.html#:~:text=Because%20co%2Dimmunoprecipitation%20depends%20so,s)%20of%20the%20target%20complex.
90. Ge L, Melville D, Zhang M, Schekman R. The ER–Golgi intermediate compartment is a key membrane source for the LC3 lipidation step of autophagosome biogenesis. eLife. 2013;2:e00947.
91. Thomas G. Furin at the cutting edge: from protein traffic to embryogenesis and disease. Nat Rev Mol Cell Biol. 2002;3(10):753-66.
92. Nakano A. The Golgi Apparatus and its Next-Door Neighbors. Frontiers in Cell and Developmental Biology. 2022;10.
93. Fujiwara T, Oda K, Yokota S, Takatsuki A, Ikehara Y. Brefeldin A causes disassembly of the Golgi complex and accumulation of secretory proteins in the endoplasmic reticulum. J Biol Chem. 1988;263(34):18545-52.
94. Nebenführ A, Ritzenthaler C, Robinson DG. Brefeldin A: Deciphering an Enigmatic Inhibitor of Secretion. Plant Physiology. 2002;130(3):1102-8.
95. Thor F, Gautschi M, Geiger R, Helenius A. Bulk Flow Revisited: Transport of a Soluble Protein in the Secretory Pathway. Traffic. 2009;10(12):1819-30.
96. Ghosh S, Dellibovi-Ragheb TA, Kerviel A, Pak E, Qiu Q, Fisher M, et al. β-Coronaviruses Use Lysosomes for Egress Instead of the Biosynthetic Secretory Pathway. Cell. 2020;183(6):1520-35.e14.
97. Roberts SA, Dong B, Firrman JA, Moore AR, Sang N, Xiao W. Engineering Factor Viii for Hemophilia Gene Therapy. J Genet Syndr Gene Ther. 2011;1.
98. Swaroop M, Moussalli M, Pipe SW, Kaufman RJ. Mutagenesis of a potential immunoglobulin-binding protein-binding site enhances secretion of coagulation factor VIII. J Biol Chem. 1997;272(39):24121-4.
99. Roth SD, Schüttrumpf J, Milanov P, Abriss D, Ungerer C, Quade-Lyssy P, et al. Chemical Chaperones Improve Protein Secretion and Rescue Mutant Factor VIII in Mice with Hemophilia A. PLOS ONE. 2012;7(9):e44505.
100. Pittman DD, Tomkinson KN, Kaufman RJ. Post-translational requirements for functional factor V and factor VIII secretion in mammalian cells. J Biol Chem. 1994;269(25):17329-37.
101. Zhang B, McGee B, Yamaoka JS, Guglielmone H, Downes KA, Minoldo S, et al. Combined deficiency of factor V and factor VIII is due to mutations in either LMAN1 or MCFD2. Blood. 2006;107(5):1903-7.
102. Spreafico M, Peyvandi F. Combined Factor V and Factor VIII Deficiency. Semin Thromb Hemost. 2009;35(4):390-9.
103. Ellgaard L, Helenius A. Quality control in the endoplasmic reticulum. Nature Reviews Molecular Cell Biology. 2003;4(3):181-91.
104. Molinari M, Eriksson KK, Calanca V, Galli C, Cresswell P, Michalak M, et al. Contrasting functions of calreticulin and calnexin in glycoprotein folding and ER quality control. Mol Cell. 2004;13(1):125-35.
105. Michalak M, Corbett EF, Mesaeli N, Nakamura K, Opas M. Calreticulin: one protein, one gene, many functions. Biochem J. 1999;344 Pt 2(Pt 2):281-92.
106. Martins I, Kepp O, Galluzzi L, Senovilla L, Schlemmer F, Adjemian S, et al. Surface-exposed calreticulin in the interaction between dying cells and phagocytes. Annals of the New York Academy of Sciences. 2010;1209(1):77-82.
107. Gold LI, Eggleton P, Sweetwyne MT, Van Duyn LB, Greives MR, Naylor S-M, et al. Calreticulin: non-endoplasmic reticulum functions in physiology and disease. The FASEB Journal. 2010;24(3):665-83.
108. Gardai SJ, McPhillips KA, Frasch SC, Janssen WJ, Starefeldt A, Murphy-Ullrich JE, et al. Cell-Surface Calreticulin Initiates Clearance of Viable or Apoptotic Cells through trans-Activation of LRP on the Phagocyte. Cell. 2005;123(2):321-34.

109. Loi M, Fregno I, Guerra C, Molinari M. Eat it right: ER-phagy and recovER-phagy. Biochem Soc Trans. 2018;46(3):699-706.
110. Forrester A, De Leonibus C, Grumati P, Fasana E, Piemontese M, Staiano L, et al. A selective ER-phagy exerts procollagen quality control via a Calnexin-FAM134B complex. Embo j. 2019;38(2).
111. Mohrlüder J, Schwarten M, Willbold D. Structure and potential function of gamma-aminobutyrate type A receptor-associated protein. Febs j. 2009;276(18):4989-5005.
112. Thielmann Y, Mohrlüder J, Koenig BW, Stangler T, Hartmann R, Becker K, et al. An indole-binding site is a major determinant of the ligand specificity of the GABA type A receptor-associated protein GABARAP. Chembiochem. 2008;9(11):1767-75.
113. Weiergräber OH, Stangler T, Thielmann Y, Mohrlüder J, Wiesehan K, Willbold D. Ligand binding mode of GABAA receptor-associated protein. J Mol Biol. 2008;381(5):1320-31.
114. Bansal S, Vachher M, Burman A. Calreticulin: a quintessential multifaceted protein with therapeutic potential. Journal of Proteins and Proteomics. 2023;14(3):187-200.
115. Krause K-H, Michalak M. Calreticulin. Cell. 1997;88(4):439-43.
116. Jiang Y, Dey S, Matsunami H. Calreticulin: Roles in Cell-Surface Protein Expression. Membranes. 2014;4(3):630-41.
117. Deng S, Liu J, Wu X, Lu W. Golgi Apparatus: A Potential Therapeutic Target for Autophagy-Associated Neurological Diseases. Front Cell Dev Biol. 2020;8:564975.
118. Le Grand JN, Chakrama FZ, Seguin-Py S, Fraichard A, Delage-Mourroux R, Jouvenot M, et al. GABARAPL1 (GEC1): original or copycat? Autophagy. 2011;7(10):1098-107.
119. Chan JCY, Gorski SM. Unlocking the gate to GABARAPL2. Biol Futur. 2022;73(2):157-69.
120. Pipe SW. Functional roles of the factor VIII B domain. Haemophilia. 2009;15(6):1187-96.
121. Chen W, Zhao H, Li Y. Mitochondrial dynamics in health and disease: mechanisms and potential targets. Signal Transduction and Targeted Therapy. 2023;8(1):333.
122. Wang S, Long H, Hou L, Feng B, Ma Z, Wu Y, et al. The mitophagy pathway and its implications in human diseases. Signal Transduction and Targeted Therapy. 2023;8(1):304.
123. Hyttinen JM, Niittykoski M, Salminen A, Kaarniranta K. Maturation of autophagosomes and endosomes: a key role for Rab7. Biochim Biophys Acta. 2013;1833(3):503-10.
124. Ganesan D, Cai Q. Understanding amphisomes. Biochem J. 2021;478(10):1959-76.
125. Sanchez-Wandelmer J, Reggiori F. Amphisomes: out of the autophagosome shadow? Embo j. 2013;32(24):3116-8.
126. Mauthe M, Orhon I, Rocchi C, Zhou X, Luhr M, Hijlkema KJ, et al. Chloroquine inhibits autophagic flux by decreasing autophagosome-lysosome fusion. Autophagy. 2018;14(8):1435-55.
127. Liu L, Han C, Yu H, Zhu W, Cui H, Zheng L, et al. Chloroquine inhibits cell growth in human A549 lung cancer cells by blocking autophagy and inducing mitochondrial-mediated apoptosis. Oncol Rep. 2018;39(6):2807-16.
128. Chaanine AH, Gordon RE, Nonnenmacher M, Kohlbrenner E, Benard L, Hajjar RJ. High-dose chloroquine is metabolically cardiotoxic by inducing lysosomes and mitochondria dysfunction in a rat model of pressure overload hypertrophy. Physiological Reports. 2015;3(7):e12413.
129. Liang DH, Choi DS, Ensor JE, Kaipparettu BA, Bass BL, Chang JC. The autophagy inhibitor chloroquine targets cancer stem cells in triple negative breast cancer by inducing mitochondrial damage and impairing DNA break repair. Cancer Lett. 2016;376(2):249-58.
130. Zhu M, Zheng C, Wei W, Everett L, Ginsburg D, Zhang B. Analysis of MCFD2- and LMAN1-deficient mice demonstrates distinct functions in vivo. Blood Advances. 2018;2(9):1014-21.
131. Phillips PC. Epistasis--the essential role of gene interactions in the structure and evolution of genetic systems. Nat Rev Genet. 2008;9(11):855-67.
132. Gros PA, Le Nagard H, Tenaillon O. The evolution of epistasis and its links with genetic robustness, complexity and drift in a phenotypic model of adaptation. Genetics. 2009;182(1):277-93.
133. Nufer O, Mitrovic S, Hauri H-P. Profile-based Data Base Scanning for Animal L-type Lectins and Characterization of VIPL, a Novel VIP36-like Endoplasmic Reticulum Protein *. Journal of Biological Chemistry. 2003;278(18):15886-96.

Publications

Journal Publications

- **Salime El Hazzouri,** Rawya Al-Rifai, Nicole Nüsgen, Melanie Rath, Heike Singer, Johannes Oldenburg, and Osman El-Maarri. **FVIII Trafficking Dynamics Across Subcellular Organelles Using CRISPR/Cas9 Specific Gene Knockouts**. (Published in the International Journal of Molecular Science; IJMS (MDPI). DOI: 10.3390/ijms26136349; Int. J. Mol. Sci. 2025, 26(13), 6349)

- Osman El-Maarri†, Heike Singer†, Rawya Al-Rifai†, **Salime El Hazzouri**†, Mira Ibrahim†, Behnaz Pezeshkpoor, Nasim Shahidi Hamedani, Muhammad Ahmer Jamil, Nicole Nüsgen, Ursula Schreck, Melanie Rath, Judith Junen, Jens Müller, Johannes Oldenburg. **FVIII Secretion is regulated by the Combined Effects of Chaperones and Cellular Energy Homeostasis.** (In Submission to Nature Communication Journal)

  †*These authors contributed equally to this work.*

- Rawya Al-Rifai, **Salime El-Hazzouri**, Mira Ibrahim, Nicole Nüsgen, Johannes Oldenburg, and Osman El-Maarri. **B-Domain deleted Factor VIII exhibits significant differences in intracellular processing and localization when compared to full length Factor VIII.** (In Submission to Blood)

Conferences and Scientific Communication

- Intracellular visualization of FVIII protein in selected knockouts in the conventional and alternative secretion pathways. H. Singer, **S. El Hazzouri**, M. Rath, J. Oldenburg and O. El-Maarri. ISTH 2020 | Virtual Congress. *(Poster presentation)*
- Tracking intracellular FVIII co-localization with intracellular markers in wild type and in gene knockouts including Atg8 gene family. **S. El Hazzouri**, H. Singer, R. Al-Rifai, N. Nüsgen, J. Oldenburg, and O. El-Maarri. Haemophilia Symposium 2020 | Hamburg, Germany. *(Poster Presentation)*

- First detailed map of FVIII's intracellular whereabouts in a mammalian cell model. **S. El - Hazzouri**, H. Singer, N. Nüsgen, J. Oldenburg and O. El - Maarri. GTH 2022 | Leipzig, Germany. *(Poster presentation)*
- The role of „GABARAP"in the intracellular distribution of FVIII. **S. El Hazzouri**, H. Singer, M. Ibrahim, N. Nüsgen, J. Oldenburg, and O. El-Maarri. ISTH 2022 | London, UK. *(Oral Presentation)*
- Prospective FVIII intracellular trafficking routes involving GABARAP. **S. El Hazzouri,** N. Nüsgen, R. Al-Rifai, H. Singer, N. Shahidi Hamedani, J. Oldenburg, and O. El-Maarri. ISTH 2023 | Montreal, Canada. *(Oral Presentation)*
  Research and Practice in Thrombosis and Haemostasis 7 DOI: 10.1016/j.rpth.2023.100418
- Investigating the Role of GABARAP in FVIII Trafficking: A Comparative Study of Cellular Responses to Pathway Disturbances. **S. El Hazzouri**, N. Nüsgen, J. Oldenburg, & O. El-Maarri. GTH 2024 | Vienna, Austria. *(Poster presentation)*
  Hamostaseologie 44 DOI: 10.1055/s-0044-1779145
- Double CRISPR/Cas9-knockout of ER chaperones, ERGIC transporters and GABARAPs reveal additive and dominant effect on FVIII secretion. **S. El Hazzouri**, Heike Singer, Rawya Al Rifai, Nicole Nüsgen, Melanie Rath, Johannes Oldenburg, Osman El-Maarri. GTH 2025 | Lausanne, Switzerland. *(Poster presentation).*
  Hamostaseologie 45(S 01):S120-S120 DOI: 10.1055/s-0044-1801734.

Academic Achievements, Awards and Prizes

- **Deutscher Akademischer Austauschdienst (DAAD)-** *PhD Scholarship*
- **Poster Award**- *51.Haemophilia Symposium, Hamburg Germany. ''Tracking intracellular FVIII co-localization with intracellular markers in wild type and in gene knockouts including Atg8 gene family''*
- **Poster Award**- *66th Annual Meeting of the Society of Thrombosis and Haemostasis Research, GTH2022, Leipzig Germany. '' First detailed map of FVIII's intracellular whereabouts in a mammalian cell model ''*

Acknowledgements

*I would like to express my sincere gratitude to **Prof. Dr. med. Johannes Oldenburg**, Director of the Institute of Experimental Hematology and Transfusion Medicine at the University Hospital of Bonn, for hosting me as a doctoral candidate and for providing the essential support needed to conduct my research.*

*I am profoundly grateful to my supervisor and the principal investigator of this project, **PD Dr. rer. nat. Osman El Maarri**, for his invaluable guidance, active discussions, insightful feedback, and support in every aspect throughout my PhD journey. I also extend my appreciation to my second supervisor, **Prof. Dr. rer. nat. Diana Imhof**, as well as **Prof. Karl Wagner** and **Prof. Martin Hofmann-Apitius** for their evaluation and support during the doctoral examination process.*

*I would like to thank **Mrs. Rawya Al Rifai** and **Dr. Muhammed Ahmer Jamil** as well as **Mrs. Nicole Nüsgen** for her outstanding technical assistance in the lab. Nicole, you were my savior during every "technical crisis“!!*

*I would also like to express my gratitude to **all of my colleagues** at the Institute of Hematology and Transfusion Medicine. You were more than just co-workers; you were family and friends over the past 6 years... Living abroad, far from my home country, would have been far more challenging without our shared moments and interactions, mutual support, and most enjoyable conference trips.*

*My deepest thanks go to my beloved mother, **Mrs. Fatima Maarabani**, and my dear siblings**, Mrs. Rawya El Hazzouri and Mr. Ali El Hazzouri**. I am forever blessed to have you as my family; I could have not wished for more. You have illuminated every dark moment along this journey and every journey of my life. Additional thanks to my friends **Mrs. Alissar Al Tarraf**, **Mrs. Nour Shaker and Mr. Omar Ghamrawi** for being the greatest ‘’backbone’’ of all times.*

*Finally, I dedicate this work and this thesis to my late father, **Mr. Khaled El Hazzouri**, whom I lost during my PhD journey in July 2021. Dear father, I hope you are proud; without your support and motivation, I would have not been standing where I am today.*

Acknowledgements

*I lastly offer my deepest praises and gratitude to **God, the Almighty**. Without Him and the faith He provided me with, continuing the path would have been unimaginably difficult.*

"As you start to walk the way, the way appears"

-Rumi